MASTER'S THESIS

TERRESTRIAL LIDAR AND PHOTOGRAMMETRY FOR ROCKFALL HAZARD ASSESSMENT OF NATURAL ROCK WALLS

Isak Helland-Hansen

Climate change management
HVL Sogndal
Paula Hilger and Stig Frode Samnøy

24.06.2021

Abstract

Rock falls have been a major threat to infrastructure in the Norwegian landscape, particularly locations located in the steep valley landscapes in the Norwegian fjords. Roads channeled through these landscapes are particularly exposed. Two rock walls located directly above and along the E16 have historically experienced rockfalls in varying scale. These Sites are potential contributors to future rockfall activity along E16 and have been further investigated in this thesis. Testing the use and application of 3D models made by photogrammetry and LiDAR of natural rock walls was the main objective of this study.

Firstly, 3D models of both photogrammetry and LiDAR was made in November 2020 and April 2021. No rockfall activity could be detected by investigating the 3D models, this was also supported by field observations. By comparing the 3D models of LiDAR and photogrammetry at Site 1, LiDAR was found to be the preferable approach in terms of results where discrepancies between models ranged from cero to two centimeters. Photogrammetry models were had discrepancies ranging from cero to 20 centimeters. Results from site two were far worse considering both approaches and the importance of ground control points well distributed over the rock wall is highlighted as a key point for the performance of the reliability and accuracy of the 3D models. Secondly, a structural geological survey was carried out at Site 1 with the main purpose of getting a better understanding of the rock fall hazard of the rock wall. This survey comprised a scanline survey, block size measurements, a kinematic analysis and field observations. Four main joint sets were identified from the kinematic analysis where set 3F followed the foliation. Wedge sliding was defined as the most likely failure mechanism of the rock wall, including small potential of planar sliding and toppling. A potential unstable area was detected during the structure line that appeared very fractured and loose compared to its surroundings. The measured fractures defining this area did not have critical values for sliding however due to the conditions of the area and history of rockfall at the site it should not be ruled out that blocks in this area have the potential to fall out, especially when considering other mechanisms affecting rockfall. A volume estimation of this potential unstable body was done from Photogrammetry and LiDAR 3D models where the LiDAR model estimated volume 14% larger than the photogrammetry model.

Acknowledgements

I would like to thank my supervisors Paula Hilger and Stig Frode Samnøy especially, mainly for the effort and availability they have shown me throughout my work at Bolstad but also for sharing their knowledge and ideas. Paula, it has been a pleasure to learn from you and get your perspective as a researcher through zoom meetings throughout the year; also thank you Stig Frode for good driving conversations to and from fieldwork and you open office door.

I would further like to thank Thomas Scheiber, Garret John Day and Sigurd Daniel Nerhus with filed work assistance.

In addition, I would like to thank Ben Snook with input and discussion of the kinematic analysis.

A special thanks to my Grandparents Kari and Johan Seland for proofreading and to my parents Hege and Peter for encouraging me throughout my studies.

Finally, the biggest thanks goes to my supporting girlfriend Camilla Reinholdtsen for motivation, coach on citations and for putting up with me in good and bad throughout my studies at HVL Sogndal.

TABLE OF CONTENT

TABLE OF FIGURES

LIST OF TABLES

1 Introduction

Since roads first were developed in the west coast of Norway one of the major challenges has been the frequent occurrence of landslides affecting areas prone to mass movements. No settlements are directly located in the proximity of either site but as E16 experiences heavy traffic It becomes important to map these sites and get an understanding of potential rockfall in the area. The steep valleys and deep fjords are formed by scars left from previous ice ages, making the infrastructure and people in the landscape susceptible to rock slope-failures. From 2000 to 2017 there was recorded 338 mass movement incidents on the 87 km long road stretch. In the same period 30 fatal accidents happened on E16 between Bergen and Voss (Otterlei, 2017). The road is ranked as the 4th most dangerous to landslides by the Norwegian road authorities (Siem & Løvseth, 2020). In recent years, the debate of where resources should be put into road safety measures has been highly relevant posing a key question: How can we best and most effectively gather information on where to implement mitigation and adaptation measures to improve road safety.

In this thesis light detection and ranging (LiDAR) and photogrammetry is used to make 3D models and are discussed in detail. Models have been made at two sites along E16, at Bolstadøyri and outside Klutrafjellstunellen. 3D models were constructed from each technique separated by almost five months to detect potential changes in the rock wall indicating rockfall activity. This study will assess and compare the two modelling techniques in mapping natural rock walls with potential rockfall activity.

Numerous methods have been used in gathering information about rock walls and rock slope failures such as historical records, local knowledge, fieldwork efforts including information about recent activities, fresh deposits, scars in rock and vegetation and digital tools such as aerial photos and digital elevation models(Corominas, et al., 2005). Because of new data treatment techniques and technological progress in equipment, modeling of Earth's surface has been greatly enhanced (Abellan et al., 2016).

By analyzing 3D models of rock walls, we can compare LiDAR and Photogrammetrys abilities to create reliable 3D models from which further information can be gathered. Ideally accuracy,

scale, and resolution are sufficient to do further volume analysis and directional measurements of planes. The comparison and assessment of both LiDAR and photogrammetry can add knowledge to the best practice of 3D modelling of natural rock walls.

2 Objectives of the study

The essential goal of this Master thesis is to investigate and compare LiDAR and photogrammetry as tools of making 3D models of natural rock walls and their potential to map rockfall at two sites along the main road E16 between Bergen and Vossevangen. This is achieved through comparison and observations of eight 3D models, with a focus on accuracy, precision, and distance between models. A secondary focus in in this master thesis has been a structural geological survey at Site 1, where the overall goal was to understand the geology and rock fall conditions better. This survey consisted of a Kinematic analysis of planes in the wall, a scanline survey and block size measurements of past rockfall events.

This Mater thesis will ultimately add knowledge on the practical application of 3D models made from LiDAR and photogrammetry as well as add knowledge about rockfall hazard at Site 1. The thesis will be a contributing resource for future application and learning about 3D modeling of natural rock walls concerning future monitoring measures, follow-up studies and future decisions for safety measures. Furthermore, the presented interpretations and results of this study can contribute to a better understanding of factors playing important roles for rock fall in an ever-changing climate.

3 Rockfall theory

Rockfall is explained as the detachment of rocks from bedrock source areas, usually cliff faces. Promotion of rockfall is usually promoted by fractures and opening of joints caused by weathering that ultimately result in detachment of blocks (Dorren, 2003).

Rockfalls can be caused by a range of natural causes. Precipitation and snowmelt can cause erosion and water pressure in fractures that can lead to rockfall. Temperature fluxes can cause freeze and thaw cycles. When water is stuck in rock fractures it can freeze when temperatures allow, this leads to small expansions that can put pressure on blocks of rock to move. Repeating freeze and thaw cycles over time can eventually cause rockfall. Root blasting and earthquakes are also possible causes of rockfall (Hoseth, Kristensen, Håland, Viklund, &

Bjordal, 2015). Human activity can also be the cause to rockfalls by excavation for infrastructure or undercutting of slopes. (Selby, M.J. 1982) as cited in (Dorren, 2003): Animals have also been reported to cause rockfalls when climbing steep rock faces. (Dorren, 2003)

A range of failure mechanisms (figure 1) apply to rockfall and is usually determined by the geometry and geologic conditions of a rock wall. Important features are joint structures, strength and deformation parameters of the rock, and the way blocks are situated. Depending on the conditions in rock walls the most typical failure mechanisms are falling, sliding, and toppling (Poisel & Preh, 2011).
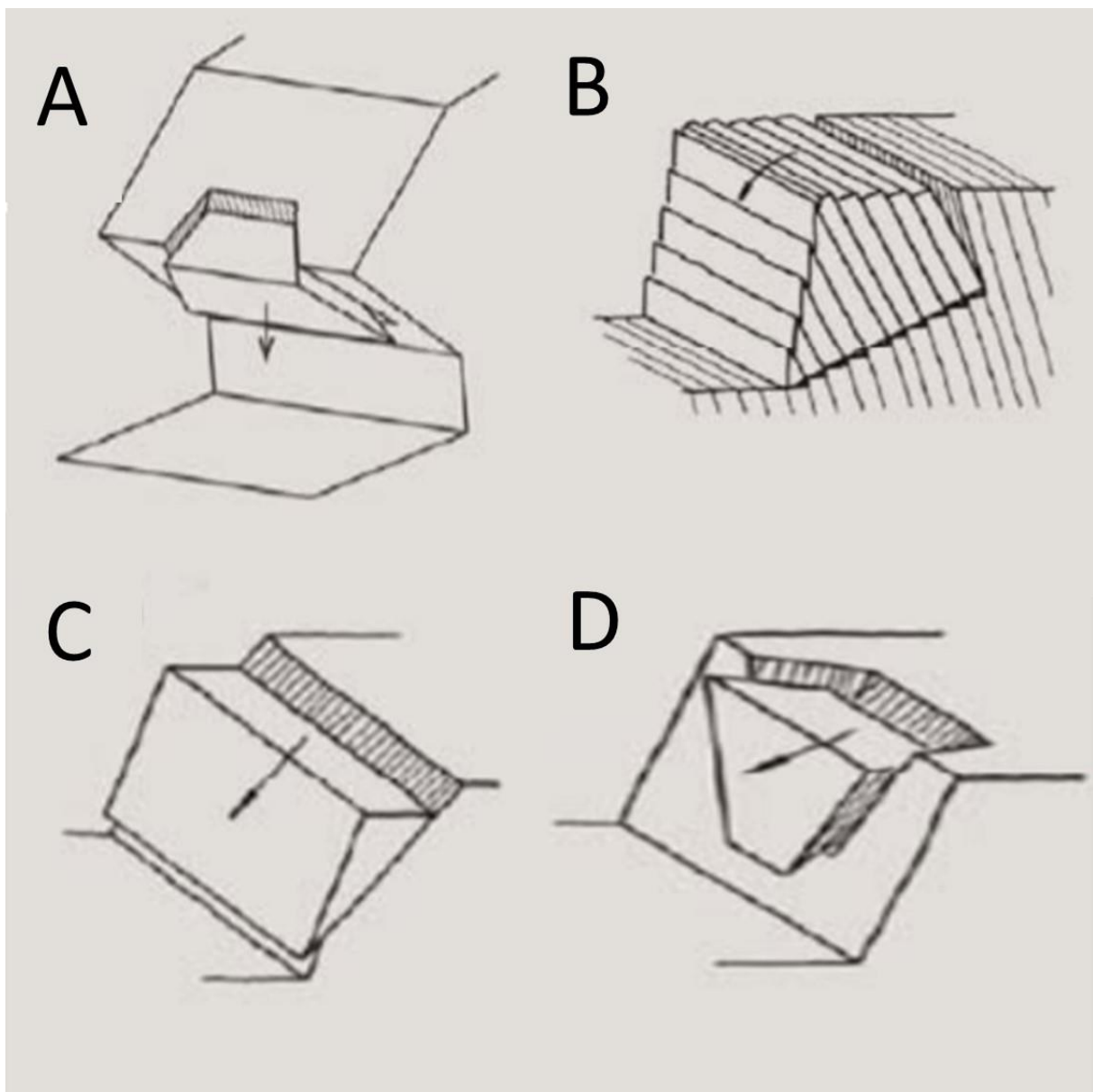
Figure 1 most common failure mechanisms for rockfall: A: falling B: Toppling C: Planar sliding D: Wedge sliding.

4 Theoretical background

This chapter will summarize the theory and history of photogrammetry and terrestrial LiDAR. 3D models have proven to be useful in recording digital data from archeological objects and sites through 3D models. Both techniques can collect data remotely and accessibility issues can be solved. Such models can also be powerful tools in monitoring and identification, of objects as well as natural features.

Challenges entailing high costs, the performance in quality of 3D modeling and challenges of accessibility has put the two approaches up against each other weighing pros and cons with both approaches resulting in choices generally relying on budget, required detail, objective, and project size (Campana & Remondino, 2008).

These technologies have had major advances the last decades due to advances in camera sensors computer power and memory storage (Zhang & Lin, 2017). Because nature is so diverse, and every study case varies highly from setup to what task you are inspecting, choosing the right method might be the key to the best results.

Photogrammetry and Terrestrial LiDAR are both optical technologies that use non-contact measuring techniques to gather data. Optical technologies can in general be divided in two groups: the group that uses laser beams which is the category where we find terrestrial LiDAR and the group which uses white light where we find photogrammetry (Baqersad, Poozesh, Christopher, & Avitabile, 2017). We can also differentiate between them as photogrammetry is a passive transmitter that captures light reflected from objects by the sun, while LiDAR is active transmitter that uses its own light.

4.1 Photogrammetry
Photogrammetry is simply put the measuring and interpretation of images to reconstruct objects or sites in 2D or 3D. Different equipment can be used ranging from handheld cameras to cameras mounted on unmanned aerial vehicles to even helicopters or airplanes. A large part of photogrammetry is the reconstruction, computing and modelling that is done when loading photos into software. We also had photogrammetry before the computer came into the picture, at that time stereoscopes were used to look at air photos and 3D observations could be observed. Today Software's are so sophisticated that they may detect overlapping

areas of pictures and are able to construct 3D models simply when photos are taken from different angles, with sufficient overlap. (Lerma, Navarro, Cabrelles, & Villaverde, 2010, p. 500).

Photogrammetry is an approach that has no physical contact with measured objects. Multiple images are captured by the reflection of visible light from objects. When multiple images are taken from different angles and with sufficient overlap common points can be identified and used to create 3D models (Baqersad, Poozesh, Christopher, & Avitabile, 2017).

4.2 Terrestrial LiDAR

A RIEGL VZ-1000 using time of flight surveying techniques a technology based on contactless data acquisition was used in this study. Time of flight work by the scanner sending pulsing laser beams towards the scanned object. Some of this light is reflected by the measured object and captured by the scanner's receiver. A point in 3D space can be very accurately acquired by measuring the time light takes to travel from the scanner to the scanned object and return. Knowing the horizontal and vertical angles of the beam, the speed of light, and the distance from the scanner to the scanned point we can very precisely calculate the point in a 3D space. Each point is given coordinates (x,y,z) that gives it a location in a 3D space relative to the scanners position. This technique yields numerous points representing a point cloud. (Slob & Hack, 2004) This point cloud is a 3D model immediately after scanning. The accuracy depends on how well a point represents the point it is trying to mimic. The accuracy is there for closely related to the distance between the points and the size of the points themselves, which determines how well details of the scanned object can be observed in a 3D model. When recording data, a scanner relies on reflected signals from a surface, factors such as atmospheric conditions, distance, incidence angle and albedo all affect the returning signal and need to be considered when scanning an object, a shiny surface is often difficult to scan. Other common challenges include temperature, as scanners can only operate within a specific range, and it is a time-consuming process if high resolution point clouds are needed (Boehler, Vicent, & Marbs, 2003, p. 1-2). Other challenges regarding the use of laser scanners are cost, the complexity of the data management, and transportation problems when bringing large equipment into difficult working sites (Historic England, 2018, p. 6).

5 Study area

The study area is located in the Vestland county in western Norway, more specifically in the vicinity of Bolstadøyri (60°38'24.3"N 5°57'34.3"E) located in Voss municipality. I focus specifically on two rock walls situated on the southern side of the valley system stretching west to east between Stammnes and Vossevangen (Figure 2).

The fjord/valley sides are dominated by steep rock slopes on either side. The climate is wet and rock slope failures have been reported frequently in the area (Angell, 2018). The sites are situated directly adjacent to and above the main road E16 connecting Bergen to Vossevangen, thus making both sites potential contributors to rockfall affecting the road in between.
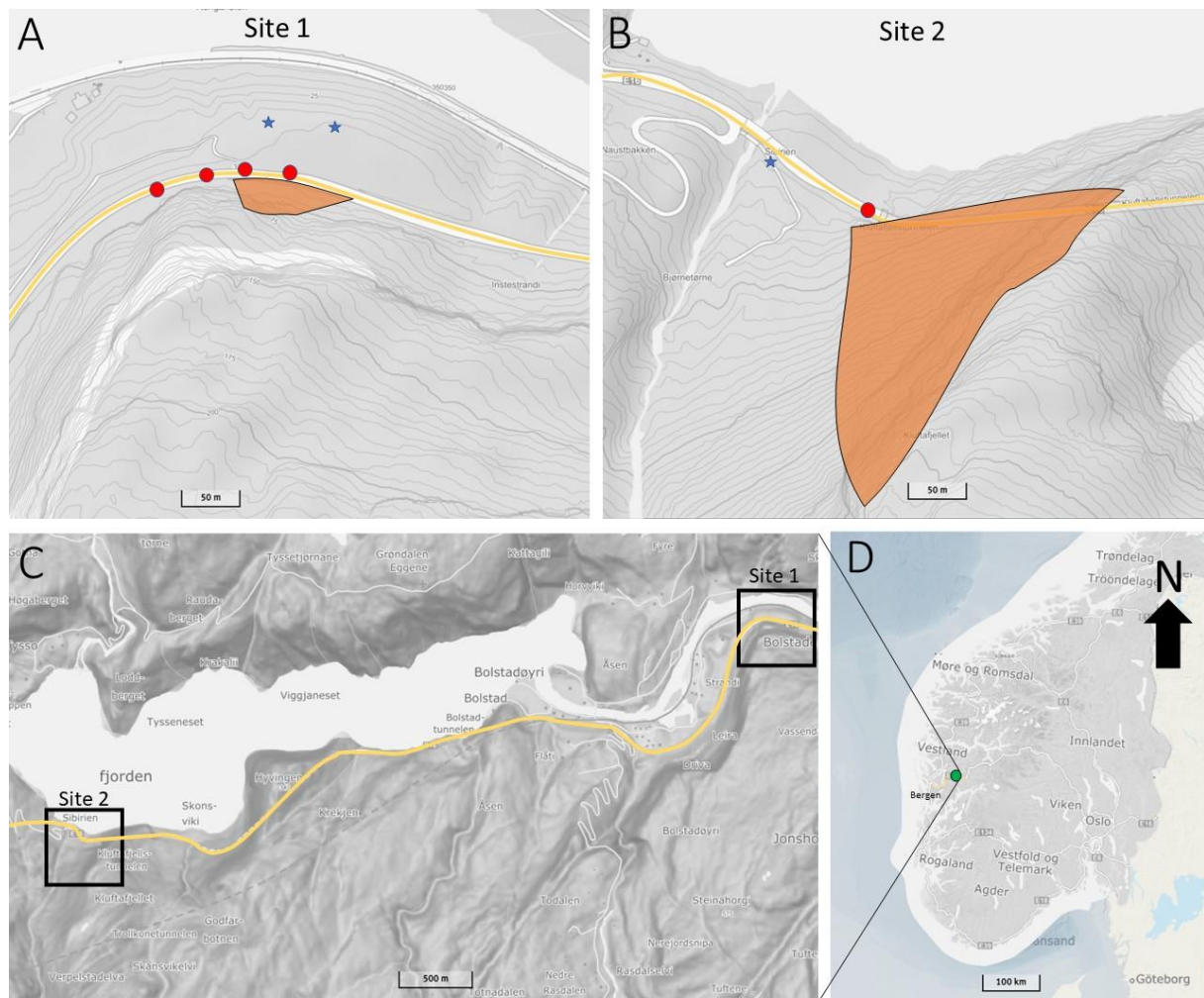
Figure 2: Overview of study area located near Bolstadøyri. (A) Map of main study area, Site 1 where the studied rock wall is outlined in orange, the laser scanners approximate positions are also marked with blue stars. (B) Map of Site 2 outlined in orange with blue star indicating approximate scanning position. (C) Overview map showing both sites in relation to Bolstadøyri. (D) overview map of western Norway locating the study area in green circle on E16 drawn in yellow between Bergen and Vossevangen. Red circles mark reported rockfall events in 2A and 2B.

Site 1. is situated at Instestrandi 40m above sea level (a.s.l.), and it is the main rock wall of this study (Figure 3). The rock wall is about 45 meters tall, and it has an average dip of 70 degrees and faces directly north. Rhyolite is the main rock type at site 1, and it has similar compounds as that of granite and is a metamorphic rock.

Adjacent to the rock wall is a small field that allowed us to setup equipment for further analysis of the rock wall. The rock wall is situated directly above the main road (E16) where the road takes a 90 degree turn to the east when passing Strandi (Figure 2A).

Figure 3: Site 1

Site 2 (14m a.s.l.) is located near Naustbakken on the southern side of the Bolstadfjord. The impressive wall is facing northwest, and it is about 260 meters tall and located directly above the Klutrafjellstunnel (Figure 4). The rock wall Is dominated by granitic gneiss, with quartzite. Granitic gneiss is a metamorphic rock type created under high pressure from e.g. Granite (magmatic rocks) the gneiss composition depends on the mineral composition transformed in the metamorphic prosses (high pressure and heat). Quartzite is a low grade metamorphic rock

type that has been transformed from sandstone influenced by heat and pressure usually related to tectonic pressure. Both sites are located on Bergsdalsdekkene.

Figure 4: Site 2

The Norwegian Road authorities have reported 206 rock fall events on E16 between Bergen and Vossevangen since year 2000. 131 of these events had volumes less than one cubic meter, 44 events had volumes of 1-10 cubic meters, eight volumes from 10-100 cubic meters, 3 of 100-1000 cubic meters and two times of over 1000m^3.16 of these events lead to parts of the road closing and 32 lead to a complete closing of the road. 70 rockfalls originated from natural mountain or valley sides, 9 inside tunnels, 29 at tunnel entrances, 5 from rock deposits and 89 from road cuttings.

At Site 1 four events (red circles Figure 2A) have been recorded in February 2000, December 2007, December 2010, and March 2018. The first three events were reported to be under one cubic meter, where the event In February 2000 lead to damage of the road and part of the road being closed. The Last recorded event in 2018 was reported to have a volume of approximately one cubic meter however this rockfall did not reach the road and was observed in the ditch beside the road.

At Site 2 only one event (red circle Figure 2B) has been reported in August 2018, this rockfall had a volume of approximately 15 cubic meters and caused damage to the road, vehicles, drainage systems along the road, and the road railing. The road was completely closed for a time. Today fall nets above the tunnel entrance stop rockfalls from reaching the road.

5.1 Climate today

Because there is no weather station located in Bolstadøyri, data from different weather stations were used depending on available data at each weather station. Temperature data

was available from Evanger weather station approximately 10km form Site 1. Temperatures averaged 15.4 degrees Celsius recorded during summer months at Evanger in 2020. Winters were relatively cold and the mean monthly temperature for January has been ranging from -0.6 to -5.6 in the last 5 years. The weather station located in Øvstedal Three kilometers form Site 1 was the closest weather station that had precipitation recordings. Precipitation the last 30 years has been recorded where annual precipitation has been ranging from a low of 2050 mm in 1993 to a high of 4400mm in 2011. At Øvstedal snow cover data was also available. Snow cover recorded the last 10 years showed 6.2 months with snow cover each year at varying levels (Meteorologiskinstitutt, 2021).

On a larger scale Hordaland, now part of Vestland, experiences a wide range of climatic variations. The climate is generally mild at the coast with large values of precipitation. At the same time we find low precipitation values further in the fjords and in the continuing valleys. In the winter, the average temperature is about 0 degrees at the coast, while its considerably lower at higher elevations as well as further inland. Annual precipitation values vary greatly from about 1200 millimeters at the very coast and inland regions to about 3500 mm at precipitation rich areas near the coast.

For reference, Vossevangen has experienced an average of 1330 millimeters annual precipitation and 5.8 degrees Celsius average in the time span from 1900 to 2014. In comparison Bergen has experienced an average temperature of 7.9 ℃ and 2340 millimeters annual precipitation in the same time span (Norsk Klimaservicesenter, 2021).

5.2 Future climate and rock fall activity

An important consideration for this study is the anticipated increase in temperature and precipitation values due to climate change. Rockfall activity has shown correlation with increased number of freeze and thaw cycles as well as extreme precipitation events (Pratt, Macciotta, & Hendry, 2018). These triggers can be directly linked to temperature and precipitation patterns; thus, a changing climate can have effects on triggering of rockfall.

The average temperature for Hordaland is calculated to increase with about 4 ℃. The increase is largest for the fall and the winter. However, when considering frost shattering it is the variation of temperature over and below freezing temperatures that allow this effect to be a potential cause of rock fall. The Annual precipitation is calculated to increase with 15%, the

change is anticipated to be strongest during fall and winter and increase more in the already precipitation rich areas close to the coast. The change includes an increase in precipitation events both in frequency as well as intensity. The County expects a small increase in yearly water flow, during winter water flow is expected to increase due to more precipitation and precipitation falling as rain rather than snow. In the spring, the water flow is expected to increase in higher laying areas due to earlier snowmelt but decrease in lower laying areas because snow melt in these areas are likely to already be done, or no snow is present at all. In summer, precipitation is expected to increase, however water flow is expected to decrease due to increased evapotranspiration and because snowmelt in the mountains will be done sooner. In the fall, water flow is expected to increase due to increased precipitation as well as more precipitation falling as rain. The numbers presented in this report is based on analysis of downscaled climate models from IPCCs fifth report 2013 (AR5), (Norsk Klimaservicesenter, 2021).

Looking at the correlation between climatic conditions and rockfall activity is beyond the scope of this study, however it is important to know about climatic factors in the area and their ability to change to get an understanding of how climatic changes might affect rockfall activity in the area.

A change in temperature could both increase and decrease the chances of rockfall depending on the preconditions in the area. For frost shattering to occur, freeze and thaw cycles must be present. If areas do not experience temperatures below 0 degrees, frost shattering will not be a scenario as water will not freeze in these areas. Areas with ideal preconditions for rockfall might experience an increase in frost shattering due to temperature fluxes where climatic conditions previously did not allow for freeze and thaw activity. Areas might also experience intensification or decreased freeze and thaw cycles. In addition to freeze and thaw conditions, intense rainfall events have shown significant influence on rockfall activity, ultimately making higher precipitation values and intensified precipitation events a realistic cause of increased rockfall activity (Krautblatter & Moser, 2009).

It has proven difficult to quantify changes in rockfall activity on the basis of climate change (Geoextreme-prosjektet). It is anyhow probable to assume that changes of weather the next 50 years with more participation, more frequent extreme participation events, longer and

more frequent freeze and thaw cycles will result in increasing rockfall activity (Hoseth, Kristensen, Håland, Viklund, & Bjordal, 2015).

6 Method

6.1 Field work for 3D modelling

6.1.1 Installation of ground control points

Ground control points (GCPs) are known stationary points that are measured with high precision to know their exact location. Two types of GCPs have been used in this study including Asphalt nails (Figure 5A) and circular metal discs with reflective material (Figure 5B).

The main reason GCPs were installed at my sites was to compare models acquired from the first (26.11.2020) and second (17.04.2021) field survey day and identify possible rockfall activity that would appear as changes from one model to another. By giving the GCPs coordinates 3D models could be georeferenced using these known points. Targets were also needed for registration of LiDAR point clouds.

At site 1, four asphalt nails were hammered into the ground near the total station and 14 Metal discs with reflective material were bolted to the rock wall. At site 2 four asphalt nails and five discs with reflective material was used as GCPs. The targets had to be installed in the entrance area of a tunnel and not in the rock wall due to the size of the wall and difficult accessibility.

To obtain satisfactory precision and accuracy a Leica Ts 15 total station using 1 second/ angle measurement and two axis compensation was used. The total station measured the distance and direction of all GCPs relative to the total station itself, giving us internal distance and direction values for all GCPs with an expected millimeter accuracy.

The purpose of the asphalt nails was to give the rest of the GCPs coordinates and they were not used in any of the 3D models. The asphalt nails were measured by a Trimble R6 Global Navigation Satellite System (GNSS) to give these GCPs coordinates with centimeter accuracy. Based on the measured location of the asphalt nails the reflective discs were given coordinates based on the internal measurements by the total station. By using this approach, the GCPs get millimeter accuracy between them. While globally all GCPs have and accuracy of a few cm.
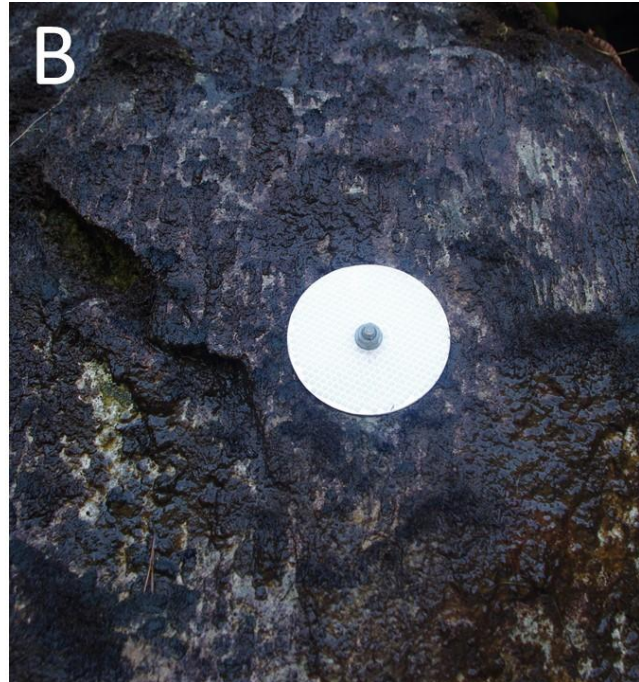
Figure 5: A: Asphalt nails hammered into the ground, used as a reference point for the total station. B: Circular metal discs with reflective material (10cm diameter) used as GCPs in 3D models for comparison and georeferencing.

6.1.2 Data collection for 3D models in the field

Data for 3D models was collected twice, first on the 26th of November 2020 followed by the 17th of April 2021. For LiDAR scanning a RIEGL VZ-1000 scanner was used to capture 3D models. All scans were done with a resolution of 0.01 point per degree. The photos used for photogrammetry modelling was captured with a PENTAX K5 camera with an 188mm Lence using automatic exposure and time values, no zoom was used when acquiring the photos.

At site 1 two setups were used to capture the rock wall from different angles to minimize shadows. The Riegl scanner was placed approximately 40 meters from the wall to be able to capture the top of the rock wall. Photos were taken from the ground on the grass field in front of the rock wall (Figure 3). 126 photos were taken on the first day of data gathering in November and 95 photos were taken on the second day in April.

At site 2 only one setup for the LiDAR scanning was performed due to limited accessibility and space of the underlying area of the rock wall. 68 and 83 photos were taken of the rock wall on the two field days in November and April to make photogrammetry models.

6.3 Terrestrial LiDAR modelling

From terrestrial Lidar scanning four models were made using the software Leica Cyclone. Two models were made at site 1 and two at site 2. The approach generally consists of three major steps where details can be found in the Cyclone basic tutorial (cite):

1. Making databases

2. Registration

3. Filtering

Table 1: Overview of 3D models made by LiDAR scanning.

Location:	Scan date:	Scan name:
Site 1 (Bolstadøyri)	26.11.2020	LiDAR 1.1
Site 1 (Bolstadøyri)	17.04.2021	LiDAR 1.2
Site 2 (Klutrafjellstunnelen)	26.11.2020	LiDAR 2.1
Site 2 (Klutrafjellstunnelen)	17.04.2021	LiDAR 2.2

The first step in Leica cyclone consists of making a database where all files needed for each 3D model are imported. These files include point cloud data from each scan position and a file containing points with the coordinates of the GCPs.

The next step called registration is a process where all these files are merged to a single 3D point cloud. There are two methods of merging scans in Leica. First Individual scans were merged by using a tool called Cloud Constrain Wizard. This tool works by selecting common points (GCPs) in two different point clouds.

The second approach was used to merge the file with the points containing coordinates meassured form the total station and GNSS to the merged scans from site 1 and to the single scans from site 2.

When using this approach each GCP in the LiDAR scans must be given an ID consistent with the ID of each coordinate point meant for a specific GCP from the coordinate file.

Leica Cyclone then matches all points of same ID and the GCPs in the scans are given coordinates. The coordinate file must be used as the reference file in this process to give the GCPs the locations of the coordinate file and not vice versa.

All four scans now have real world coordinates, and the third stage of the process is filtering out trees and vegetation, to better compare the rock surface in the models.

This process was done in an open-source program called Cloud Compare(Citation). Trees bushes and visible vegetation were selected and deleted manually with scissor tool and the result is a relatively vegetation free model of the rock wall. The LiDAR 2.1 model has been used to visualize the vegetation filtering job (Figure 6). Figure 6A represents the georeferenced model of Site 2 before filtering, however in this image I have already filtered the model and put them back together giving vegetation yellow color and the rock wall behind grey color. Figure 6B shows the vegetation and areas of the model that was filtered out. Lastly Figure 6C shows the filtered rock wall without vegetation.
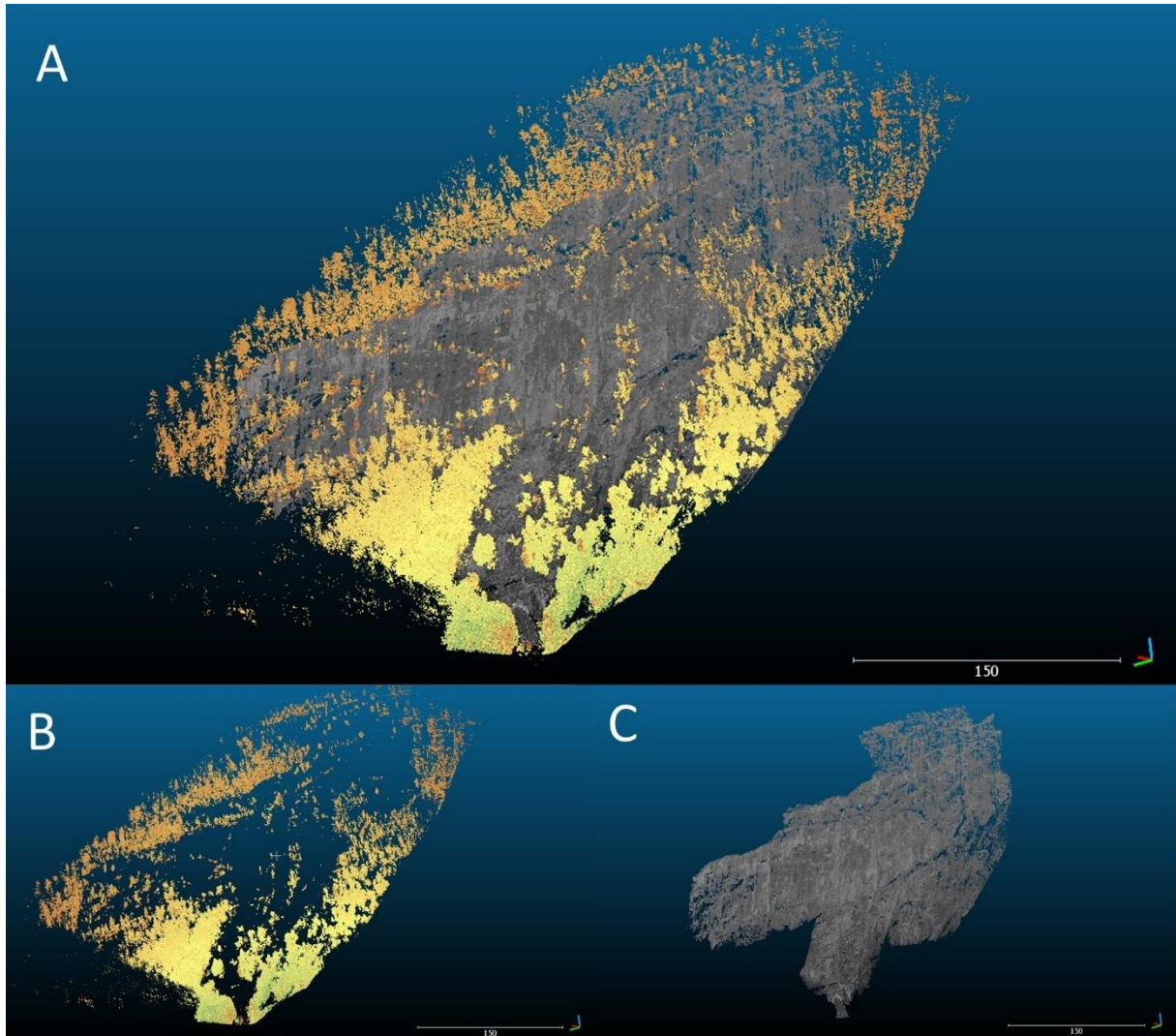
Figure 6: A: LiDAR model of Site 2 including vegetation and rock wall. B: Vegetation that has been filtered out and is not used further. C: Rock wall without vegetation ready for further analysis.
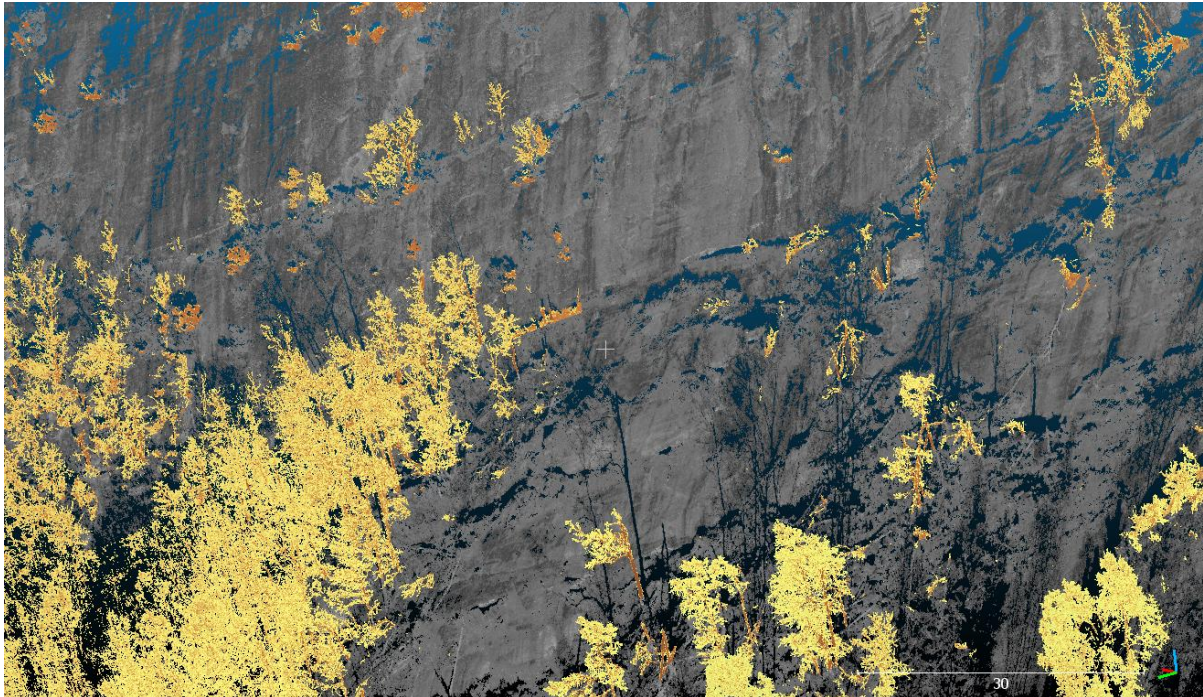
Figure 7 Cutout image of LiDAR point cloud of site 2 sampled on 26.11.2020. It is easy to see shadow effects of this model because only one scan position was used. However, most of the larger wall is vegetation free and therefore the cloud is quite well suited for comparison.

At Site 2 there was less vegetation than at site 1, the time spent on executing filtration reflects both the amount of vegetation and the area of the two areas examined. For the models of both sites this job consumed a few hours for each model, at Site 1 because vegetation was more abundant and at site two because the wall was so large. When the models are filtered, they are ready for comparison. Vegetation that was missed during the filtering process will also be detected when comparing the 3D models.

6.4 Photogrammetry modelling

Photogrammetry modelling was done in Agisoft metashape professional (64 bit). Four 3D models (Table 2) were made using a four-step approach including photo alignment (6.4.1), georeferencing (6.4.2), Dense cloud development (6.4.3) and cleaning (6.4.4). For details see user manual of Agisoft metashape professional (Agisoft Metashape User Manual, Professional Edition, Version 1.5, 2019). The raw data used to make 3D models are images taken from different angles with at least 70% overlap. Table 2 shows location, image count and date of the data gathered.

Table 2: Overview of 3D models made by Photogrammetry including; name, location, date and image count of each model.

Model name:	Location:	Date:	Image Count:

Photogrammetry 1.1	Site 1 (Bolstadøyri)	26.11.2020	126
Photogrammetry 1.2	Site 1 (Bolstadøyri)	17.04.2021	95
Photogrammetry 2.1	Site 2 (Klutrafjellstunnelen)	26.11.2020	68
Photogrammetry 2.2	Site 2 (Klutrafjellstunnelen)	17.04.2021	83

6.4.1 Photo alignment

During photo alignment the software runs two processes called aerial triangulation and bundle adjustment. Aerial triangulation is where Agisoft searches for common points across images and matches them in tie points.

The tie point limit is set to 4,000 and is the maximum number of matching points for every image, this was a recommended value by Agisoft warning that a too high or low value could result in points in the dense point cloud to be missed. The key point limit was set to 40,000 and is the maximum number of points on every image to be considered during photo alignment. Bundle adjustment is very easily explained as the estimation of the location of a 3D point in relation to the camera and involves minimizing the error of this point.

The camera position of each picture is also found in this process. The results from the alignment tool makes a sparse point cloud as well as giving estimated relative camera positions. All point clouds are made with high accuracy meaning that the software works with the photos in their original size. In contrast medium settings downscales the images by a factor of four. For high accuracy, the process takes about 3-5 minutes depending on image count.

6.4.2 Georeferencing

Georeferencing entails the process of changing the models local coordinate system to a global coordinate system by using a transformation algorithm. The model is hereby given correct scale and location in the global coordinate system. This is necessary to be able to compare a model with another model from different time period, to compare it to a model using a different method and to do area and volume measurements. In all models the global coordinate system WGS 84/UTM zone 32N has been used.

Site 1:

The 13 GCPs are identified in the images. By placing a marker on the visible GCP the images are assigned the correct coordinates given to this marker (Figure 8). When assigning a marker to a GCP in one image the software automatically detects the same point in the other images.

To obtain high accuracy markers needed to match well with the GCPs and all markers in every image had be manually verified and corrected if necessary. The manual verification included 1007 points in 125 images and 787 points in 95 images for photogrammetry model 1.1. and 1.2, respectively. After all targets are corrected and verified, coordinates can be given to each marker (Table 3). Agisoft allows for setting coordinate systems based on either camera coordinates or GPCs. In this thesis GCPs have been used because coordinates of these points are usually more accurate than coordinate data from cameras. Witch in turn allows more precise georeferencing.
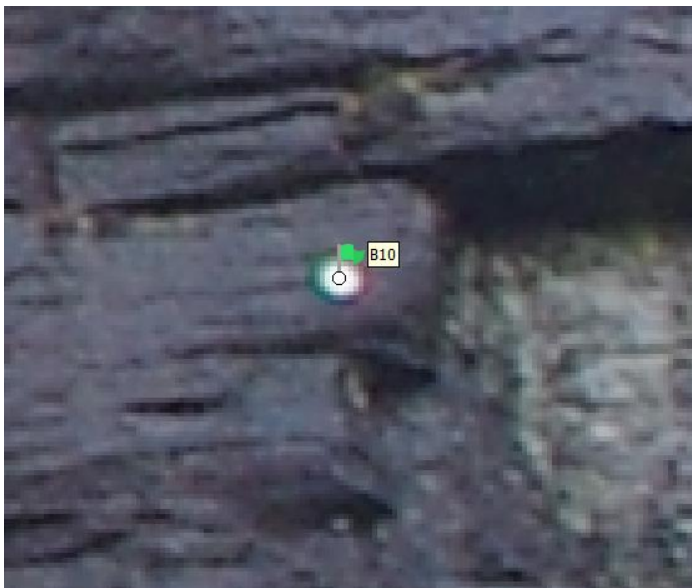
Figure 8 Displaying marker B10 placed directly in the middle of GCP B10 found in one of the images.

Site 2:

Four GCPs were installed but were not possible for Agisoft to use as they were not located in the rock wall but in a tunnel area below. Therefor 5 stable physical features in the rock wall have been used as GCPS for these models. The coordinates of these points were acquired through LiDAR 2.1 model.

Table 3: Overview table of Markers in Agisoft Metashape Professionals matching error to the coordinates of the GCPs in the wall. With coordinates included. Last column includes a number of how many photos each target appear in.

Marker ID	Northings	Eastings	Altitude	Error (m)	Projections
B1	6727061.72	334836.179	52.6	0.0006	34
B2	6727066.19	334815.583	56.071	0.0005	67
B3	6727065.05	334811.662	64.479	0.0024	78
B4	6727066.97	334807.404	51.415	0.0049	78

B5	6727060.41	334785.949	83.908	0.0007	53
B6	6727067.01	334793.938	73.114	0.0035	73
B7	6727068.58	334792.557	66.628	0.0020	73
B8	6727071.56	334794.662	55.522	0.0010	75
B9	6727067.58	334779.123	72.17	0.0012	63
B10	6727069.48	334778.859	65.519	0.0002	61
B11	6727072.74	334782.109	57.277	0.0010	55
B13	6727069.65	334758.182	68.452	0.0013	32
B14	6727075.77	334774.287	51.459	0.0020	45

6.4.3 Dense Cloud development

Generation of dense point cloud uses dense stereo matching based on depth map calculation. (explain these two). The depth maps are calculated for overlapping image pairs based on the image's exterior and interior orientation parameters from the bundle adjustment during photo alignment. Depth maps are generated for each image in combination with images overlapping this image. All depth maps from images are combined into one large depth map and transformed into a dense point cloud.

For the final cloud ultra-high and high quality was considered. High quality was chosen as results of this quality was more than good enough in terms of details and point density (Figure 9).

Dense point cloud generation also allowed automatic filtering including mild, moderate, and aggressive setting where outliers are filtered out. After experimenting with all three options aggressive was found to be the best one fitting for my models. This kept the subsequent filtering jobs to a minimum while necessary details of the cloud were not lost.
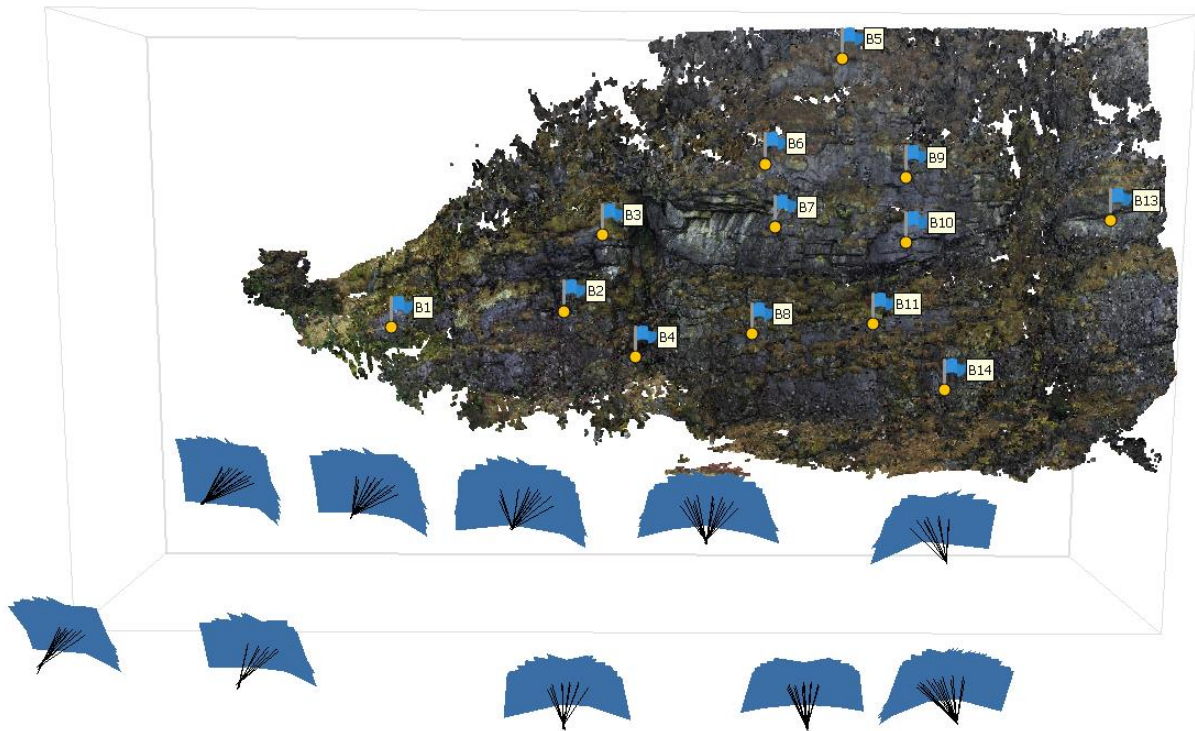
Figure 9: Photogrammetry 1.1. Image of finished cloud in Agisoft metashape professional showing dense cloud. A: Yellow points with blue flags and ID are GCPs. B: Estimated camera positions are shown in the fornt of the pointcloud in blue.

6.4.4 3D model cleaning

Cleaning was needed to prepare the 3D models for comparison. Aggressive filtering was used to develop the clouds however, there were still vegetation and unnecessary points in the periphery of the models that had no interest. Cleaning the dense point cloud was done in Cloud compare with standard cleaning tools were used. Model Photogrammetry 1.1 has been used as a before and after filtering image (Figure 10). Figure 10B is the finished 3D model for further analysis.
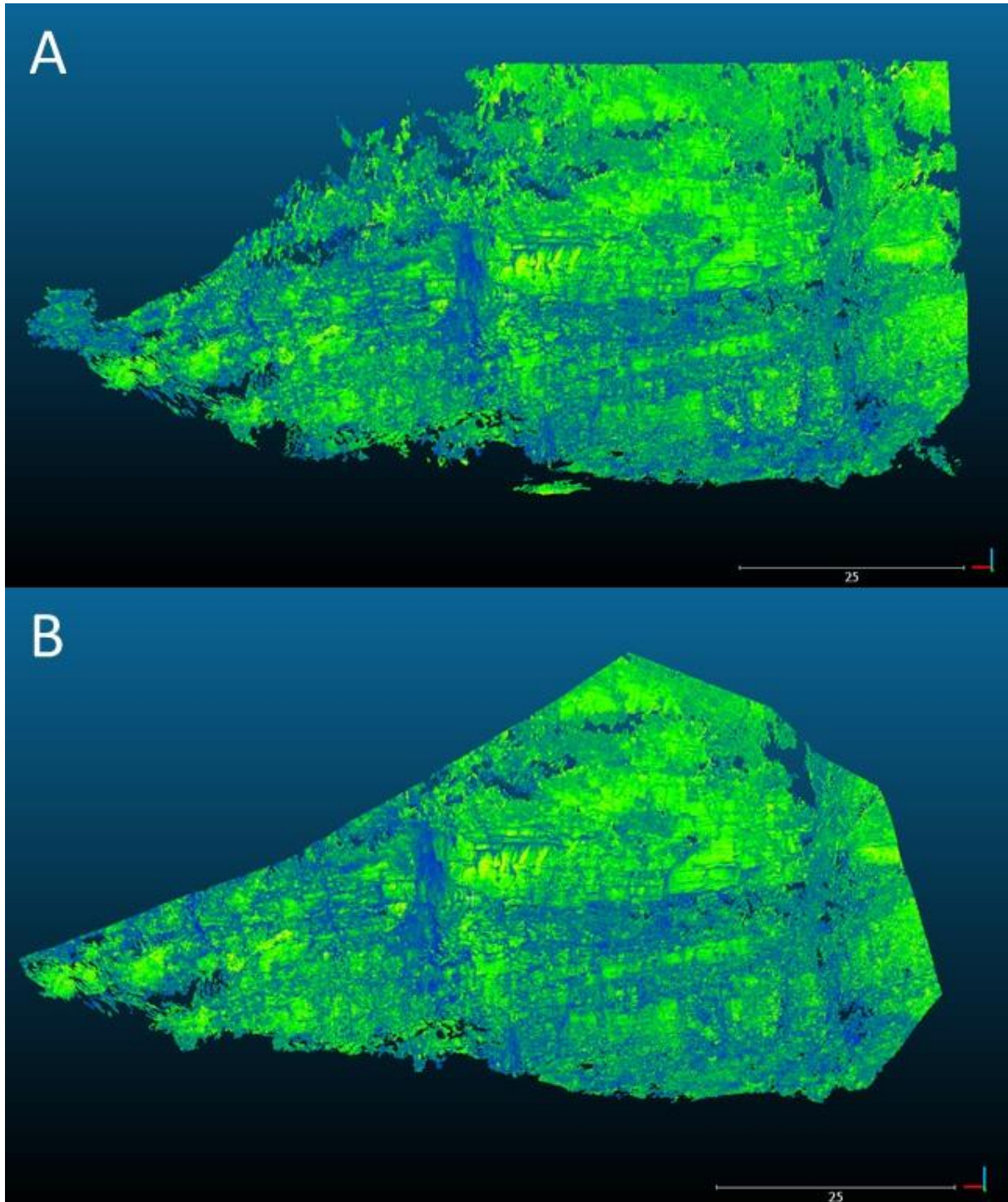
Figure 10: Image of photogrammetry model of Site 1 (26.11.2020) before filtering.

6.5 Structural geological Survey

A structural geological survey was conducted at site one to understand the geology of the rock wall. This is not the main objective for the master thesis; however it was important to do this

survey to get a better understanding about the geology of the wall in terms of identifying main joint sets, possible failure modes, potential rockfall volumes and critical failure planes at the site. The data from the simple structural geological survey was gathered in two phases field mapping and digital mapping based on LiDAR data. The data was thereby processed in Dip's software to get an overview over the main joint sets in the rock wall and run a kinematic analysis.

6.5.1 data gathered in the field

Field data was gathered on the 8th of March 2021 at site 1. The field work consisted of dip and dip direction measurements of fractures well accessible at the base of the rock-wall. 140 measurements of geological structures were done with a compass with libellee.

In addition, a basic scanline survey was conducted to measure fracture density (Figure 11). The survey was conducted using a 30-meter-long measuring tape placed along the lower right part of the rock wall. The distances between all discontinuities intersecting the measuring tape were recorded, and their orientation measured. A clearly defined, possibly unstable rock section was identified in the field marked in orange (Figure 11A). Additional recordings were taken along its delimitation, of the controlling structures.

Figure 11: (A) Showing the first part of the structure line located in the lower left area of the rock wall at Site 1, with the unstable area marked in orange. (B) Me (Isak) writing down dip and dip direction measurements along the structure line situated to the right of the unstable area. (C) A large opening in the rock wall using Paula (supervisor) for scale.

Finally, blocks found in the talus area below the rock wall was measured to see if we could identify a typical block size and how the block sizes fit with the structures in the rock wall.

Random blocks in the talus area were measured with a measuring stick, length height and width of the block were measured to calculate an approximate volume of these blocks. All these measurements were done in areas that were relatively vegetation free and situated in the lower parts or near the base of the rock wall so they could be safely collected and easily accessible. Both the structure line and the block size measurements were done to indicate, volumes of expected rockfall.

6.5.2 Digital structural geological survey

The second phase of the geological analysis consists of measurements from LiDAR point cloud data to compliment the field data in identifying the main structures in the rock wall. The Plane tool in Cloud compare was used to measure the orientations of surfaces in the point cloud. The Plane tool works by measuring orientations of planar structures. By selecting an area, a plane is fitted to the selected area giving an orientation estimate of (dip/dip direction). The distribution of measurements were conducted to get measurements from different parts of the rock wall (Figure 12). 179 measurements were done using this approach proving to be very time efficient compared to field measurements. The tool also allowed measurements in areas of the wall that were otherwise inaccessible during fieldwork. Combining data from this approach with field measurements allows identification of structures representing the whole wall.
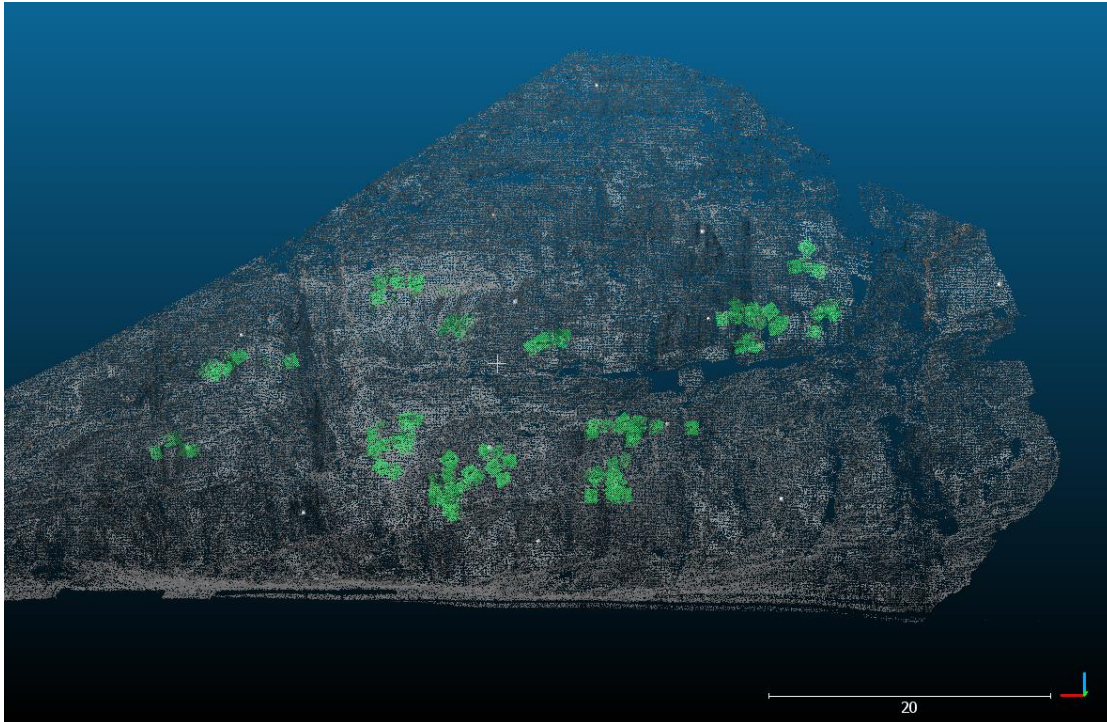
Figure 12: LiDAR point cloud data with 179 measured planes shown in green.

6.6.4 Stereo net development and kinematic analysis

The structural geological measurements were plotted as stereo nets in DIPS. By plotting the density distribution of the poles all measurements most likely representing main joint sets could be selected. Three stereo nets were made to Identify the main structures. Field measurements and data derived digitally through cloud compare was used to make two separate stereo nets. A third and final stereo net was plotted using the two datasets in combination, data from the scanline survey was also included in this stereo net.

In addition, a Stereo net of wedge sliding was made to show intersections between planes that was found in the critical zone were conditions are possible for sliding

6.5.2 Volume calculation of unstable area

The area-colored black (Figure 13) is an area of the wall that appear more unstable than the surrounding area and could be a rock-fall scenario that could potentially fallout.
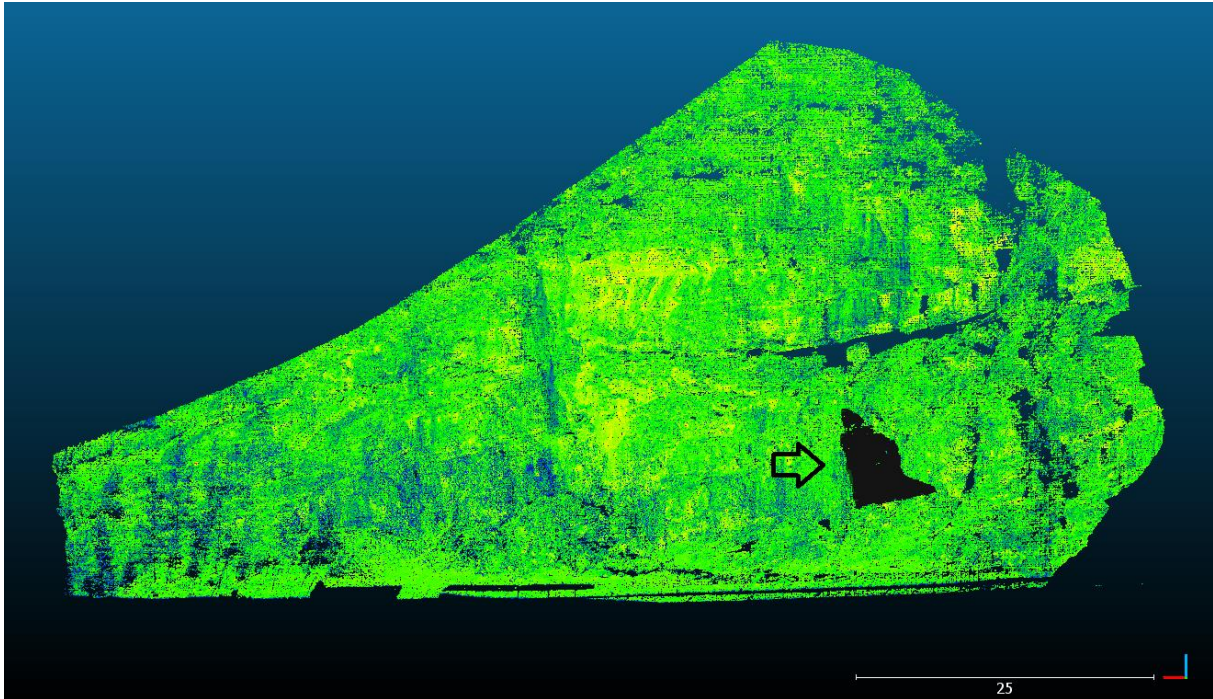
Figure 13: showing Lidar model 1.1 with the potential unstable area in black indicated by an arrow.

Segments of the models LiDAR 1.1 and Photogrammetry 1.1 was used to calculate volume of this area. Before volume calculation the potentially unstable area needed to be isolated. Three planes were used to define the unstable area (Figure 14). Planes A and B were based on measurements from the assumed back-fracture of the unstable area and plane C was based on a plane set with foliation like features identified from the kinematic analysis. The volume calculation was done in Cloud compare using 2.5D volume. 2.5D volume tool calculates volume based on a segments distance to a ground plane. More specifically plane B is turned into a horizontal plane with zero elevation. The volume is calculated by dividing the area into squares of 1 cubic centimeter area. The average height of the unstable area relative to the ground plane is calculated within each square and volume is measured. It was difficult to define the lower border of the unstable area because of vegetation. A foliation like fracture or the talus itself could both potentially define it. The volume is therefore an approximate measurement where the foliation was used.
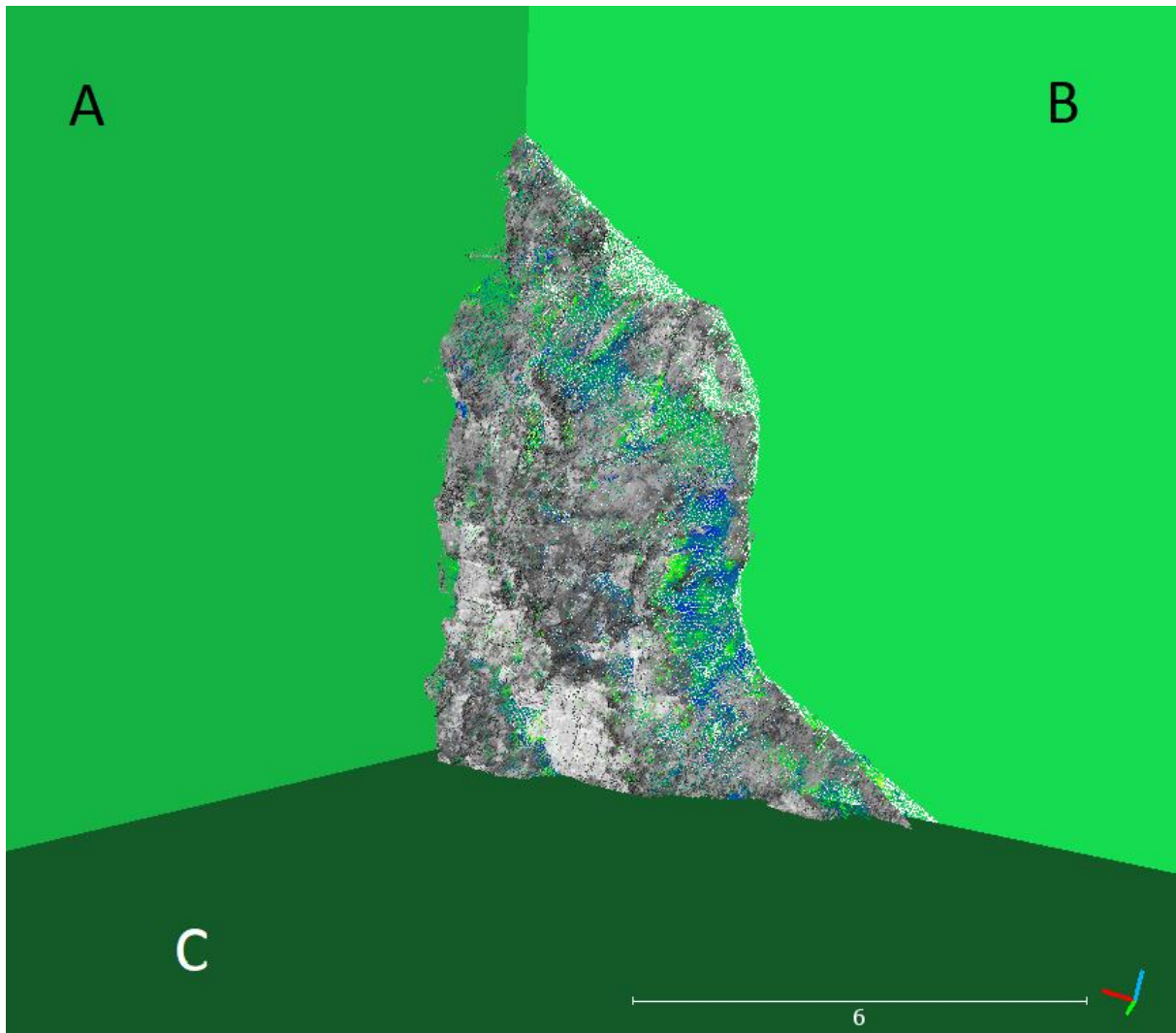
Figure 14: Potential unstable area defined by 3 planes A, B and C. Plane B was also used as elevation 0 when computing the 2.5D volume (Volume derived from Relative height from plane B to the cloud surface and area.).

7 Results

7.1 Basic information on all Point clouds

The area of site 1 and 2 was roughly estimated to be 3500 square meters at Site 1 and about 90,000 square meters at Site 2. The point density of the clouds was estimated in two different manners. First by dividing the total amount of points by the approximate surface area of the wall. By selecting a relatively flat area of the wall with no holes in the model and no edges where point density of all clouds should be relatively good. For Site 1 this area was defined in the middle of the rock wall, an area consisting of 4 square meters. The points in the area were then divided by 4 and density per square meters was given. At Site two a much larger area

was used due to the large size of the wall. First a relatively flat area was cut out of the middle of the two LiDAR clouds and the density was measured based on the number of points divided on the area in square meters. Two suitable areas were cut out of the photogrammetry models separately to do the same calculation.

At Site 1 the LiDAR Cloud surveyed on the 26th of November 2020 consisted of 22.7 million points and has an estimated point density of 6485 per square meter. The second LiDAR cloud surveyed on the 17th of April 2021 consisted of 18.57 million points with a point density of 5305 points per square meter. The Photogrammetry Cloud surveyed on the 26th of November at Site 1 consists of 6.7 million points and has an estimated average point density of 1,935 points per meter.

A complete overview of global and local density of all 3D models can be found in Table 4. The point clouds made of site 1 have much higher point densities due to a much lower surface area compared to site 2. In addition, the point clouds derived from LiDAR have higher densities then the ones made from photogrammetry. It should be noted that at Site 1 two scan positions were used and the point density is roughly doubled due to this.

Table 4: Name of models and their global and local densities of 3D model after they are filtered.

Point cloud name	Points of filtered cloud	Global point density average (3,500 square meters at site 1) (9,000 square meters at site 2)	Local point density defined by area (4 square meters at site 1) (individual area in meters at site 2)
LiDAR 1.1	22,741,731	6,485	10,626
LiDAR 1.2	18,573,436	5,306	10,882
Photogrammetry 1.1	6,774,078	1,935	1,537
Photogrammetry 1.2	9,611,089	2,746	2,344
LiDAR 2.1	16,995,202	189	7,822/14.7=532
LiDAR 2.2	20,771,814	230	8,135/14.7=553
Photogrammetry 2.1	9,435,045	105	1,980/12.9=153
Photogrammetry 2.2	8,564,636	95	2,046/13.1=156

7.2 Merging and georeferencing LiDAR

The accuracy of the registration process is presented below. This entails how well scan positions were merged and how well targets in the scan worlds were matched towards coordinate points (control file) measured by total station and GNSS (Figure 15).
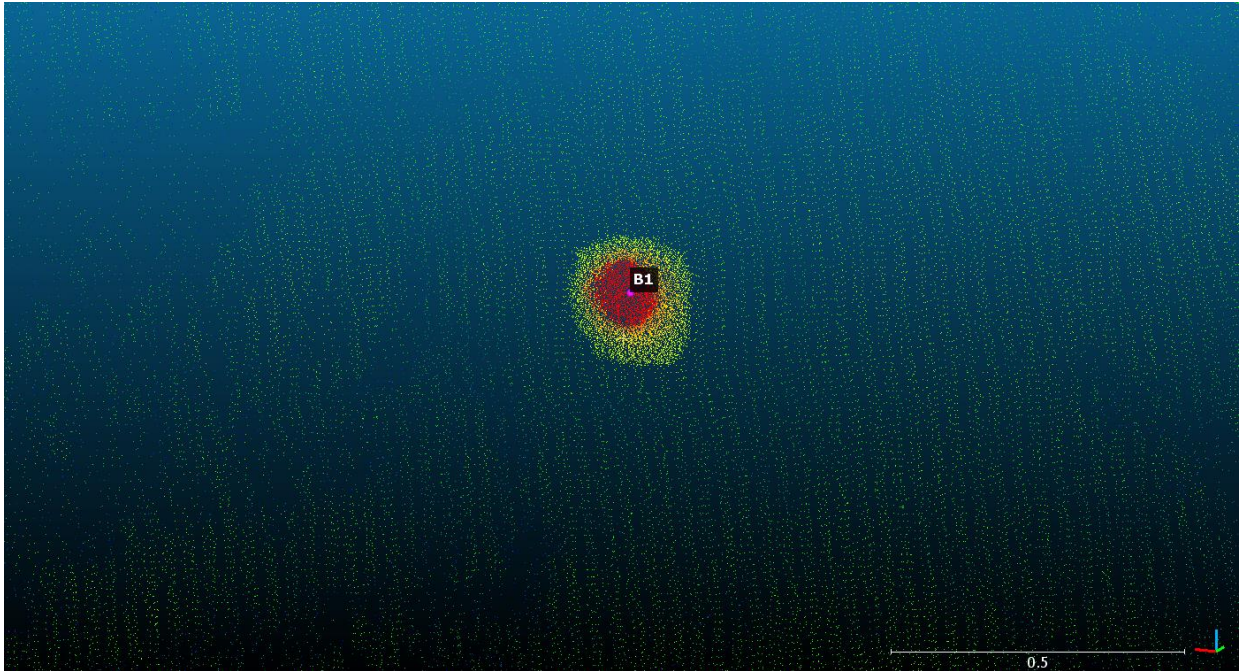
Figure 15: An image of GCP B1 showing the coordinate point exported in as a coordinate file and the LiDAR cloud in the background. The red area in the cloud is the disc with reflective material and has a diameter of 10cm. The coordinate point is a single point that must be matched to the center of the disc. If the coordinate point is in the dead center of the disc, we get an error of zero.

The two scan positions sampled on the 26th of November 2020 was merged by common point picking with cloud constraint wizard. The clouds were weighted equally, and the overall matching error was 2.7cm.

Table 5: Errors of registration of scan positions at site 1 26th of November 2020

Constrain...	ScanWorld	ScanWorld	Type	Sta...	Weight	Error	Error Vector	Group E...	Group Error Ve...	Group
✂ Cloud/M...	pos 1 w tar...	pos 3 w tar...	Cloud: Cloud/Mesh - ...	On	1.0000	0.000 m	aligned [0.027 m]	n/a	aligned [0.027 m]	Ungrouped

When adding real time coordinates each target in the 3D point clouds were given an ID and merged to the coordinate file. Difference in distance of all targets excluding 12 and 13 is shown in (table 6) below. Targets 12 and 13 were not used due to measuring errors in the field but should not affect the results of the matching of clouds as only 3 common points are needed for this operation. Target B5 and B14 have the highest error values of almost 28 and 32.5 cm respectively.

Table 6: Errors of registration of merged scans to coordinate points 26th of November 2020.

Constrain...	ScanWorld	ScanWorld	Type	Sta...	Weight	Error	Error Vector	Group E...	Group Error Ve...	Group
B2	kordinater ...	all scans m...	Coincident: Vertex - V...	On	1.0000	0.046 m	(0.005, -0.043, 0.01...	n/a	n/a	Ungrouped
B1	kordinater ...	all scans m...	Coincident: Vertex - V...	On	1.0000	0.096 m	(0.020, -0.037, 0.08...	n/a	n/a	Ungrouped
B3	kordinater ...	all scans m...	Coincident: Vertex - V...	On	1.0000	0.089 m	(0.002, 0.083, 0.034...	n/a	n/a	Ungrouped
B10	kordinater ...	all scans m...	Coincident: Vertex - V...	On	1.0000	0.018 m	(-0.005, -0.007, -0.0...	n/a	n/a	Ungrouped
B11	kordinater ...	all scans m...	Coincident: Vertex - V...	On	1.0000	0.149 m	(-0.011, -0.132, -0.0...	n/a	n/a	Ungrouped
B14	kordinater ...	all scans m...	Coincident: Vertex - V...	On	1.0000	0.278 m	(-0.030, -0.245, -0.1...	n/a	n/a	Ungrouped
B4	kordinater ...	all scans m...	Coincident: Vertex - V...	On	1.0000	0.144 m	(-0.003, -0.144, 0.00...	n/a	n/a	Ungrouped
B5	kordinater ...	all scans m...	Coincident: Vertex - V...	On	1.0000	0.325 m	(0.032, 0.304, 0.110...	n/a	n/a	Ungrouped
B6	kordinater ...	all scans m...	Coincident: Vertex - V...	On	1.0000	0.169 m	(0.000, 0.169, 0.005...	n/a	n/a	Ungrouped
B7	kordinater ...	all scans m...	Coincident: Vertex - V...	On	1.0000	0.051 m	(0.002, 0.050, -0.00...	n/a	n/a	Ungrouped
B8	kordinater ...	all scans m...	Coincident: Vertex - V...	On	1.0000	0.120 m	(-0.009, -0.108, -0.0...	n/a	n/a	Ungrouped
B9	kordinater ...	all scans m...	Coincident: Vertex - V...	On	1.0000	0.112 m	(-0.003, 0.110, 0.01...	n/a	n/a	Ungrouped

The scan positions sampled on the 17th of April 2021 was also merged by common point picking with cloud constraint wizard. The overall error of this merge was 2.9cm.

Table 7: Errors of registration of scan positions at site 1 17th of April 2021

Constrain...	ScanWorld	ScanWorld	Type	Sta...	Weight	Error	Error Vector	Group E...	Group Error Ve...	Group
Cloud/M...	210417_114...	210417_123...	Cloud: Cloud/Mesh - ...	On	1.0000	0.000 m	aligned [0.029 m]	n/a	aligned [0.029 m]	Ungrouped

The merged scan positions were then merged to the coordinate file using common names of targets. This merging showed relatively low errors ranging from 7 mm to 3.9 cm

Table 8: Errors of registration of merged scans to coordinate points 17th of April 2021 .This model matches better with the targets, where results are ranging from 7 mm to 3.9 cm.

Constrain...	ScanWorld	ScanWorld	Type	Sta...	Weight	Error	Error Vector	Group E...	Group Error Ve...	Group
B6	kordinater ...	Merged sc...	Coincident: Vertex - V...	On	1.0000	0.007 m	(0.005, -0.004, -0.00...	n/a	n/a	Ungrouped
B5	kordinater ...	Merged sc...	Coincident: Vertex - V...	On	1.0000	0.011 m	(0.010, 0.000, -0.00...	n/a	n/a	Ungrouped
B7	kordinater ...	Merged sc...	Coincident: Vertex - V...	On	1.0000	0.004 m	(-0.003, 0.002, -0.00...	n/a	n/a	Ungrouped
B8	kordinater ...	Merged sc...	Coincident: Vertex - V...	On	1.0000	0.015 m	(-0.006, 0.006, -0.01...	n/a	n/a	Ungrouped
B9	kordinater ...	Merged sc...	Coincident: Vertex - V...	On	1.0000	0.010 m	(-0.002, 0.007, 0.00...	n/a	n/a	Ungrouped
B3	kordinater ...	Merged sc...	Coincident: Vertex - V...	On	1.0000	0.010 m	(0.008, -0.007, 0.00...	n/a	n/a	Ungrouped
B2	kordinater ...	Merged sc...	Coincident: Vertex - V...	On	1.0000	0.009 m	(0.001, 0.000, 0.009...	n/a	n/a	Ungrouped
B1	kordinater ...	Merged sc...	Coincident: Vertex - V...	On	1.0000	0.022 m	(0.021, -0.005, 0.00...	n/a	n/a	Ungrouped
B10	kordinater ...	Merged sc...	Coincident: Vertex - V...	On	1.0000	0.012 m	(0.001, -0.007, 0.00...	n/a	n/a	Ungrouped
B11	kordinater ...	Merged sc...	Coincident: Vertex - V...	On	1.0000	0.011 m	(-0.003, -0.006, 0.00...	n/a	n/a	Ungrouped
B14	kordinater ...	Merged sc...	Coincident: Vertex - V...	On	1.0000	0.039 m	(-0.032, 0.014, -0.01...	n/a	n/a	Ungrouped

At site 2 the three best visible targets are used to match the single scan position to the coordinate file. Model 1 sampled on the 26th of November 2020 had errors of 3, 3 and 4 millimeters.

Table 9: registration errors of LiDAR 2.1

Constrain...	ScanWorld	ScanWorld	Type	Sta...	Weight	Error	Error Vector	Group E...	Group Error Ve...	Group
B4T	kordinater ...	pos 4 w tar...	Coincident: Vertex - V...	On	1.0000	0.003 m	(-0.002, -0.003, 0.00...	n/a	n/a	Ungrouped
B2T	kordinater ...	pos 4 w tar...	Coincident: Vertex - V...	On	1.0000	0.003 m	(0.003, -0.001, 0.00...	n/a	n/a	Ungrouped
B5T	kordinater ...	pos 4 w tar...	Coincident: Vertex - V...	On	1.0000	0.004 m	(-0.002, 0.004, 0.00...	n/a	n/a	Ungrouped

Model 2 sampled on the 17th of April 2021. Used target B1T instead of B4T because this target was more visible in this scan. Merging errors was ranging from 8 mm to 1.6 cm.

Table 10: registration errors of LiDAR 2.2

Constrain...	ScanWorld	ScanWorld	Type	Sta...	Weight	Error	Error Vector	Group E...	Group Error Ve...	Group
B2T	kordinater ...	210417_135...	Coincident: Vertex - V...	On	1.0000	0.016 m	(0.015, -0.005, 0.00...	n/a	n/a	Ungrouped
B1T	kordinater ...	210417_135...	Coincident: Vertex - V...	On	1.0000	0.011 m	(-0.011, -0.002, 0.00...	n/a	n/a	Ungrouped
B5T	kordinater ...	210417_135...	Coincident: Vertex - V...	On	1.0000	0.008 m	(-0.004, 0.006, -0.00...	n/a	n/a	Ungrouped

7.3 Georeferencing Photogrammetry

Georeferencing process of Photogrammetry happened prior to the development of 3D point clouds. The coordinate file of the GCPs was entered into Agisoft metashape and used as true points in the development of photogrammetry 3D point clouds. The results below are showing how well the targets in images match the coordinate file.

The model made of site 1 from the 26th of November 2020 had errors ranging from approximately 2cm to 39 cm. the complete error overview is shown in Table 11.

Table 11: target diagnostics of model: Photogrammetry 1.1

Markers	Easting (m)	Northing (m)	Altitude (m)	Accuracy (m)	Error (m)	Projections
B1	334836.179000	6727061.719000	52.600000	0.005000	0.111441	53
B2	334815.583000	6727066.188000	56.071000	0.005000	0.089648	95
B3	334811.662000	6727065.052000	64.479000	0.005000	0.272966	108
B4	334807.404000	6727066.972000	51.415000	0.005000	0.074121	74
B5	334785.949000	6727060.409000	83.908000	0.005000	0.150037	78
B6	334793.938000	6727067.013000	73.114000	0.005000	0.094463	101
B7	334792.557000	6727068.584000	66.628000	0.005000	0.019942	96
B8	334794.662000	6727071.559000	55.522000	0.005000	0.072800	90
B9	334779.123000	6727067.583000	72.170000	0.005000	0.054059	81
B10	334778.859000	6727069.484000	65.519000	0.005000	0.030995	75
B11	334782.109000	6727072.744000	57.277000	0.005000	0.115494	73
B13	334758.182000	6727069.648000	68.452000	0.005000	0.230255	38
B14	334774.287000	6727075.766000	51.459000	0.005000	0.389879	45

The model made of site 1 from the 17th of April 2021 hard error ranging from approximately 1cm to 5 cm. the complete error overview is shown in Table 12.

Table 12 Target diagnostics of model (Photogrammetry 1.2) surveyed on the 17th of April 2021.

Markers	Easting (m)	Northing (m)	Altitude (m)	Accuracy (m)	Error (m)	Projections
✓ ⚑ B1	334836.179000	6727061.719000	52.600000	0.005000	0.054027	34
✓ ⚑ B2	334815.583000	6727066.188000	56.071000	0.005000	0.012129	67
✓ ⚑ B3	334811.662000	6727065.052000	64.479000	0.005000	0.017154	78
✓ ⚑ B4	334807.404000	6727066.972000	51.415000	0.005000	0.020055	78
✓ ⚑ B5	334785.949000	6727060.409000	83.908000	0.005000	0.031105	53
✓ ⚑ B6	334793.938000	6727067.013000	73.114000	0.005000	0.018333	73
✓ ⚑ B7	334792.557000	6727068.584000	66.628000	0.005000	0.021028	73
✓ ⚑ B8	334794.662000	6727071.559000	55.522000	0.005000	0.019576	75
✓ ⚑ B9	334779.123000	6727067.583000	72.170000	0.005000	0.018077	63
✓ ⚑ B10	334778.859000	6727069.484000	65.519000	0.005000	0.015920	61
✓ ⚑ B11	334782.109000	6727072.744000	57.277000	0.005000	0.013098	55
✓ ⚑ B13	334758.182000	6727069.648000	68.452000	0.005000	0.029559	32
✓ ⚑ B14	334774.287000	6727075.766000	51.459000	0.005000	0.029840	45

Models made from site 2 could not use installed targets in the rock wall. Therefore, visible rock features in the wall were used as control points. The coordinates of these features were derived from LiDAR data at site 2. Errors are much larger here ranging from 60cm to almost 5m in model 1 and 1.5m to 7 m in model two.

Table 13: Target diagnostics of model (Photogrammetry 2.1) surveyed on the 26th of November 2020.

Markers	Easting (m)	Northing (m)	Altitude (m)	Accuracy (m)	Error (m)	Projections
✓ ⚑ F1	330418.123000	6725129.505000	159.473000	0.005000	4.955151	50
✓ ⚑ F2	330424.481000	6725147.544000	117.927000	0.005000	3.738444	46
✓ ⚑ F3	330371.545000	6725097.857000	163.898000	0.005000	3.658982	56
✓ ⚑ F4	330383.747000	6725118.362000	121.805000	0.005000	2.616496	55
✓ ⚑ F5	330341.464000	6725075.221000	140.792000	0.005000	0.591891	58

Table 14: Target diagnostics of model (Photogrammetry 2.2) surveyed on the 17th of April 2021

Markers	Easting (m)	Northing (m)	Altitude (m)	Accuracy (m)	Error (m)	Projections
✓ ⚑ F1	330418.123000	6725129.505000	159.473000	0.005000	7.166588	76
✓ ⚑ F2	330424.481000	6725147.544000	117.927000	0.005000	4.737337	65
✓ ⚑ F3	330371.545000	6725097.857000	163.898000	0.005000	3.809406	74
✓ ⚑ F4	330383.747000	6725118.362000	121.805000	0.005000	1.829498	79
✓ ⚑ F5	330341.464000	6725075.221000	140.792000	0.005000	1.499577	78

7.4 Cloud to Cloud distance

Cloud-to-cloud distance is the main tool used to derive results in my thesis. The tool compares two point clouds and takes measurements of the closest point in the compared cloud. This method allows me to compare two clouds derived from different methods and two clouds with temporal difference from the same method. Four temporal cloud to cloud distance measurements have been done with an overview shown in Table 15. Cloud to cloud distance

of Lidar and photogrammetry has also been done at site 1 for surveys done both in the late fall and early spring. No comparison of Photogrammetry to Lidar has been done at site 2 due to no ground control points in the rock wall. Because of this it is difficult to give the photogrammetry clouds at site two proper coordinates and scales that gives results that are satisfying for a comparison. However, an illustration is made to show the large differences between Photogrammetry and LiDAR clouds at site 2.

Table 15: Overview of Comparison of 3D models.

Name	Cloud	Compared to	site
LiDAR to LiDAR site 1	LiDAR 1.1	LiDAR 1.2	1
LiDAR to LiDAR site 2	LiDAR 2.1	LiDAR 2.2	2
Photogrammetry to Photogrammetry site 1	Photogrammetry 1.1	Photogrammetry 1.2	1
Photogrammetry to Photogrammetry site 2	Photogrammetry 2.1	Photogrammetry 2.2	2
LiDAR to Photogrammetry site 1 firste survey	Photogrammetry 1.1	LiDAR 1.1	1
LiDAR to Photogrammetry site 1 second survey	Photogrammetry 1.2	LiDAR 1.2	1

LiDAR to LiDAR site 1

The image shows the cloud measured on 17.04.2021 and the colors represent differences to the cloud measured on 26.11.2020. The cloud shows no signs of rockfall activity. The largest difference can be found at the edges of the model and in holes in the model where the models do not overlap. When there is no overlap between two models the distance is computed to the nearest point in the opposite cloud and *appears as a* higher value. These values *can be* false since *there is a possibility that* they are not computed towards the actual nearest point. Therefore, a look at the larger distances between clouds manually is necessary to see if there is an edge effect or a difference from one model to the other. However, only minor differences

could be detected between the two models that did not include vegetation or edge effects where an area was missing rather then changed.

Most of the distances between the clouds give measurements with a difference of 2cm or less which are reliable values to draw the conclusion that no rockfall has happened at site 1.

Cloud to cloud distance between LiDAR Scans at site one at first and second measurement shows small deviations (Figure 16). The cloud-to-cloud distances is set to show values ranging from 0 to 50 cm. The red and green areas in the model show vegetation that has been cropped out in one model but not the other and edge effects.
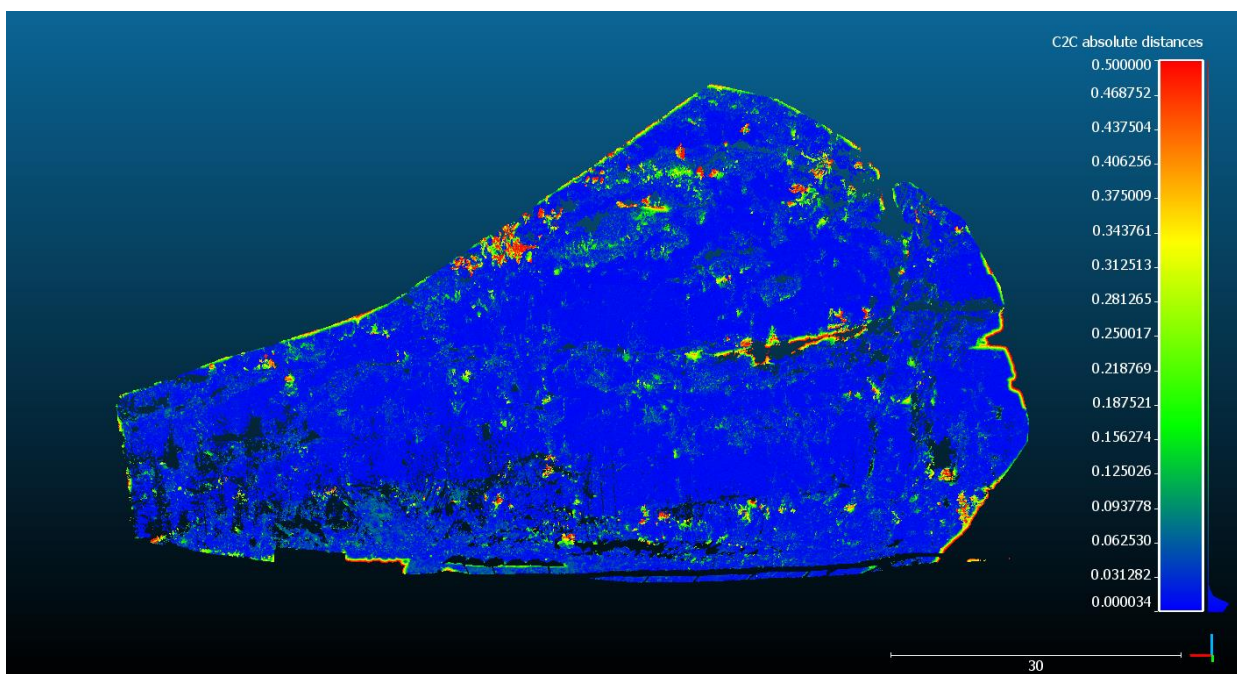
Figure 16: Cloud to cloud distance between LiDAR Scans at Site 1 at first and second measurement. Parameters are set to shows distances ranging from 0 to 50 cm.

In the following figure the cloud-to-cloud distance is set all the way down to 0 – 5cm (Figure 17). This shows the same comparison as (Figure 16) however only values with maximum 5cm is shown. The density bar on the side gives us an overview of where points are distributed in terms of cloud-to-cloud distance. Most values are less than 2cm.
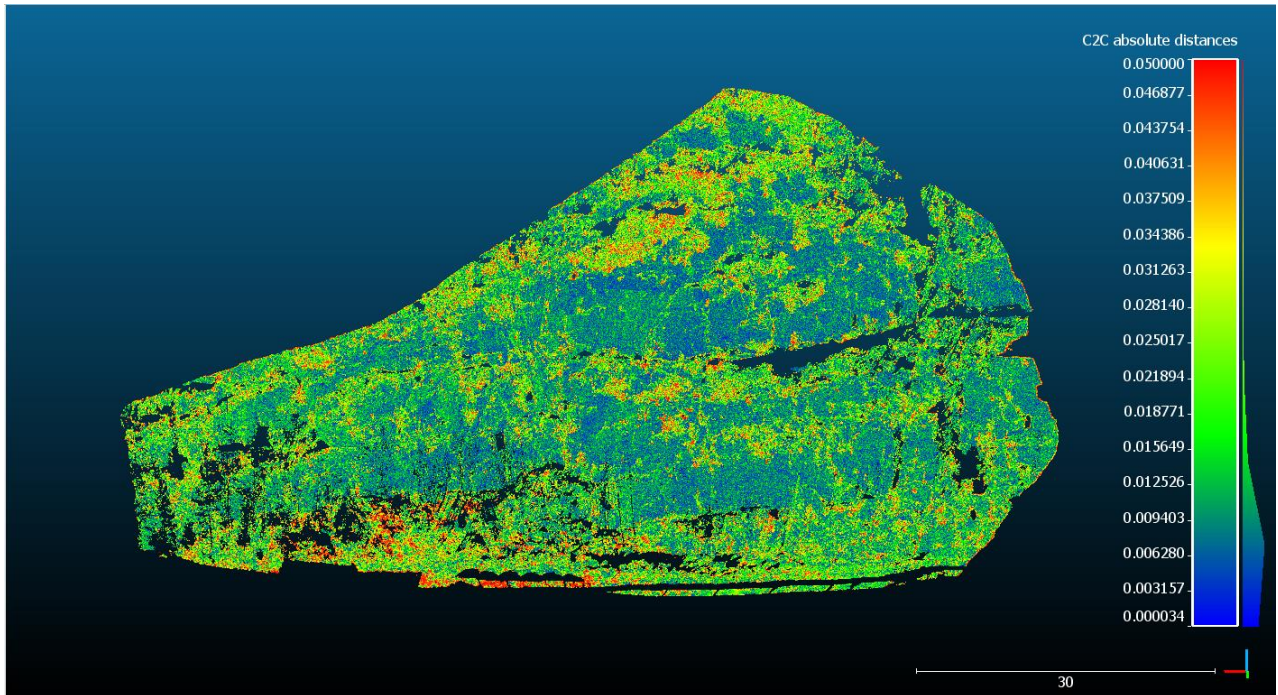
Figure 17: LiDAR to LiDAR Site 1. In this image the distance bar is changed to only show distances ranging from 0 to 5cm. As you can see in the image most of the values falls withing this range. On the right side of the distance bar, you can see the density of distance points. The density starts rising at 2.5cm distance and the majority falls between 0 and 1cm meaning that most of the distance between the two clouds are between 0 and 1cm. This supports the assumption that there has not been any rockfall activity at site 1.

The following figure shows a cut out area of the LiDAR-to-LiDAR comparison at site 1 (Figure 18). Vegetation is clearly visible as the highest distance colors. A small green area in the bottom right area could indicate small block that had fallen out, but it is a hole in one of the models that resulted in this difference. By inspecting models individually it is easier to understand why we see edge effects (Figure 18B), vegetation and differences between models when computing cloud to cloud distance.
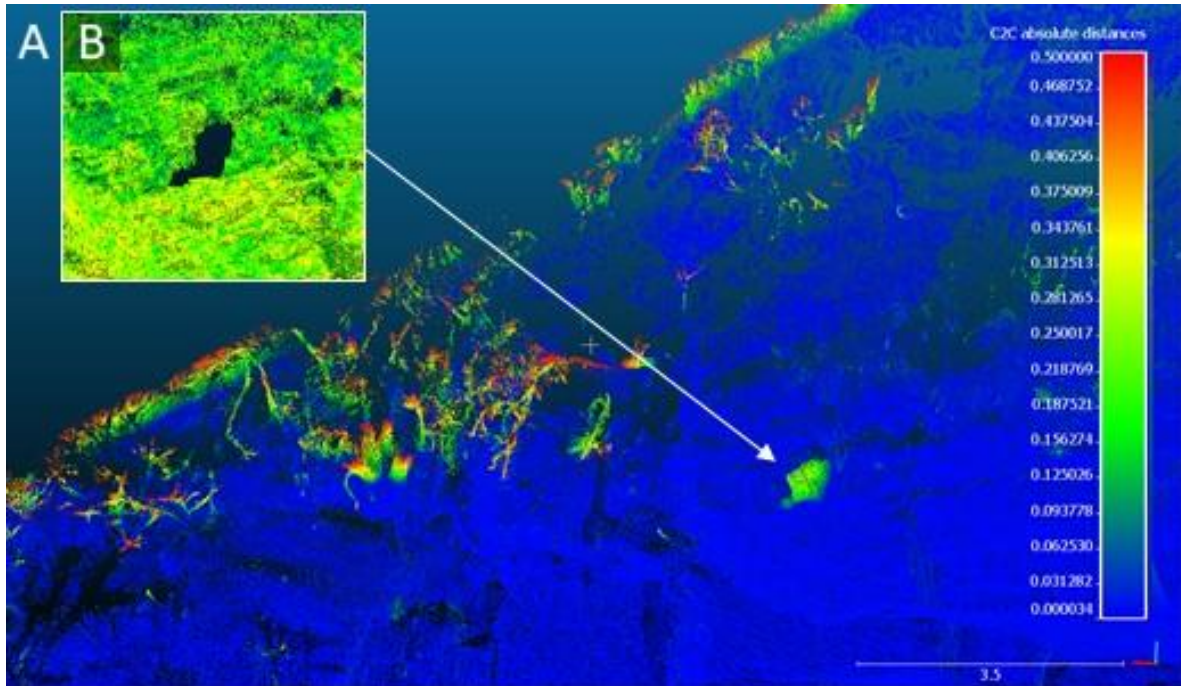
Figure 18: A: LiDAR to LiDAR site 1 zoomed in area. In this image we can observe differences of up to 50cm. These images are meant to portray how I systematically examine all the scans compared. At the top edge of the scan, I can clearly see the colors shift with the scale. This makes it very evident that it is an edge effect. I can manually toggle the two clouds to see if this is indeed a correct assumption. Vegetation missed in the filtering process is also very easily detectable and here we can see branches that stick out of the rock wall. Lastly, we have areas within the cloud not near any edges. These become particularly interesting because it looks like a block that is missing that was previously there. In this case a difference of 15- 30 cm (green) and an area close to half a meter in diameter. These spots must be manually checked and in image x you can see that this is in fact a hole in one of the models. Because the hole has such clean edges it is likely that it was cut out with a mistake during the vegetation filtering process. B: LiDAR 1.1 showing a hole in the model that results in difference in distance between clouds.

LiDAR to LiDAR Site 2

Cloud to Cloud distance between LiDAR clouds at site 2 (Figure 19) show the model surveyed on the 17.04.2021 and colors represents distance in meters to the cloud surveyed on the 26.11.2020. The majority of the points in the clouds has a distance ranging from 50cm to about

0 cm when judging from the density bar on the right of the distance bar. The models change color from upper right to lower left middle. Indicating that the models have a slight rotation resulting in this distance over a larger area. Because of this shift of up to 50 cm in the upper right area there might possibly have been activity of volumes smaller than this. However, in the lower left and middle areas the distance is lower and no rockfall activity can be seen here and can be more clearly seen in Figure 20 were shown distances are lowered to a maximum of 30cm. A few different images of the model are presented below to present the findings. A close look at the scale bar in meters is necessary as it is set to different ranges in the following images.
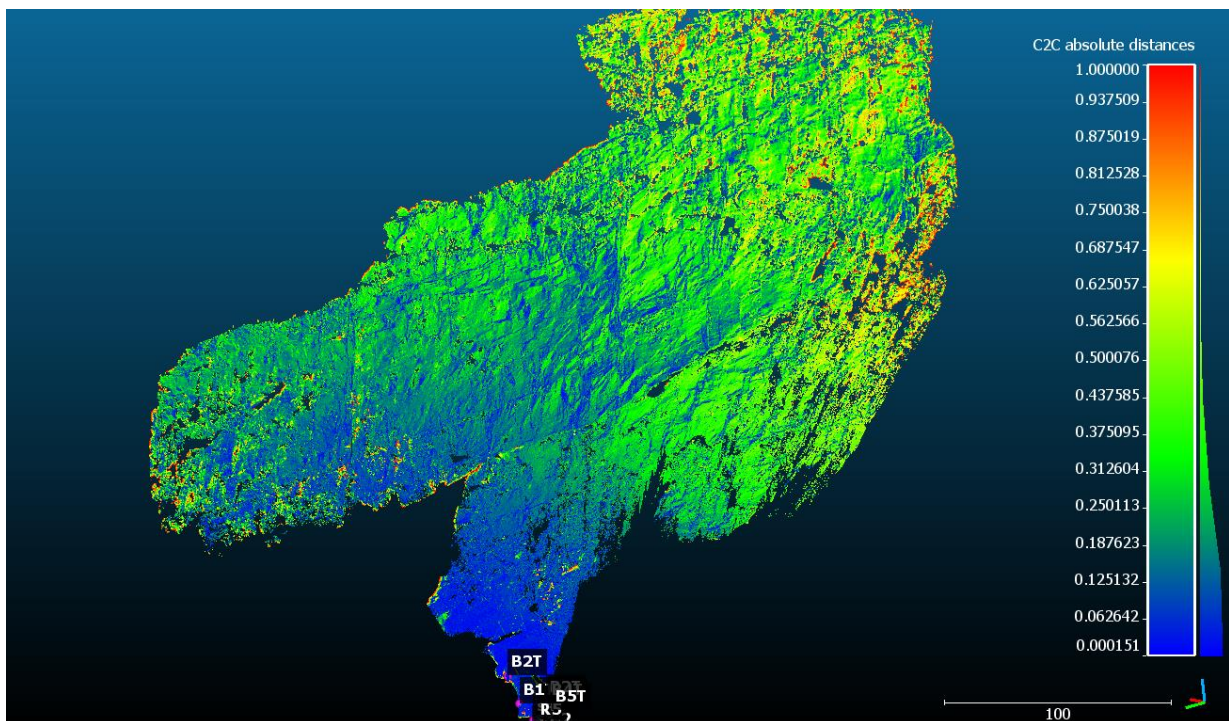
Figure 19 Comparison of LiDAR scans at site 2. With cloud distance from 0-1m. most of the distance falls withing 0-50cm with a consistency of better accuracy at the middle and lower left of the model.
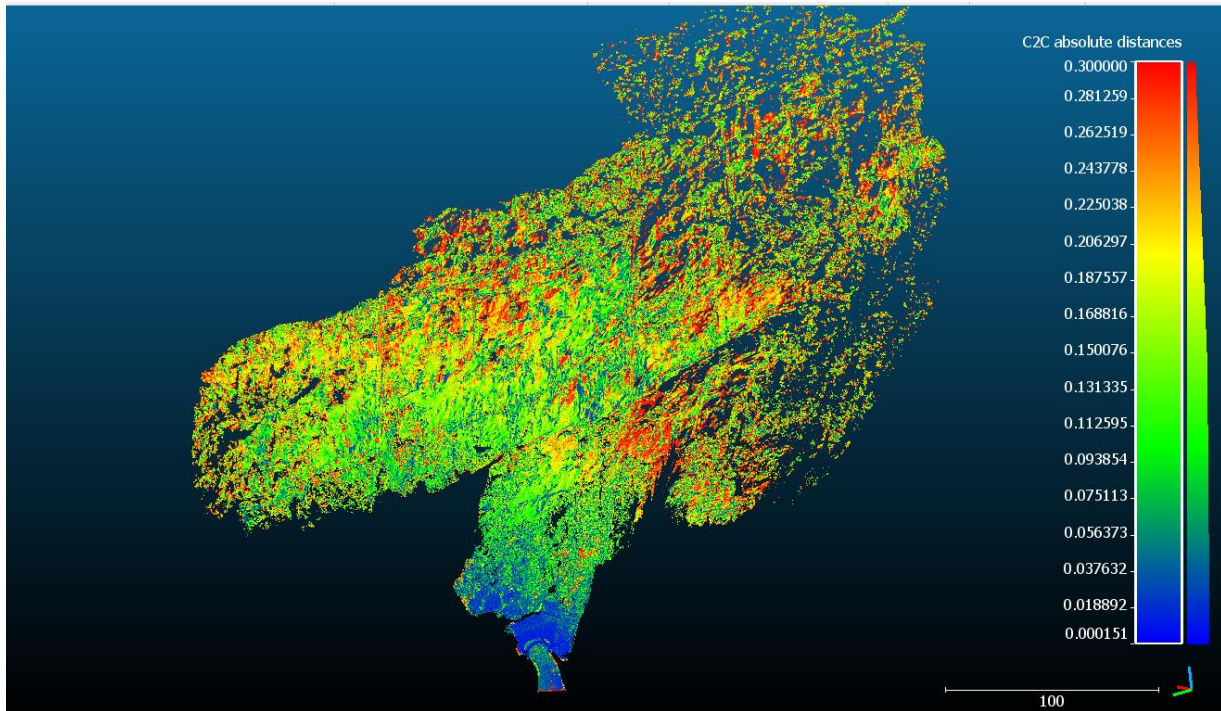
Figure 20: Comparison of LiDAR scans at site 2. With cloud distance from 0-30cm.

Photogrammetry to Photogrammetry Site 1

The majority of the two photogrammetry models has a distance between 0 and 20cm (Figure 21). The Photogrammetry models are not as complete as the Lidar models showing some occlusion, but the difference of two-time measurements shows very promising results.
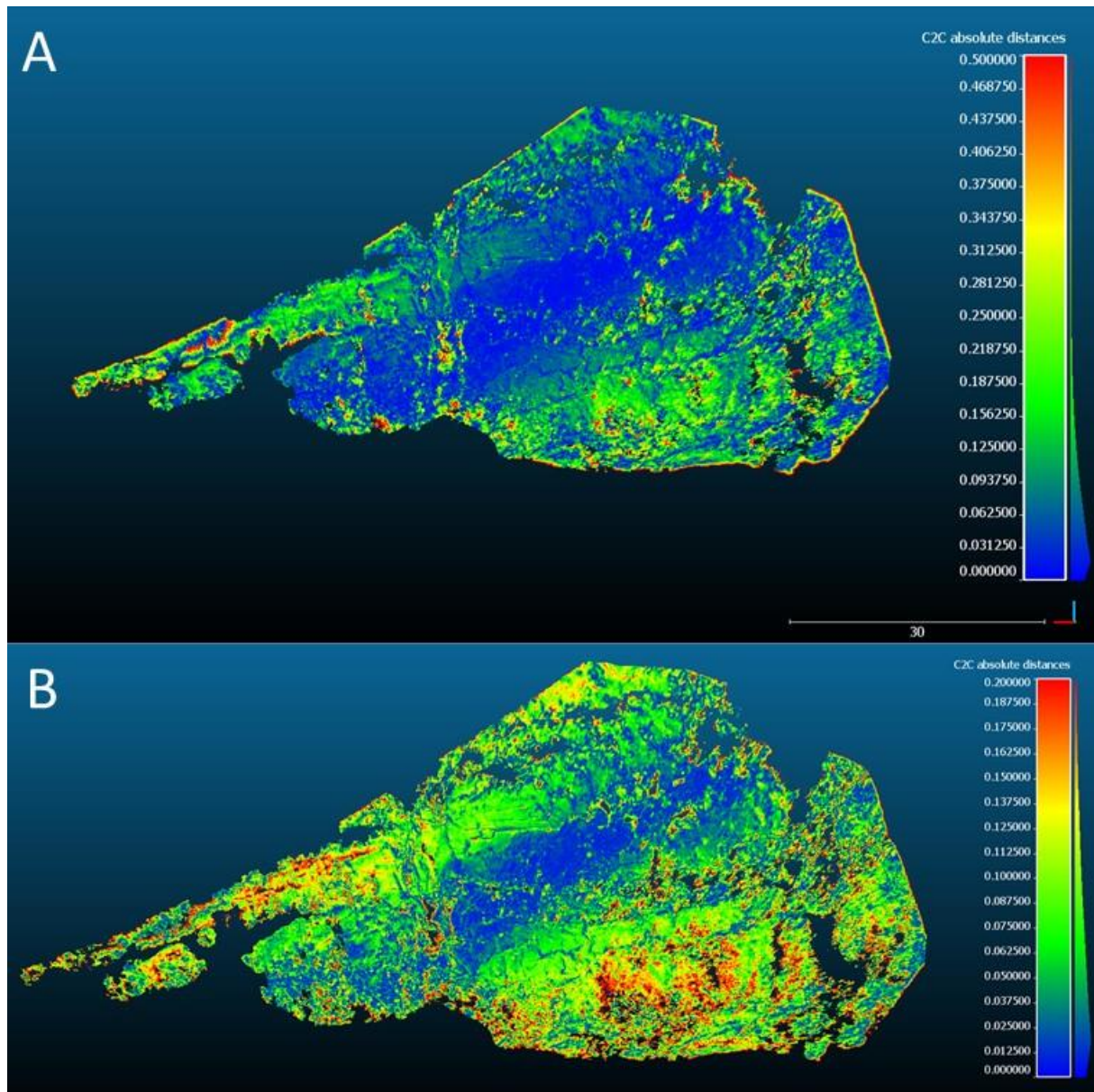
Figure 21 A: Photogrammetry to Photogrammetry Site 1. With a bar showing distances between 0 and 50 cm. B: Photogrammetry to Photogrammetry Site 1. With a bar showing 0-to-20-centimeter distance we can more clearly see that there is an area of the middle section in blue where distance is very small ranging from about 0 to 3.5 cm. the area bellow and above the blue areas in the middle section shows green colors with a distance of 3.5 to 12cm. further out at the edges we have values that are closer to 15-20 cm. Some of these values are likely to be edge effects and not representable for the model. Looking at the density bar we have a peak at about two centimeters and a falling curve towards 20cm as well as towards 0cm. however the density is far greatest between 0 and 10cm.

LiDAR to Photogrammetry site 1 first survey

This comparison shows the Photogrammetry cloud surveyed 26th November 2020 at site one. The colors represent distance to the LiDAR cloud surveyed the same day also at Site 1. Most of the models lay within 20 cm of each other, blue colors with very good comparison of 0 to 4

cm and green values showing distances of 7-16 cm. The range from 0-5 cm is the most abundant. Some values are higher than this and are partly edge effects. A closer look at an area with low distance (Figure 23A) and an area with higher values of distance (Figure 23B) is showed below.
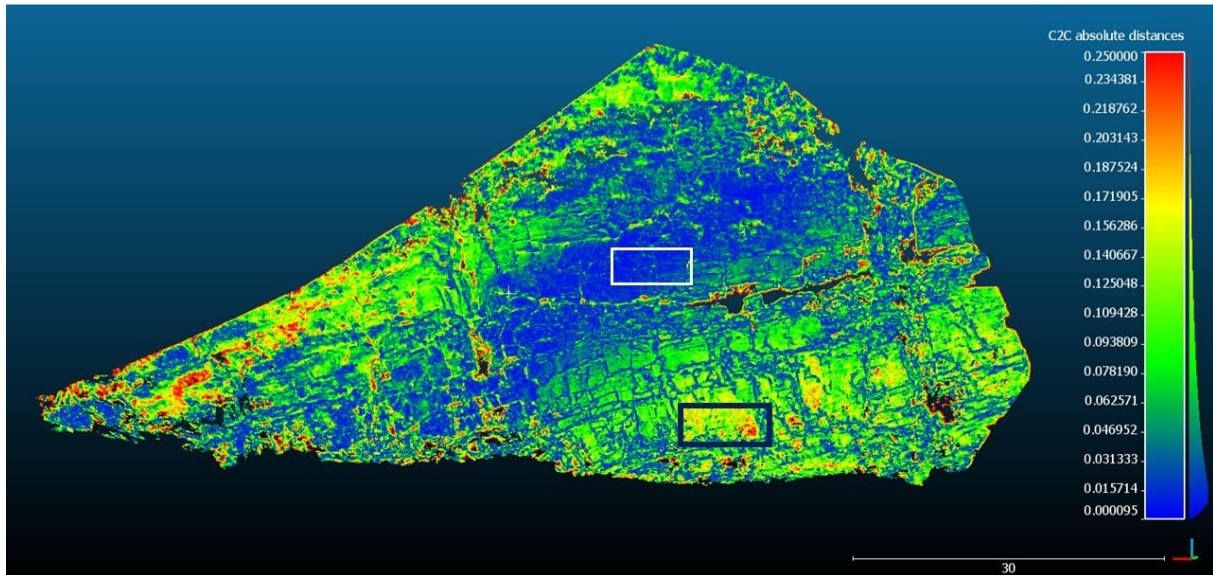
Figure 22 LiDAR to Photogrammetry site 1 first survey. Distance bar is set to 0 to 25 cm difference, showing all values within this spectrum. The distance is clearly lower in the blue middle section and larger in the lower right area and top felt area of the model. Boxes show cut outs presented in Figure 23, white box (Figure 23A) and black box (Figure 23B).
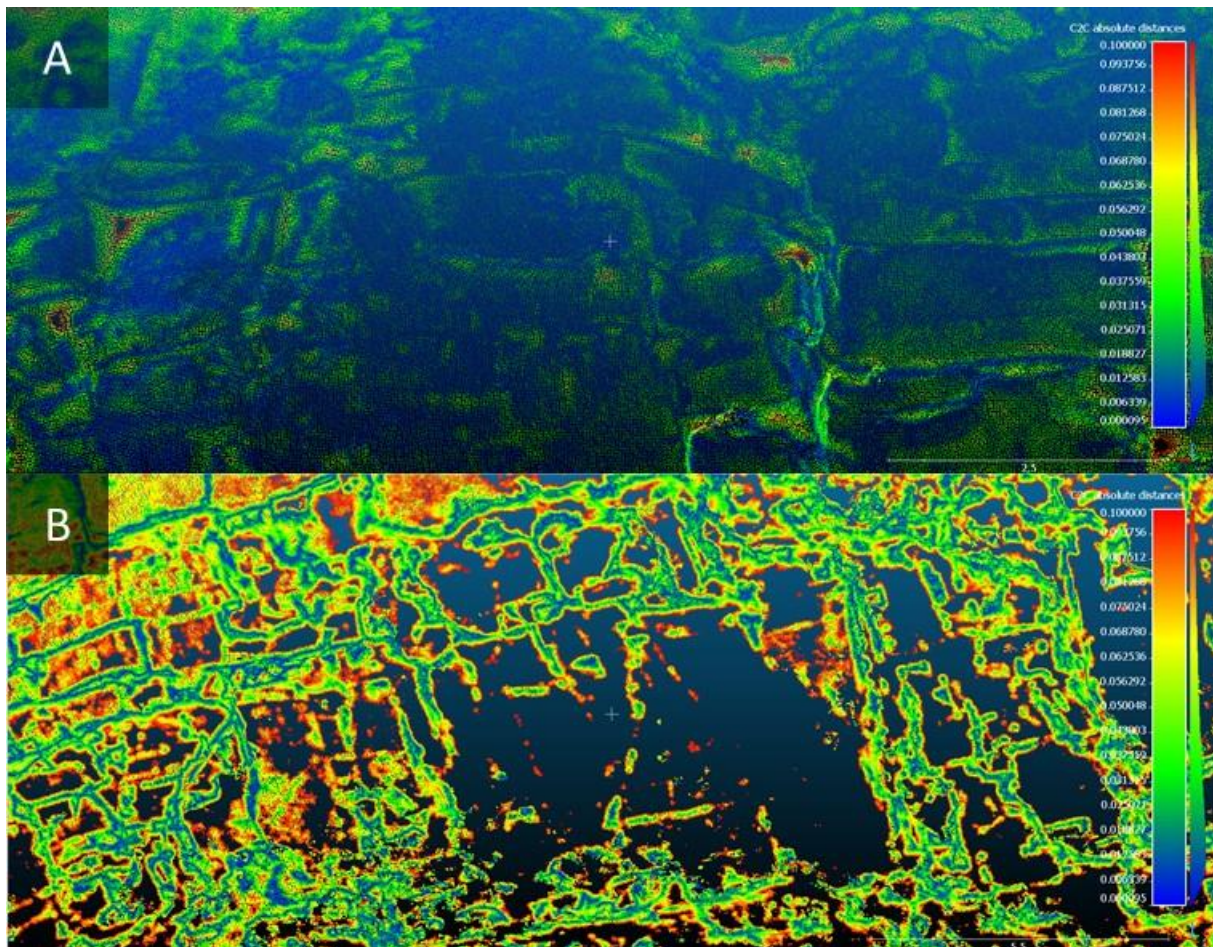
Figure 23: A: Zoomed in area of LiDAR to Photogrammetry comparison, site one first survey. The distance bar is changed to 0-10cm and most values in this cutout ranges from 0-6 cm. there are some edges and corners that are over 10 cm distance, and they appear as open areas in the model. B: zoomed in section of the model showing 0-10cm on the distance bar are showing large holes. These holes are due to distance being greater then 10cm between the clouds in these areas.

Comparison of LiDAR and Photogrammetry at Site 1 second survey

By comparing Photogrammetry and LiDAR scans from the second survey (Figure 24) relatively low values ranging from 0 to 5 centimeters distance are the most abundant that can be observed between the models. Most of the rock wall is well presented with values generally ranging from 0 to 12 centimeters.
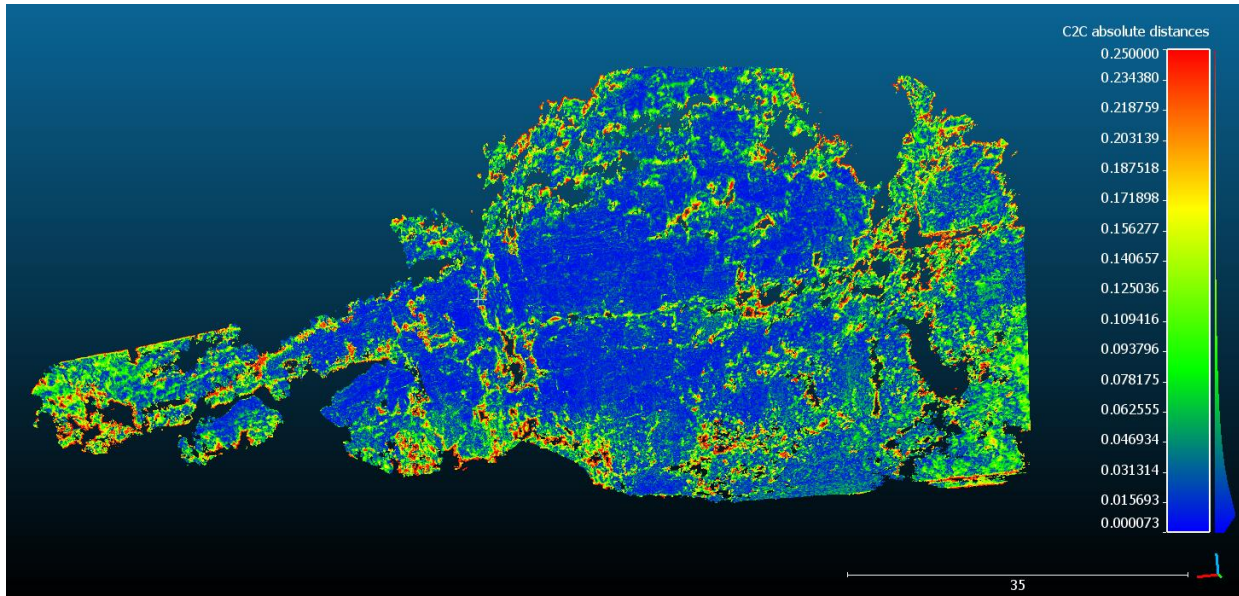
Figure 24 Comparison of LiDAR and photogrammetry at Site 1.

Comparison of LiDAR and Photogrammetry models at Site 2.

At Site 2 there is no GCPs in the wall physically. Therefore, an experimental method to match the clouds were used. This method produced results that were difficult to compare due to error values in the targets when making photogrammetry models. This is probably one of the reasons the clouds have troubles overlapping. The two photogrammetry clouds were compared to one LiDAR cloud and the distance between the clouds in some areas are 10s of meters (Figure 25). However, since the two photogrammetry clouds themselves are closer to each other, a cloud-to-cloud comparison of these were done (Figure 26). This comparison shows that there is also a rotation issue where the sides of the model are many meters apart while the middle parts are closer together.
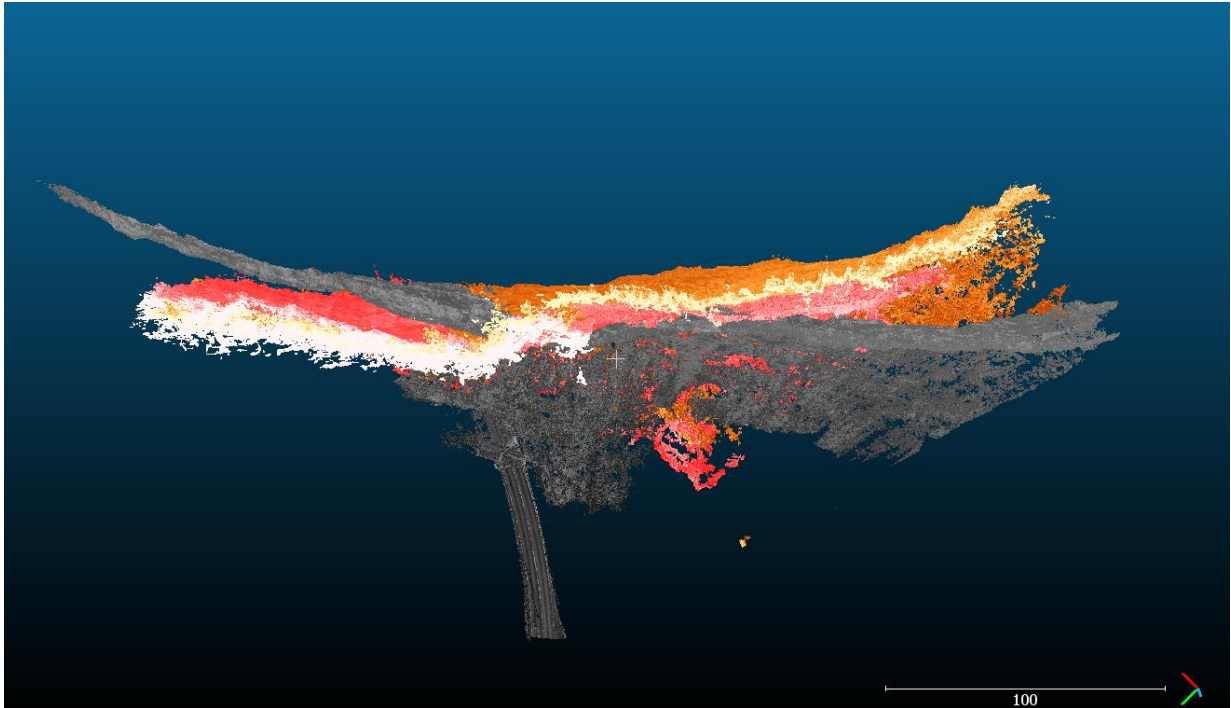
Figure 25 Overview photo of LiDAR point cloud in grey compared to both photogrammetry models in orange and red.

Lastly a comparison between the two photogrammetry models at site 2 was done and they are quite similar in the middle section but comes further apart to the right and the left of the model. From Figure 29 both these models have been rotated in a way that makes the distance between them very far at the left right edges.
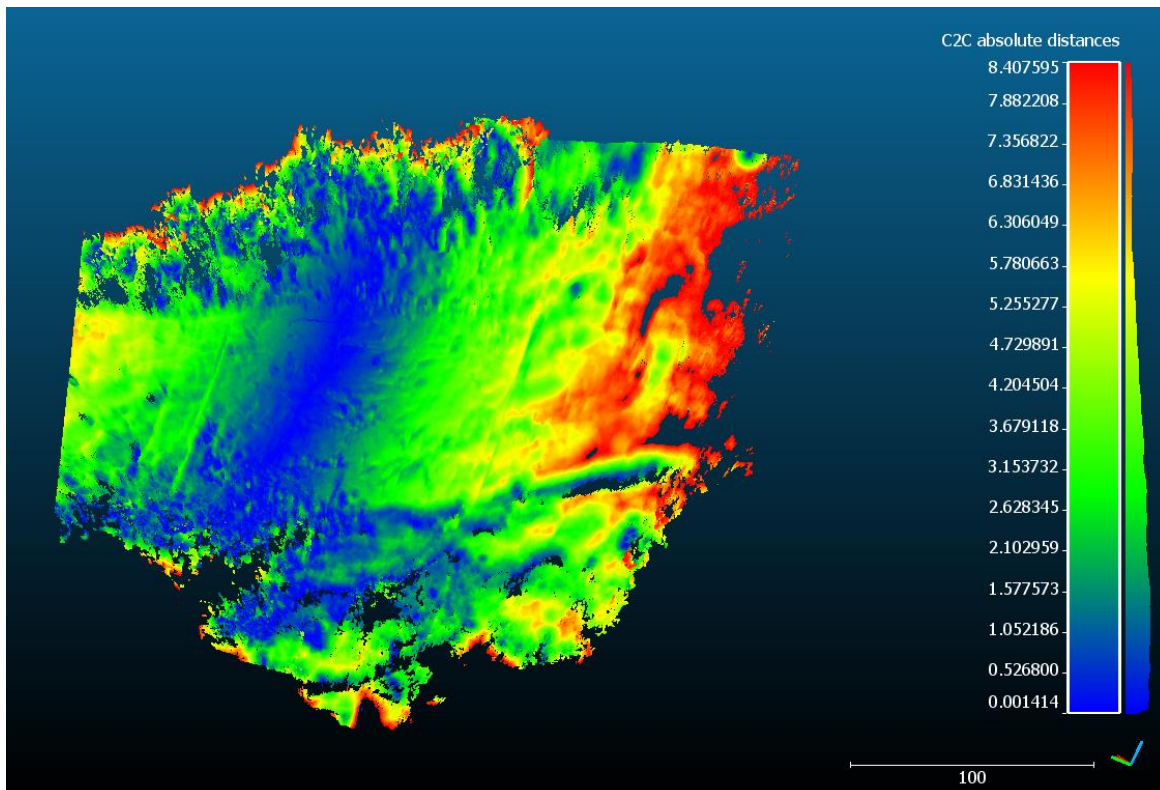
Figure 26 Cloud to cloud distance between Photogrammetry scans at site 2

7.5 Structural geological analysis

Presented in this chapter is the compiled results of the structural geological analysis done at site 1. Main joint set identification from Stereo nets are presented in (7.1.1) followed by the kinematic analysis (7.1.2). Finally, the scanline survey and block size measurements are presented in (7.1.3).

7.1.1 Main joint set identification

Stereo nets easily visualize the data gathered for identifying main joint sets. Each joint set is named by the first number indicating which dataset the stereo net is made from: 1 = field data, 2=digital data, 3= combined data. The second letter indicates weather a the fractures in the set are foliations (F) or joints (J). Foliation refers to repetitive layering in metamorphic rock, which in my wall represents relatively horizontal fractures. Joint represents the other fractures in the wall that with more vertical angles. The last number is the set number within the same stereo net. Example: 3J2 is the second joint set from the combined data.

Field data

Data from 140 measurements were plotted in Figure 27, and it can be subdivided into five joint sets.

Variation and confidence level of the main joint sets are given as two standard deviations (Table 8). Joint set F1 is considerably more horizontal than the other planes and is likely defined by the foliation in the rock wall. The set dips 16.5° and has a direction of 109°. 1J1 is the most densely plotted set with the lowest variation of 11.6°, and it is directed at 30 degrees and dips at 88.4°. 1J2 has similar dip to 1J1 but faces in a slightly different direction of 14.1°. 1J3 is the set with the most measurements (32 poles) but as seen in the stereo net, it is quite sparsely distributed with a variation of 27.4°. In contrast 1J4 only has seven poles and is the least represented set, variation is also high here (27.4°). One and three standard deviations including a confidence level of 50% can be found in the appendix (Appendix x).
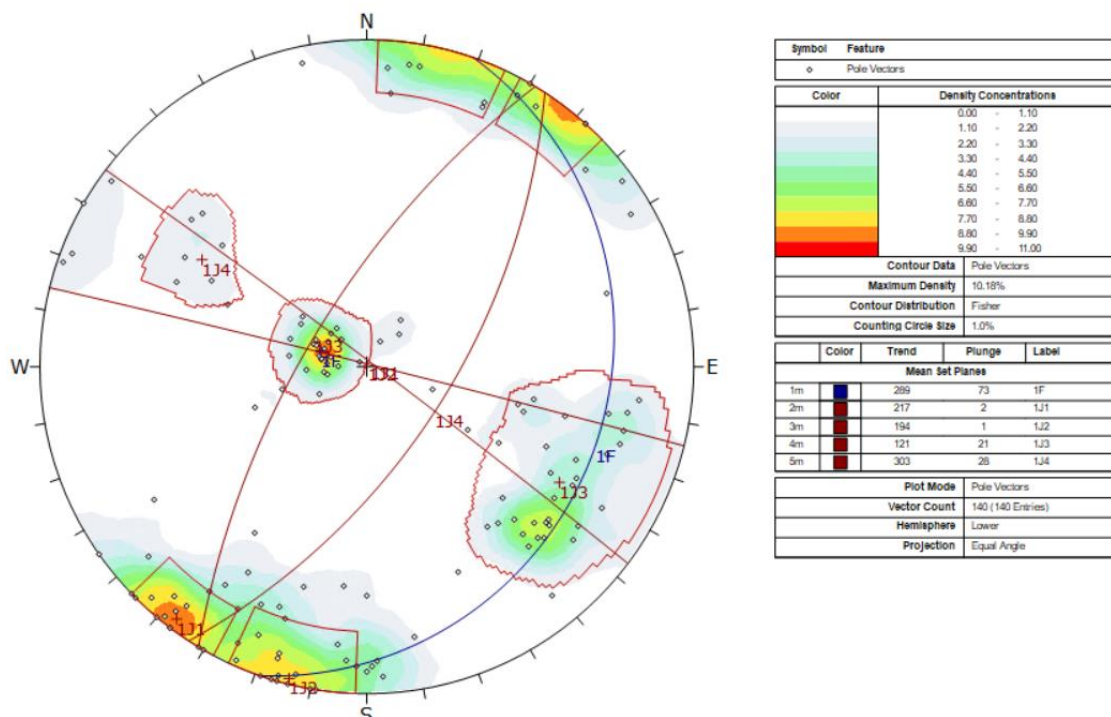
*Figure 27: **Stereonet 1** presenting a scatterplot of the dip and dip direction data measured in the field. Five mean joint sets (1F,1J1,1J2,1J3 and 1J4) can be identified from the available data where one has foliation like features (1F).*

Table 16 shows the dip and dip direction mean of each main joint set found in the stereo net including variability and confidence values at two standard deviations.

Table 16: Variability limit: the Variability here means that any pole in this group has a two standard deviations (i.e. 96%) probability to fall within that many degrees of the mean value. Confidence Limit: means that one can be two standard deviations (i.e. 96%) confident that the true mean is within that many degrees of the calculated mean.

Label	Planes	Dip	Dip Direction	Variablity limit at two standard deviation	Confidence limit at two standard deviation
1F	24	16.52°	109.01°	14.59°	2.98°
1J1	19	88.42°	36.96°	11.62°	2.67°
1J2	23	89.21°	14.09°	15.89°	3.32°
1J3	32	68.72°	300.92°	27.36°	4.88°
1J4	7	62.24°	123.28°	27.36°	4.88°

LiDAR data

Five main joint sets were identified from 179 orientations of planar structures using lidar data and are presented in stereo net 2 (Figure 28). Joint set 2F has a dip of 10.8° and a direction of 135°. It consists of 51 planes with a variability of 22.5° (Table 10). Set 2J1 includes 59 planes and is consistent with set 1J2 from the field data. The three following sets 2J2, 2J3 and 2J4 are based on only a few planes each, five, five and six respectively. Set 2J2 at (79.45/324.82) and 2J3 (75.79/295.60) are relatively close to 1J3. Set 2J4 with a direction of 244.99° and a dip of 84.25° is not represented by the field dataset, it is the set in this data set with the lowest variability at 7.9°. More measurements are needed for joint set 2J2, 2J3 and 2J4 to validate if these are indeed of significance. Joint set 2F show similar results to 1F and are likely to be following the foliation.
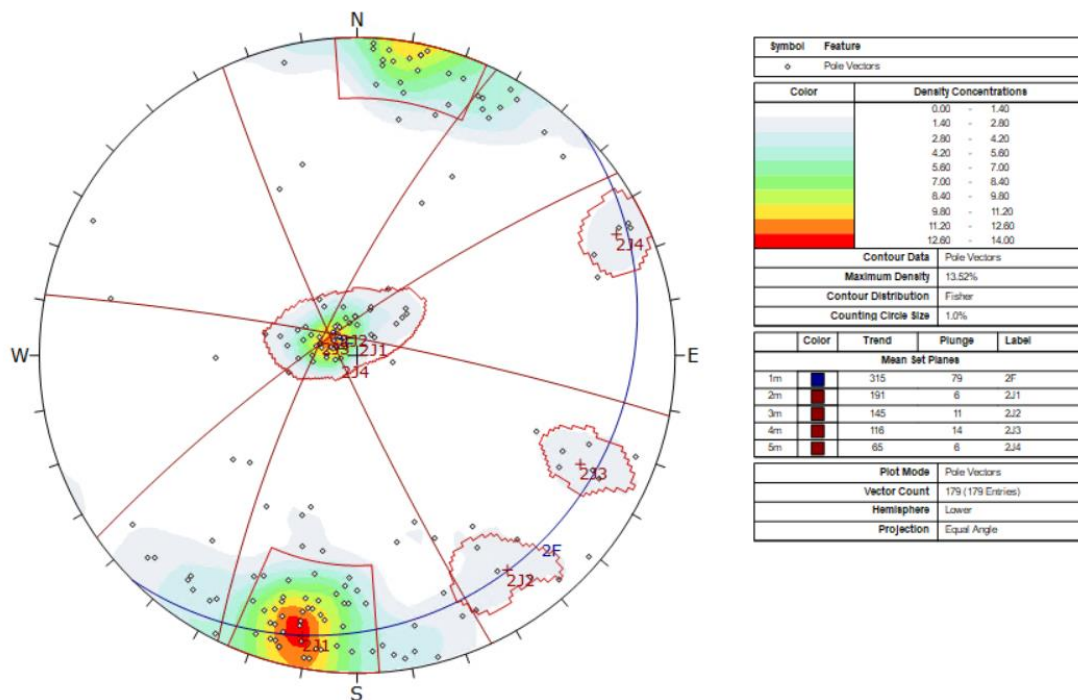
*Figure 28: **Stereonet 2** Showing density concentration of the poles of the planes. Five main joint sets (2F, 2J1, 2J2, 2J3 and 2J4) can be identified from the data where 2F seems to be representing a foliation in the rock wall.*

Table 17: Statistics for stereonet 2 (LiDAR data) showing variability and confidence limi of each joint set at two standard deviation. One standard deviation, three Standard deviation and a 50% value can be found in the appendix.

Label	Planes	Dip	Dip Direction	Variablity limit at two standard deviation	Confidence limit at two standard deviation
2F	51	10.78	135.08	22.508°	3.1705°
2J1	59	84.35	10.54	18.0051°	2.35301°
2J2	6	79.45	324.82	15.2757°	6.25076°
2J3	5	75.79	295.60	9.12635°	4.08468°
2J4	4	84.25	244.99	7.90306°	3.95374°

Combining field and Lidar data

The combined stereo net was made by combining the field data (140) measurements, the LiDAR data (179) measurements and an additional 53 measurements of fractures along the

scanline survey. These data in combination give us the basis of better identifying the main joint sets of the rock wall. We can identify four main joint sets: 3F (69/12.26), 3J1 (88/35), 3J2 (84/11), and 3J3 (73/305); (Figure 29).

Each set is well represented here with 3J1 having the least entries of 35. When looking at joint sets from the two datasets separately and comparing results with the combined joint set (table 18) we can see that joint set 1J4 and 2J4 are the two joint sets that does not fall within the mean joint sets of the combined data. Based on this these two sets can be identified as secondary joint sets, but not main joint sets because they are not very well represented by open fracture.
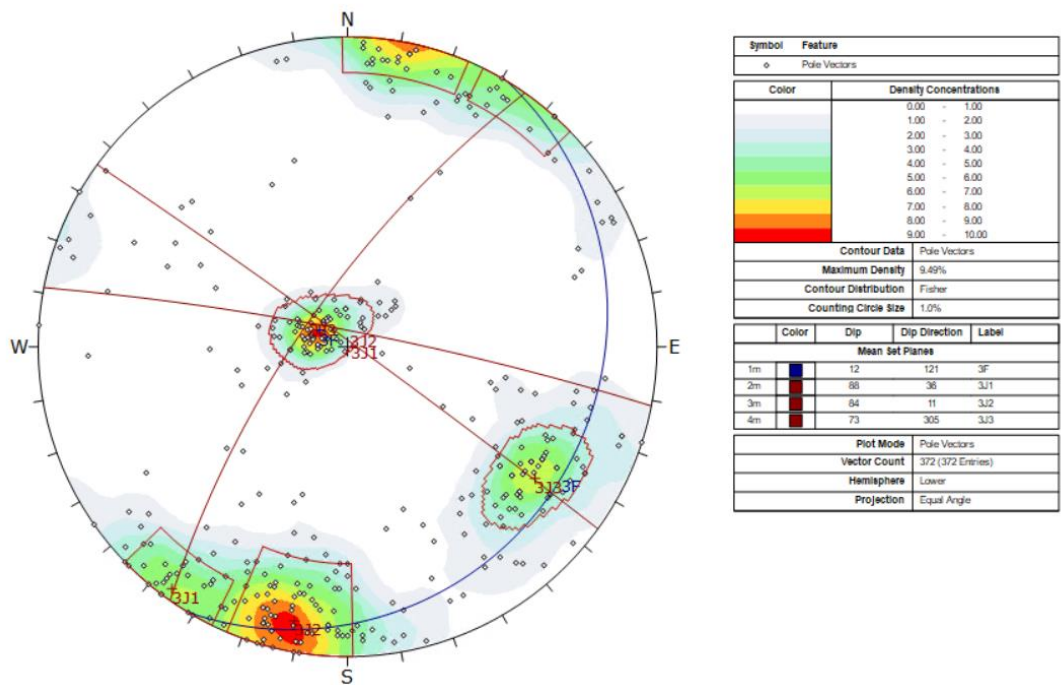
Figure 29 Stereonet of combined data sets. With more data its much more clear where the main joint sets can be found.

Table 18: Statistics of main joints sets from stereo net 3 (Combined data)

Label	Poles	Dip	Dip Direction	Variability limit at two standard deviations	Confidence limit at two standard deviations
3F	69	12.26	120.91	16.8436°	2.03452°
3J1	37	88.21	35.84	13.2614°	2.18462°

| 3J2 | 79 | 84.06 | 10.92 | 16.5997° | 1.87369° |
| 3J3 | 51 | 72.61 | 304.67 | 14.7448° | 2.11176° |

7.6 Kinematic analysis

The summarized results for the kinematic analysis from the dataset consisting of 372 measurements are found in this section. This analysis is based on the data combining all individual measurements of dip and dip direction. Eight planes meet the conditions of normal planar sliding (2%). Toppling has a bit higher values where 25 planes (6.72%) allow for flexural toppling and 28 planes (7.52%) allow for direct toppling. This suggest that toppling is a possible failure mechanism at site 1 more so than planar sliding. From the analysis, the potential for failure appears to be highest for wedge type sliding (Table 20). The findings of the kinematic analysis can be visualized in Figure 30 and 31. 68,984 intersections between planes were identified by the whole dataset. 19,992 of intersections are between planes belonging in the main joint sets, and the kinematic analysis are based on these. (2.92%) of the 19992 intersections have critical values were sliding between two planes is possible. An additional 114 plane intersections allow for wedge sliding on one plane (critical 2). This seems very little in terms of percentages, however most of these intersections are between joint set 3F and the other three planes where no values are critical. By looking at the values between the set planes where critical values occur, we find that 50 of 1813 (2.76%) intersections between plane 3J1 and 3J3 have critical values. 200 of 3871 (5.17%) are critical intersections between plane 3J2 and 3J3. The highest values are found between plane 3J1 and 3J2 where 333 of 2923 (11.4%) intersecting planes have critical values.

Symbol	Feature	
▫	Critical Intersection	

Kinematic Analysis	Wedge Sliding		
Slope Dip	70		
Slope Dip Direction	0		
Friction Angle	30°		

	Critical	Total	%
Wedge Sliding	6401	68984	9.28%

Plot Mode	Pole Vectors
Vector Count	372 (372 Entries)
Intersection Mode	Grid Data Planes
Intersections Count	68984
Hemisphere	Lower
Projection	Equal Angle
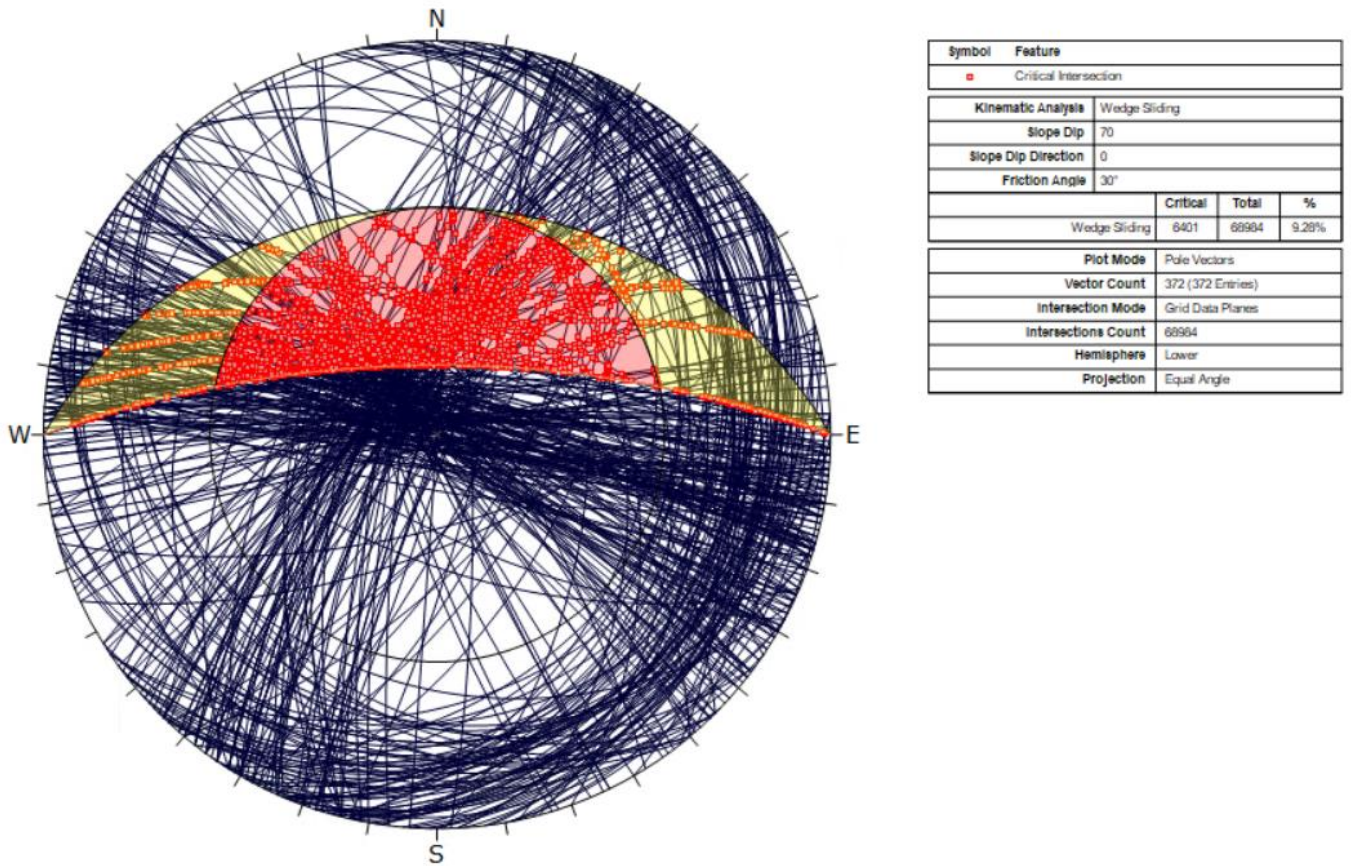
Figure 30: Stereo net of kinematic analysis for wedge sliding. Red areas show primary critical zone (Critical 1). Intersections that are plotted in this area represent wedges that fulfill kinematic and frictional conditions for sliding. Yellow area represents secondary critical zone (Critical 2). If intersections are plotted in this zone it means that one of the wedge planes has a more favorable orientation for sliding then the line of intersection of the wedge, and sliding on one plane can occur. The results in this figure show critical intersections based on all intersections in the dataset.
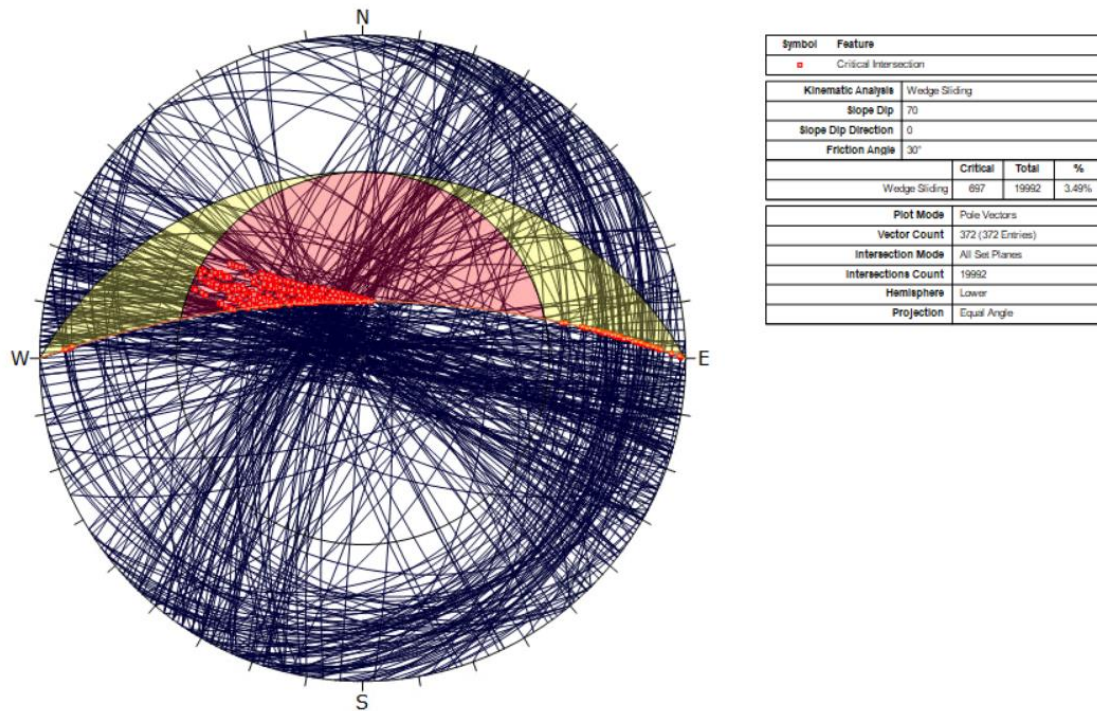
Figure 31: Stereo net of kinematic analysis for wedge sliding. 697 intersections between planes belonging to main joint sets have critical (583) or secondary critical (114) values. The results in this figure show critical intersections based only on intersecting planes that are part of the main joint sets.

Table 19 Planar sliding

Planar Sliding	Critical	%	Total
All Vectors	8	2.15%	372
Set 3: 3J2	1	1.27%	79

()Table 20: Wedge sliding statistics. Critical 1 = wedge sliding (both planes). Critical 2 = wedge sliding (One plane). It has to be noted that the percentages are based on the total intersections in each intersection type. For instance only 2.92% of the planes in (Intersections in set Planes) are primary critical, this is because there are 19992 intersections of planes included in the main jointsets and 583 of these have primarary critical values. Between jointset 3J1 and 3J2 there are only 2923 intersections of planes, 333 of these are critical and we come out with

11.39% much higher then the total number because most of the critical values is found between these sets, but the total intersections between planes are much lower.

Intersection Type	Critical 1	%	Critical 2	%	Total
All Intersections	5280	7.65%	1121	1.63%	68984
Intersections in set Planes	**583**	**2.92%**	114	0.57%	**19992**
Set 1: 3F vs Set 2: 3J1 Planes	0	0.00%	0	0.00%	2553
Set 1: 3F vs Set 3: 3J2 Planes	0	0.00%	51	0.94%	5451
Set 1: 3F vs Set 4: 3J3 Planes	0	0.00%	0	0.00%	3381
Set 2: 3J1 vs Set 3: 3J2 Planes	**333**	**11.39%**	28	0.96%	**2923**
Set 2: 3J1 vs Set 4: 3J3 Planes	50	2.76%	0	0.00%	1813
Set 3: 3J2 vs Set 4: 3J3 Planes	200	5.17%	35	0.90%	3871

Table 21: Flexural toppling

Flexural Toppling	Critical	%	Total
All Vectors	25	6.72%	372
Set 3: 3J2	15	18.99%	79

Table 22: Direct Toppling, Critical 1= Direct Toppling (intersection). Critical 2=Oblique Toppling (Intersection)

Intersection Type	Critical 1	%	Critical 2	%	Total
Grid Data Plane Intersections	759	1.10%	4883	7.08%	68984
All Set Planes	40	0.20%	1083	5.42%	19992
Set 1: 3F vs Set 2: 3J1 Planes	0	0.00%	0	0.00%	2553
Set 1: 3F vs Set 3: 3J2 Planes	0	0.00%	0	0.00%	5451
Set 1: 3F vs Set 4: 3J3 Planes	0	0.00%	0	0.00%	3381
Set 2: 3J1 vs Set 3: 3J2 Planes	40	1.37%	700	23.95%	2923
Set 2: 3J1 vs Set 4: 3J3 Planes	0	0.00%	10	0.55%	1813
Set 3: 3J2 vs Set 4: 3J3 Planes	0	0.00%	373	9.64%	3871
User and Mean Set (Unweighted) Plane Intersections	0	0.00%	0	0.00%	6
User Plane Intersections	No results				
Mean Set Plane (Unweighted) Intersections	0	0.00%	0	0.00%	6

7.7 Scanline Survey

Along the scan line observations intersecting the measuring tape were registered. Observations consisted of fractures, foliation like fractures, continuous fractures, open fractures, including a potentially unstable area (Table 13). 51 observations were registered and a total of 53 measurements were done, some large fractures were measured multiple times along the 22.5-meter-long scan line while other features were unable to be measured with a libellee compass. Interval and distance at which similar fractures within the same joint sets repeated could be interpreted from the observations. The most abundant joint set represented in the scanline was 3J3 (72.6/204.6). 22 out of 53 observations had similar values to this set. By looking at the interval of these fractures where they were not interrupted by fractures of other joint sets, I found 15 observations. The distance ranged from 5cm to 1.5 meters. 10 of the 15 intervals observed were between 30 and 60 cm long.

Six fractures along the foliation were measured with somewhat different dip and direction. A large open fracture was observed from 4.9m to 6.1m (Figure 32)

Figure 32 Open fracture from 4.9m to 6.1m on the measuring band.

A potentially unstable loose area was identified (figure 11). This area was defined by a wedge with two planes. Three measurements were done from plan A and five from plan B. the final

values were calculated by the mean dip and dip direction measured from each plane respectively: Plane A (74/303.3) and plane B (84.4/14).

Table 23: Complete overview of measurements along the scanline survey. Orange bars mark the planes defining the potentially unstable area. Some fractures were to narrow to get good measurements with the compass with libelle these are marked with N/A (not available) other features were larger and more than one measurement was needed. All measurements was done with emphasis on measuring stable areas that was real representations of the joint sets of the wall.

Length along meassuring tape (M)	Dip	Dip Direction	Feature
1.60	N/A	N/A	Fracture
2.65	64	308	Fracture
3.55	64	308	Fracture
3.60	12	142	Fracture along the Foliation
4.90 – 6.10	90/80	288/324	Open fracture
6.60	72	300	Fracture
6.80	80	328	Fracture
7.35	72	322	Fracture
7.75	20/40/28	50/78/52	Fracture along the foliation
7.95	70	306	Fracture
8.54	68	308	Fracture
8.70	68	308	Fracture
9.30	60/72/72	284/302/294	Fracture
10	N/A	N/A	Fracture
10.80	86/84/84/86/84	26/16/04/02/24	Fracture defining the potentially unstable area (plane B)
10.85	72	310	Fracture
11.20	88	38	Continuous fracture
11.20 – 12.10			Vegetation
13.20	N/A	N/A	Fracture
13.30	76/60	300/304	Fracture
13.70	76	300	Fracture
13.90	82	30	Fracture
14.10	62	306	Fracture
14.50	N/A	N/A	Fracture

14.85	70	302	Continuous fracture
15.35	70	302	Fracture
15.50	70	302	Fracture
15.80	78	306	Fracture
16	72/78/72	304/306/300	Fracture defining the potentially unstable area (Plane A)
16.20	80	304	Fracture
16.25	82	298	Fracture
16.95	82	298	Fracture
18.05	N/A	N/A	Fracture
18.20	Ice	Ice	Fracture
19.20	86	38	Fracture
20.05	74	284	Fracture
20.25	N/A	N/A	Fracture
20.35	76	314	Fracture
20.40	12	208	Fracture along the foliation
20.90	N/A	N/A	Fracture (quartz)
21.10	N/A	N/A	Fracture
21.50	90/80	94/88	Continuous Fracture
21.70	2	30	Fracture along the foliation + ice
21.90	80/88	50/48	Fracture
22.50	N/A	N/A	Fracture
22.60	N/A	N/A	Fracture along the foliation
23.25	70	314	Fracture
23.80	90	N/A	Continuous fracture
24.00	86	108	Fracture
24.30	68	304	Fracture
24.30	N/A	N/A	Fracture along the foliation
24.50	86	288	Fracture
24.80	86	288	Fracture

7.8 Block size measurements

Block sizes were measured in varying sizes from about 0.00432 cubic meters to 1.6 cubic meters (Table 14). There are quite few samples from the block size measurements there that keep coming back. The Intermediate- and short-axes often represented values between 20-

40cm, while the long-axis was highly variable from 30 to 190cm. This can indicate that there are main joint sets that have this distance within the wall (Citation missing) In the talus area we did find some blocks that were relative fresh indicating recent activity.

Table 24: Block size meaured in the field

Long axes (cm)	Intermediate axes (cm)	Short axes (cm)	volume dm3
70	25	20	35
40	22.50	20	18
30	18	8	4.32
60	20	10	12
180	120	45	972
120	100	50	600
90	70	25	157.5
70	60	25	105
60	30	30	54
60	50	40	120
110	40	30	132
80	40	27.5	88
130	37.5	30	146.25
65	45	20	58.5
190	100	85	1615
120	60	40	288
100	65	20	130
100	80	50	400
65	45	30	87.75
50	30	25	37.5
60	40	28	67.2
90	70	40	252.
50	45	30	67.5
			Range: 4.32 – 1615

7.9 Volume estimation of the possible unstable area

The volume of the possible unstable area was estimated from LiDAR and Photogrammetry. Based on LiDAR the area was calculated to 22.66 cubic meters (Figure 33A). The unstable area

of the photogrammetry cloud was calculated to 19.78 Cubic meters using the same parameters shown in the volume calculation for LiDAR (Figure 33B). When comparing the two figures we can see that the LiDAR volume is slightly larger. The relative height from the ground plane in this case plane B shows higher values for LiDAR (1.87m) than for Photogrammetry (1.67m). This in turn results in a difference of volumes of the entities of 2.88 cubic meters. These results are consistent with the difference in the large models where some areas are up to 25 cm apart.
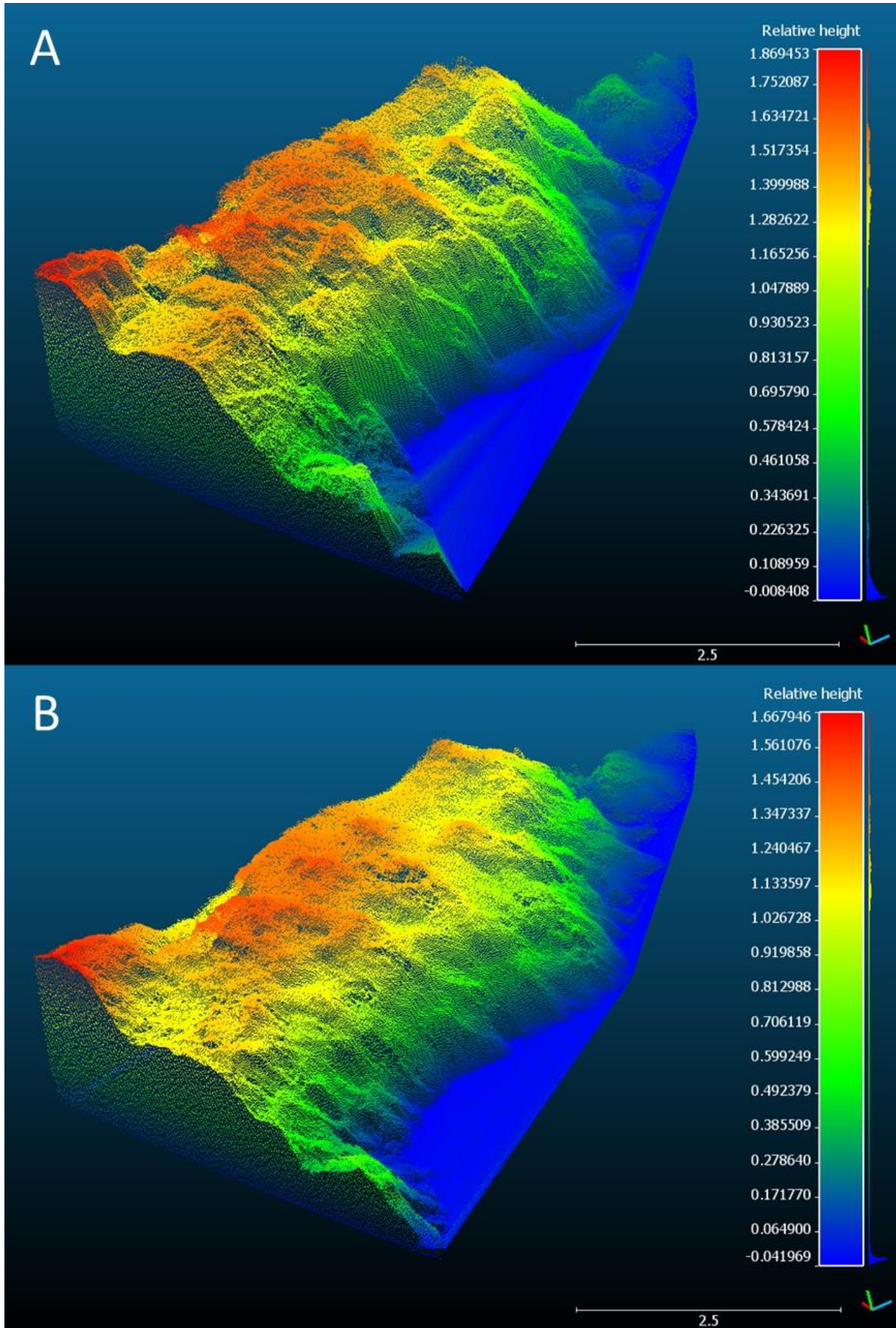
Figure 33: The unstable area was calculated by LiDAR and photogrammetry. A: Possibly unstable area showing made from LiDAR 3D model. The colors represent height of the unstable are relative to one of the planes defining the area. B: The same possibly unstable area made from photogrammetry 3D model.

8 Discussion

The discussion of this study is divided into four sections. In section (8.1) I will be discussing the results of the LiDAR scanning, in (8.2) I will discuss Photogrammetry results. (8.3) Will be focused on comparison of the two methods. I am discussing different aspects of LiDAR and photogrammetry with a focus on method application, including opportunities and challenges of each method. Part (8.4) will regard the potential rockfall at the site and discuss the possibilities around a warming climate and its effect on rock walls, Site 1 in particular.

8.2.1 LiDAR

LiDAR has become a widely applicable technology that allow for high accuracy remote data acquisition. In this chapter the application and challenges in relation to data acquisition of natural rock walls will be discussed. Furthermore, the discussion expands on data acquired from this study and relevant literature regarding their usefulness in terms of accuracy, reliability, and their application in the field.

Comparison of LiDAR clouds sampled in November 2020 and April 2021 at Site 1 showed small deviations generally ranging from zero to two cm. At Site 2, the comparison of LiDAR clouds had larger deviations generally ranging from zero to 50 cm but differences as high as 1 meter were observed at edges of the models. What makes results for LiDAR at site 1 considerably better then at site 2. It must be assumed that either the approach while gathering data, or the conditions at either site has influenced the data in some way that can be explained by investigating the matter. The most important parameters that influence the quality of datasets acquired by TLS systems are resolution, accuracy, maximum range, and survey set-up. (Abellan, et al., 2013) Naturally differences in these parameters may have influenced data acquisition and may or may not explain the different results.

The most apparent difference between Site 1 and Site 2 is the rock walls sizes. The area of the rock wall at Site 1 was estimated to 3,500 square meters, while site two is about 25 times larger covering an estimated area of 90,000 square meters. Not only is the wall much larger

but the distance of the scanner to the furthers points in their respective rock walls are over 400 meters at site 2 while only about 100 meters at Site 1. How can this influence the quality of the results of LiDAR data differently at the two sites?

The same scanner of type RIEGL VZ-1000 was used for all setups at both sites and the same resolution was used for every scan. Distance to the wall mostly influence the point density of the clouds and can also have an effect of the beamwidth that get slightly larger at longer distances. However, the scanner has a range of 1,400 meters and collecting data between 0 – 400 meters is likely not the cause of these larger errors.

However, the range of instruments are normally provided by the manufacturer. It is usually presented as a maximum distance for a high reflectivity surface (i.e., 1200m for 80% reflectivity). However, surfaces such as natural rock is normally characterized by a reflectivity of 20%. This surface is usually only capturable within half of the 80% reflectivity distance. (Abellan, et al., 2013) By applying this assumption to our instrument, the range would still be 700 meters well over the distances scanned at site 2.

Resolution was considered to not be a problem of the difference in quality of data because the observed detail of the separate clouds made with LiDAR at sit 2 were of good quality. Resolution is often understood as the spacing between measured points reliant on the distance of the scanner and the scanned object as well as the angular spacing set for the instrument (0.01 per degree).

However, a characteristic for TLS instruments like the laser scanner used in my study is that the increasing diameter of laser beams increases linearly with increased distance due to beam divergence. Because of this resolution depends not only on the spacing between each beam but also on the diameter of the beam called spot dimension. (Pesci, Teza, & Bonali, 2011) Because of beam divergence the spot dimension can be much larger than the point spacing leading to unnecessary data redundancy at longer distances. (Shan & Toth, 2018). An example of compromise of accuracy and precision with range (i.e. 1 cm at 0.1 km and 2 cm at 2 km for ILRIS-3D device) (Lichti & Jamtsho). RIEGL VZ-1000 however has an accuracy of 8mm and precision of 5 mm up to 1400 meters if conditions are ideal. In turn this does not explain a difference of 50 cm between 3D models.

With long experience of laser scanning the accuracy of laser scanning has a range of a few millimeters. (Ingensand, 2006), (Eltner & Baumgart, 2015) found that the usage of a well measured and calibrated reference system ensures accuracy of 7 mm over a 2*1000m^2 area.

(Yogender, Raghavendra, & Kushwaha, 2020) Found that accuracies of 3D models taken by a building from a 10–15-meter distance ranged from 9mm when using GCPs as reference to 3.3 cm when no georeferencing the cloud. Thereby stating that GCPs are essential in precise and effective co registration of 3D point clouds.

The installation of ground control points was used for the main purpose that clouds could be compared. However, GCPs have been installed in very different matters at the two sites. While 13 GCPs at site one is well distributed all over the rock wall at site 1, Site 2 only has Five. Not only are there considerably fewer targets especially when considering the area of each rock wall, but the targets at Site 2 are only installed in a tunnel entrance area and not distributed evenly in the rock wall. Could this explain the differences in results of point cloud comparisons from November 2020 to April 2021?

GCPs should be installed in a way that they do not appear in the same plane. (Kemeny & Turner, 2008) The location of the installed GCPs location is therefore very likely to have influenced the large differences between the LiDAR models made at Site 2.

Quality of data decrease with distance and can also be influenced by weather conditions such as fog and rain that can lower reflectivity of objects and in some cases solar irradiation (Olsen & Stuedlein, 2010). However, conditions were relatively similar at the two scan times with clear skies and sunny weather. Field days were picked with caution regarding weather forecasts and optimal conditions for scanning. Influence on atmospheric conditions should have very little influence on the results.

While two scan positions were used at Site 1 and only one scan position was used at site 2 this does not affect the differences observed from the results of differences of LiDAR clouds at site 2.

The question at hand is if the cloud-to-cloud tool in cloud compare could have impact on these results and in what regard. The tool simply computes the nearest neighbor distance Using a Hausdorff distance algorithm () This means that distance between points between 3D models

in this case point clouds is determined by the furthest point in one cloud to the closest point in the other cloud (Figure 3). This ensures that points are not falsely computed too well. However, with increasing resolution this computation can result in distances being overestimated as well.
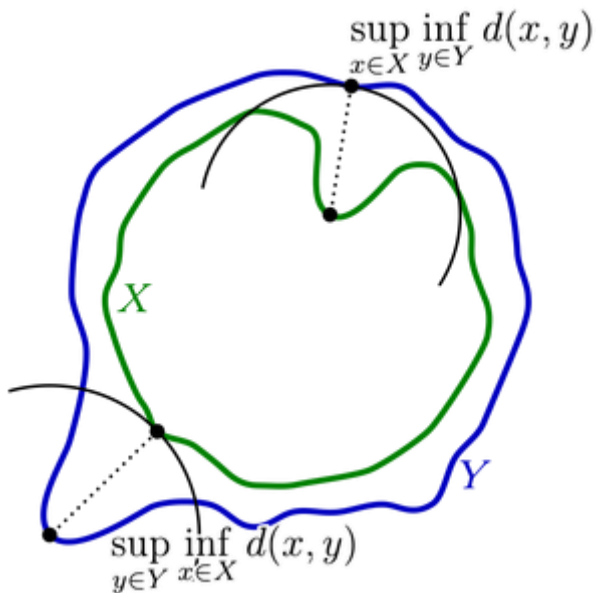
Figure 34: Principle of Hausdorff distance. Hausedorf between the blue and the green line shows that the furthest distance of the closest point is determined as the distance.

Alternatively point to mesh distance have been proposed as a better comparison tool. In particular Iterative closest point (ICP) algorithms have been warned against because it assumes that points shortest distance form one another in two different models represents that same point and this may not be true (Figure x). Typically point to mesh distances yield better results (Olsen & Stuedlein, 2010).
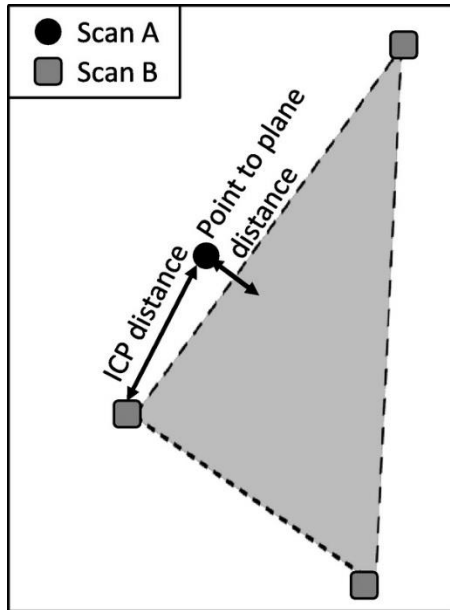
It is likely to presume that the targets located at tunnel entrance area at Site 2 can explain the large errors. First, from examining the Distance between the models we can see that distance between the two clouds increase the further you get towards the top right of the models. It is unlikely that errors of factors as atmospheric conditions and the cloud-to-cloud tool would appear in this manner. However, they might play a smaller role. One thing underlining the issue with targets only in one area of a model comes with the registration of the individual clouds. When georeferencing the scan done on November 26th, 2020, the GCPs in the 3D models matched the coordinate points with three to four millimeters error. In comparison the scan done on the 17th of April 2021 matched with errors of 0.8 to 1.6 centimeters. Even though these are relatively small errors the difference can lead to larger errors when comparing the

model at a distance further from the GCPs (Figure 35). As we can see the distance is relatively low close to the GCPs but gets larger further from them.
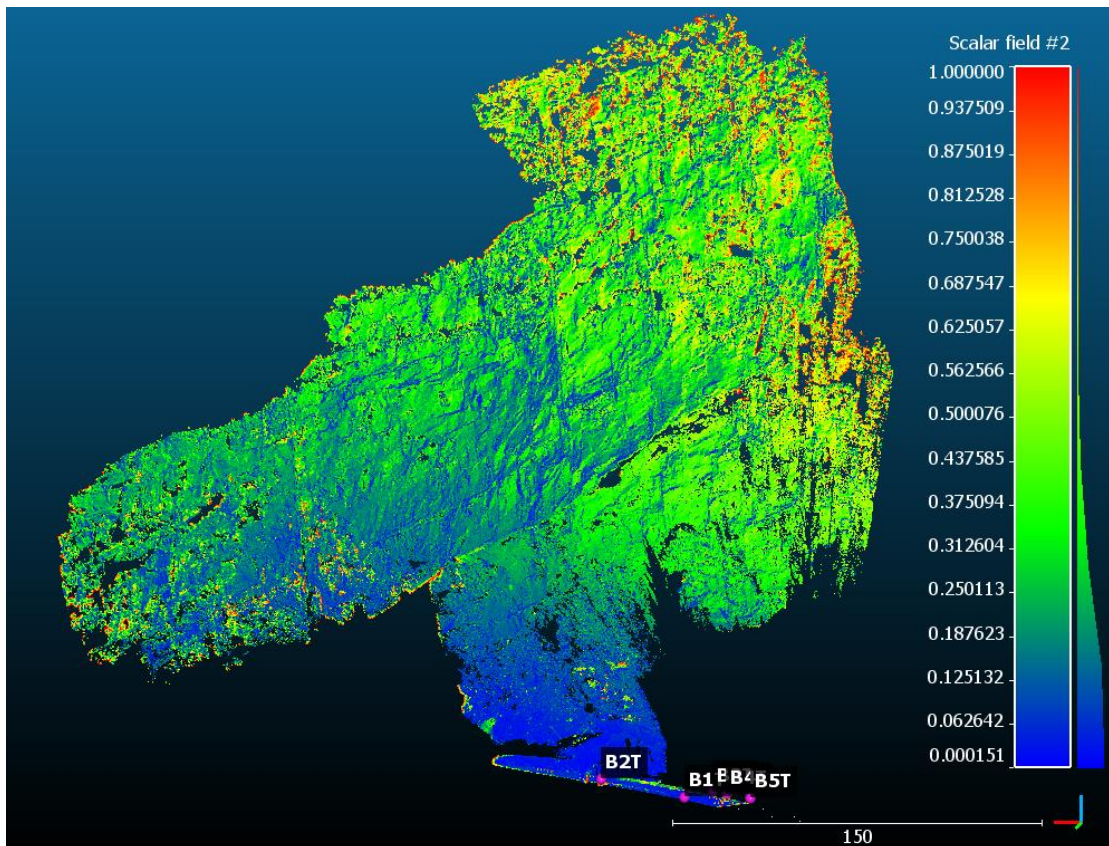
Figure 35

One of the major reasons terrestrial laser scanning (TLS) was used in this study was because of its potential to detect slope movements over a larger area rather than just a single monitoring point. In addition, 3D point clouds provide high resolution models of the topography and there is potential for extracting data of relevant structures form the point clouds. (Oppikofer, et al., 2009) This was utilized when deriving dip and dip direction measurements from otherwise inaccessible areas of the rock wall at Site 1.

8.2.2 Photogrammetry

(Bolognesi, et al., 2014) found by comparing point clouds from photogrammetry and TLS and control points by total station that agreement between the point clouds did not exceed 3 cm. However, when computing photogrammetry point clouds there are many factors that play a major role in the accuracy such as orientation and overlapping of images, digital and optical performance of the camera, scale, the photometric processing code, and its parameters. A Different study found that high quality 3D models can be achieved with appropriate light

conditions and a large set of images. (Koutsoudis, et al., 2014) The Popularity of photogrammetry for 3D documentation and recording is on the rise due to the decreasing processing time a formerly weak point of photogrammetry due to advances in computation techniques and algorithms. The position and popularity of this approach in the 3D digitization field is also strengthened due to its cost-effective solution (Nocerino, Menna, Remondino, & Saleri, 2013). Photogrammetric techniques proved sensitive to changes in cliff face topography despite the challenges posed by scale and nature of the environment. This suggests that significant potential exists for the application of digital photogrammetry in mapping natural roc walls (Lim, et al., 2005)**.**

Because no changes were detected in LiDAR scans from November to April the appropriate judging tool for how well Photogrammetry performed was to see how well it represented the same Rock wall twice. At Site 1 the model from November and April had a relative distance to each other ranging from zero to 20 centimeters. At Site 2 georeferencing of the models showed difficulties and this resulted in models difficult to compare properly, however distances was measured over several meters. This underlines the importance of using well distributed targets over a surface to properly georeference models that help achieve and validate desired reliability of the data.

By comparing models from two different time periods, we get an indication of the Accuracy and precision of the method, following the approach in this thesis. However, by looking at the individual developments of each model we can see that already by georeferencing the models we see considerable differences in coordinates matching GCPs. However, can the differences in the models at site 1 mostly ranging from zero to 20 cm can be explained by this?

The photogrammetry model at Site 1 where images were taken on the 26th of November 2020 some coordinates match their GCPs very well while others do not. GCPs B14, B13 and B3 have errors of 39cm, 23cm and 27 cm, respectively. To see if these errors at the georeferencing stage of making models can explain the overall difference between the models we investigate and compare the errors of the same targets in the model made form photos taken on the 17th of April. GCPs B3, B13 and B14 in the models made from photos taken on the 17th of April 2021 at Site 1 has lower errors of 1.7 cm, 3cm and 3cm, respectively.

The differences at these GCPs can be observed in the 3D models in the same areas (Figure 36). We can see that the models have a smaller distance between them towards the middle section, areas are further apart around B14 and B3 as expected. B14 is on the very edge of the model and might have been beneficial to not include this point in the modelling due to its high error in the model form the 26th of November. To further validate the hypothesis that these errors can translate to the models we can compare errors of GCPs that have lower differences and see if areas of the models including these GCPs show lower differences. B7, B9 and B10 have the lowest errors from the model form 2020, These errors are even lower in the 2021 model. All three of these GPs run through the section of the models that have the lowest distance and supports the hypothesis.
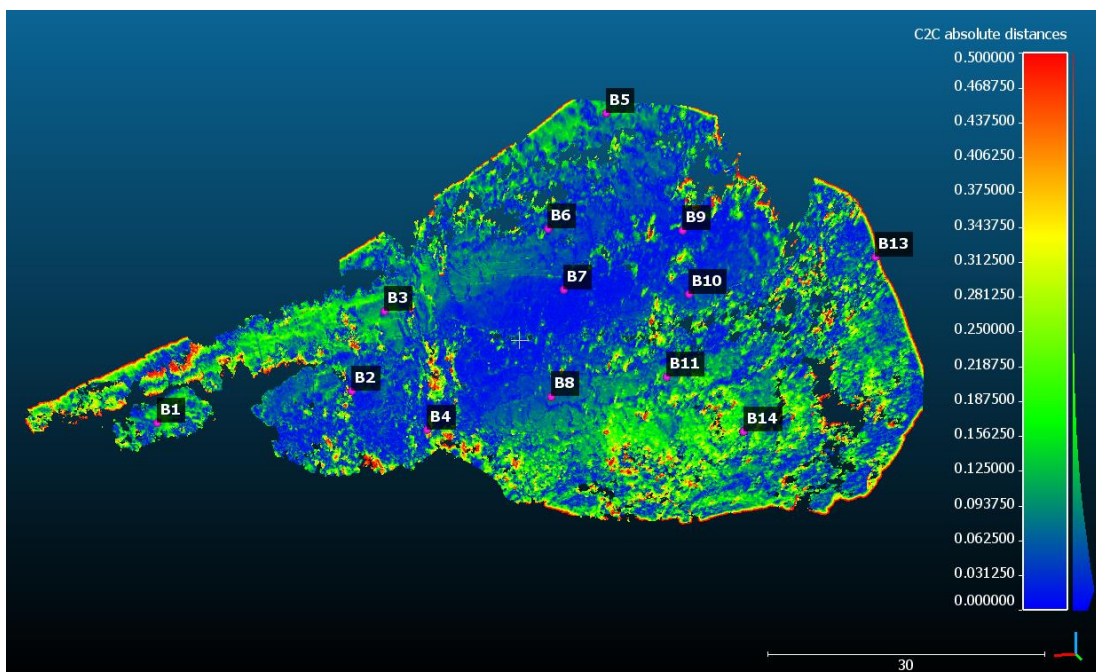
Figure 36: Comparison of photogrammetry models made at Site 1 with GCPs.

The question at hand is what makes the models match so differently to their targets? Why does the Coordinates match so differently between the two models? 125 photos were used in the first model while only 95 photos were used in the model performing the lowest errors. The same camera was used with the same camera settings. The question remains, what parameters play a major role at this stage of the development of 3D models using photogrammetry that could cause these differences.

Bright conditions and small amounts of blur existing in images can cause image degradation (O'Connor, 2018) Though it is not a well investigated point by research it is worth mentioning that photos are not taken from the exact positions between the two 3D models. The middle section is naturally better presented in both image sets could under representations of photos and simple slightly different camera positions cause errors as high as 20-30cm? This is yet to be answered as no it was difficult to find reported research on this.

8.2.3 Comparing LiDAR and Photogrammetry

By investigating and comparing results from LiDAR and Photogrammetry I observed that LiDAR performs better at making a 3D model of a rock wall at different times, thus representing the same surface of the rock wall twice. LiDAR had a difference of around 0-2cm difference between 26th of November 2020 and 17th of April 2021. Photogrammetry performs worse in this regard as differences ranged from 0-20cm at Site 1. Could we based on this say that the reliability of the LiDAR data is better than that of Photogrammetry because it was better at representing the same surface at different times in different 3D models?

To shed further light on this it is necessary to discuss the resolution and accuracy of each method.

The resolution of LiDAR is dependent on the equipment in particular the type of laser scanner. My scanner in particular has a range of settings where I used 0.01 degrees per point which was satisfactory for my study, however this setting goes all the way down to 0.0005 degrees per point witch would dramatically increase the point density as well as the processing time. To put it in perspective this would mean 2000 points per degree which would depend on distance from the scanner to the scanned object. Based on the manufacturers manual the scanner has an accuracy of 8mm and a precision of 5 mm up to 1400 meters if conditions are ideal (RIEGL, 2017).

When it comes to accuracy and resolution of photogrammetry it becomes a bit more complicated because it is highly dependent on the raw data used. The accuracy is directly related to the image resolution of the photos used to make a photogrammetry 3D model.

In other words, the detail of a 3D model cannot be better than the detail of the photos used to make the model.

One of the most important aspects regarding the resolution is the Ground sampling distance (GSD).

GSD is simply explained the distance between the centers of two pixels of an image measured on the object captured by the image. This is commonly meassured in millimeters per pixel and a GSD of 10mm/pixel would mean that one pixel in the photo represents 10mm in the real world. The GSD therefore depends on the resolution of the camera as well as the distance between the camera and the observed object and is a measurement of the detail that can be captured in an image.

In my study the photos captured has dimensions of 4928*3264 pixels. With very simple calculations the approximate detail in my photos can be determined. Each photo taken at my sites consisted of 4928 pixels in the horizontal direction, to capture an area of 100meter in the horizontal direction would result in a GSD of 25mm/pixel. In this case details below 25mm could not be captured and this would be the major limiting factor of detail on the photos. Naturally, 3D models made from these same photos could not capture details smaller then 25mm. However, because GSD is dependent on the distance from the camera to the captured object more detail can be captured by taking pictures closer to the object.

So, the question to ask is not how accurate photogrammetry can be, but what accuracy is needed, and how much effort is needed to acquire this accuracy compared to other approaches considering the scale of the project.

A Study making 3D models of a historical building had discrepancies under 3cm when comparing models made by Photogrammetry and LiDAR. 170 images were used, of an area covering about 3300 square meters. (Bolognesi, Furin, Russo, Pellegrinelli, & Russo, 2014)

Numerous Scientific publications are published focusing on the integration and comparison of photogrammetry and laser scanning and prove the equivalence of these techniques in achieving desired accuracy and reconstructing geometric detail. (Remondino, El-Hakim, Gruen, & Zhang, 2008)

(Skarlatos & Kiparissi, 2012) Studies show that the two different technologies perform results that can compete. However, when choosing an approach, it is not only the results that has to be considered when weighing methods.

In the field it took much shorter time and was much more convenient to use a handheld camera compared to setting up a laser scanner to let it scan the rock wall. Costs were also considerably lower as Laser scanners are still relatively expensive, and rent is usually higher than buying or borrowing a camera that is sufficient. Another point that was apparent in my thesis was the processing time used after data was gathered. LiDAR 3D models were already finished, the time consumed in preparing the models consisted of registration/georeferencing and filtering of trees. Photogrammetry 3D models had to be built in Agisoft. Building these 3D models took some time but most of the work was tied to the georeferencing. So how do we judge what is the best method? (Lato, Hutchinson, Gauthier, Edwards, & Ondercin, 2015) compared Laser scanning and Photogrammetry as well to try to pinpoint strengths and weaknesses of each method. by using a grading system from one to three they found that Terrestrial laser scanning performed better in spatial coverage. Photogrammetry had an edge when it came to remote accessibility and speed of deployment, they performed equally when mapping large scale changes, but terrestrial laser was slightly better at mapping small scale changes. On spatial resolution both technologies were graded with one, the highest score. In addition, affordability depended on the spatial footprint where smaller areas favored photogrammetry whilke larger areas favourd Terrestrial LiDAR. An interesting note was that when considering vegetation or tree cover, photogrammetry is the least desirable. (Lato, Hutchinson, Gauthier, Edwards, & Ondercin, 2015) The comparison of the two technologies highlights the different considerations when choosing one approach over the other. It is not so simple to say that one is better than the other.

In the first years of the 2000s computation techniques and algorithms in photogrammetry needing long processing time was a known weak point. New more efficient algorithms have been developed which have speed up image-based processing time and workflows. Photogrammetry has become increasingly popular underlining its cost-effective solution (Nocerino, Menna, Remondino, & Lunazzi, Accuracy and block deformation analysis in automatic UAV and terrestrial photogrammetry - Lesson learnt). By taking all into consideration its maybe not so odd that many studies have recommended the interdisciplinary use of these two methods. Where one falls short the other applies.

In 2004, very optimistic researchers even predicted that traditional surveying methods like tacheometry or close-range photogrammetry might have completely replaced by 3D scanning in the near future (Boehler & Marbs, 2004)

When considering the differences of both methods a combination of the two has the potential to complete each other's shortcomings. In general photogrammetry is found to be the best tool when an object mainly consists of point or line-based structures and Laser scanning is more suitable when objects are complex and irregular (Boehler & Marbs, 2004, p. 297-298). However, when study sites are large and complex both tools in combination can yield the best results (Remondino & El-Hakim, 2006).

8.2.1.5 Filtering

Filtering is one of the most time-consuming tasks at hand when preparing a point cloud for further analysis. I used 3-4 hours for each LiDAR point cloud and 10-20 minutes for photogrammetry clouds. When preparing a considerable amount of point clouds for further analysis these tasks require extensive and thorough work.

To isolate the surface area of interest in a point cloud, all extraneous points should be filtered out before analysis. Automatic algorithms that remove vegetation and other noise in point clouds have been proposed, alternatively 2.5D grids to remove Points below or over a mean elevation can be an effective tool in filtering vegetation. Although the task of cutting out vegetation and noise is straight forward, most automatic techniques struggle to filter out low laying vegetation. Low laying bushes and plants still needs to be filtered out manually and can be a time-consuming task. (Jaboyedoff, et al., 2012) I did all filtering manually with the scissor tool in Cloud Compare. The task at hand was time consuming but working with the tool for some time I developed techniques such as isolating densely vegetated areas that improved my efficiency. None the less for inexperienced and experienced users alike this is a time consuming but necessary job for further analysis of the point clouds.

8.1.1 Potential rockfall

The structural geological analysis at Site 1 betters our understanding of the geology at the scene and gives us information on potential rockfall. Potential rockfall is a complex theme and relies not only on the geologic conditions of a scene but also the external factors such as failure modes and failure mechanisms (Citation).

Inventories are the only direct approach to gather information about true hazard of an area (Volkwein, et al., 2011). By investigating historical records, we found that there has been at least 4 rockfall recordings at site 1 and one at Site 2 since 2000. Historically the prevention of rockfalls has been undoubtedly influenced and driven by rockfall activity especially events causing damage and injury.

Unfortunately, the availability of data at specific location can be very scarce and hazard cannot be determined by few events alone. However Conceptual frameworks that describe potential for instabilities in a rock wall can be given through investigation of internal parameters and external factors.

The potential rockfall depend on a range of factors that can be divided into preconditions, drivers, and triggers. Preconditions include Topography, geology, structures and their continuity, and permeability. Drivers and triggers are external forces that can be divided into Vegetation, climate and weather, infiltration, groundwater, earthquakes, human activity, animals and gravity. Time is also a factor that must be considered as natural processes and will eventually break down even rock due to chemical and physical weathering.

The potential for rockfall and presented interpretations are based on the structural geological analysis from Site 1 including kinematic analysis, scanline survey and block size measurements. In addition, weather data, historical records and observations at the site are key factors when considering rockfall potential.

A few key factors have been put emphasis in this discussion including Structures and their continuity in the rock wall, climate, and weather.

Numerous studies have investigated slope failure modes and uses kinematic analysis as a common tool. h**Ugyldig kilde er angitt.** However, it must be noted that a kinematic analysis only refers to the motion of bodies without taking account of forces acting on them. This means that conditions for sliding may meet critical values but sliding will not happen unless the body is free to move and not stabilized by other factors (Figure 42). A body of rock can act as a stabilizer meaning that other bodies of rock can be stable even if they are situated on a steeply inclined slope or on a low friction planes if there is no freedom for the body to move. Moving this body would in turn release the blocks sitting behind it that meet conditions for sliding (Kulatilake, Wang, Tang, & Liang, 2011).

The factor of safety

$$FS = \frac{resisting\ forces}{driving\ forces}$$

› FS < 1 → failure
› *Resisting forces:* shear strength of slope material, added strength (e.g. roots, cold ice), friction, etc.
› *Driving forces:* Gravity, added stress (e.g. seismic shaking, water pressure, roots)

Figure 37 Factor of safety of a slope where a value of 1 equals failure. Stability depends on the relationships between resisting and driving forces. As long as resisting forces exceeds driving forces failure will not happen.

The Kinematic analysis indicated that the least likely failure mode is planar sliding where eight planes have critical values. Flexural toppling has 25 planes that are critical, and 28 planes fall within critical values for direct toppling. Even though these values are smaller than wedge sliding, a failure by these modes cannot be ruled out.

Wedge sliding on the other hand looks at intersections between planes and many more possibilities appear. Now we are not looking at 372 planes but at intersections between planes that in theory could intersect (Table 13). There are a total of 68,984 intersections that in theory can intersect and a number of these have critical values that further can allow failure.

 The kinematic analysis however puts emphasis on the data within the main plane sets, likely because these are the joint sets that are likely to dominate the whole wall. However, this only includes 19,992 of the 68,984 planes and 583 intersections have critical values for wedge sliding on two planes and 114 for sliding on one plane here. When including the intersecting planes that exists outside the main joint sets there are actually considerably more intersections that are critical here then within the main joint sets. Out of the total 68,984 intersections there are actually 5,280 critical intersections for wedge sliding between two planes and 1,121 from one plain (Figure 34). This means that critical planes identified from the kinematic analysis is actually underreported heavily by 4,697 critical intersections for wedge sliding between two planes and 1,007 critical intersections where sliding can happen on one plane.

The other more random plains that does not fit with the main joint sets could just as likely lead to rockfall events, and one cannot pretend they do not exist. This highlights the danger of working with main joint sets for kinematic analysis because it simplifies the data and underreported the actual critical intersections.

Conditions that allow rock fall based on fractures have been identified in the rock wall at site 1. However, it is not easy to say when or how failures can happen in the wall.

Further analysis is needed to more accurately identify slope failure modes and rockfall hazard. Investigating rock samples and doing block theory analysis that identify critical blocks for failure in a rock wall are aspects that could improve the understanding of failure modes at the site (Kulatilake, Wang, Tang, & Liang, 2011). Kulatilake et al. (2011) argue that the results coming from block theory are closer to reality then that of kinematic analysis. Thereby Identifying critical blocks in the wall by block theory might be an appropriate approach of further investigation of the wall.

8.1.2 Rockfall triggers and its relation to climate change

A major reason for rockfall not covered by the kinematic analysis and the preconditions of the rock wall are external forces. These forces are referred to as triggering mechanism and driving conditions, I will discuss two phenomena that releases rockfall namely: Freeze and thaw cycles and extreme precipitation. In addition, climate changes has the ability to have large impact on these triggering mechanisms and can play a major role in areas prone to change in rainfall intensity and change of extreme temperatures.

8.1.2.1 Freeze thaw cycles

By visually inspecting the rock wall at Site one its probable to assume that Freeze and thaw is a probable mechanism that can lead to rockfall. The rock wall has areas where fractures are especially apparent where water can easily enter. The sites do experience temperatures over and below zero degrees Celsius that can be observed from data and backed up by observations in the field. The rock wall at Site 1 is north facing and receives very little sun particularly in the winter year. The closest weather station to Site 1 in Øvstedal has recorded mean temperatures in the winter months the last five years ranging from -0.6 to – 5.6 from month to month. By 2100 temperatures in Norway are expected to rise by an average of 2.5 degrees following warming scenario RCP 4.5, however using RCP 8.5 warming it is expected to rise by 4.5 degrees

on average (Hanssen-Baue, et al., 2017). By using either scenario it is likely that winter months in Bolstadøyri might get positive degree days based on recorded weather data. If these data could be applicable at Site 1, we could assume that we could see a rise in freeze thaw cycles during winter in the future. However, to scrutinize this more thoroughly we would have to look at the range of temperatures at the site rather than mean monthly temperature. Mean temperatures is misleading in the way that we might have positive temperatures in the day while negative temperatures at night leading too freezing and thawing. While mean temperatures only portray one value either positive, negative or zero. Site 2 might experience similar changes but due to the rock wall facing northwest the sun might have a larger impact on this wall that could impact freeze and thaw cycles differently form site 1.

Repeatedly Freeze and thaw cycles are reportedly one of the major triggers of rockfall, In a changing climate is it likely that changing temperatures will have effect on freeze and thaw conditions. But can we assume more rockfalls to happen in a warming climate du to freeze and thaw cycles?

In a study done in limestone the frequency of rockfall was found to be about seven times higher during freeze and thaw. (D'Amato, et al., 2016) indicating a rockfall frequency highly dependent on freeze and thaw cycles.

8.1.2.1 Extreme rainfall

Many studies have reported Extreme participation events as major triggering factors for rockfall (Contino, Bov, Esposito, Giuffré, & Monteleone)

Holset et al 2015

8.1.3 Structure line and block size measurements

8.1.3 Potentially unstable area

The Kinematic analysis indicated that intersections between these two planes do not fall within critical values of wedge sliding. However the apparent fractures in the area is clear signs of deformation. This mean the possibility for this area to fall out is not possible based on these two planes alone. However with the investigation of other factors and more data can shed more light on the probability of this areas stability.
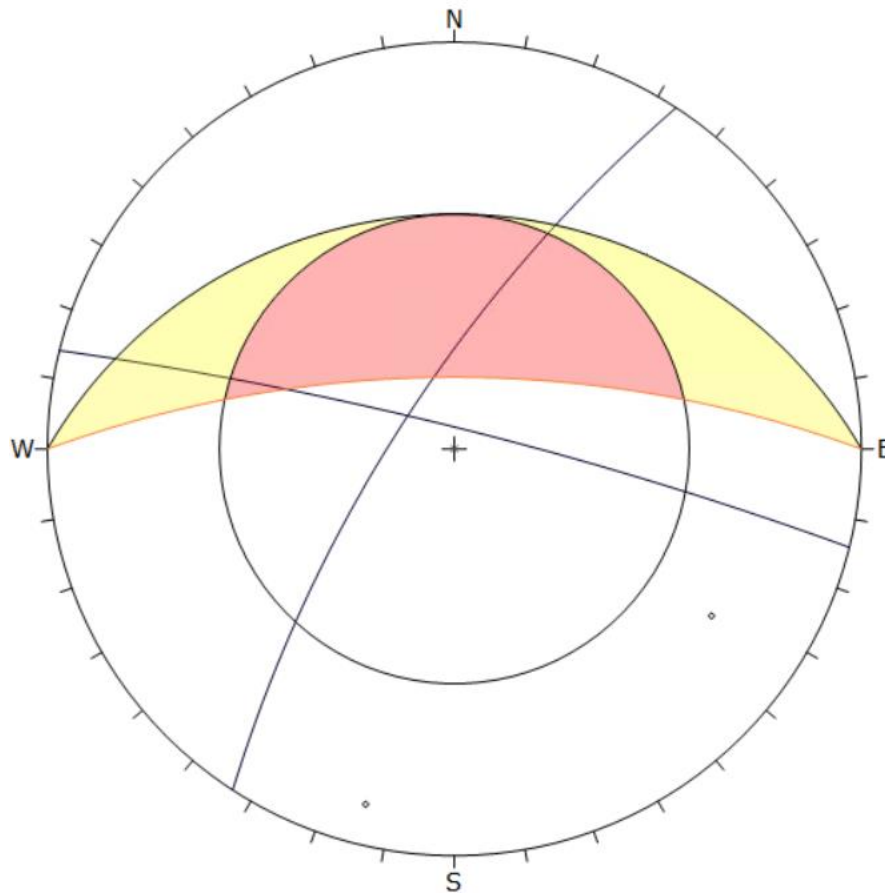
Symbol	Feature
◇	Pole Vectors
■	Critical Intersection

Kinematic Analysis	Wedge Sliding
Slope Dip	70
Slope Dip Direction	0
Friction Angle	30°

	Critical	Total	%
Wedge Sliding	0	1	0.00%

Plot Mode	Pole Vectors
Vector Count	2 (2 Entries)
Intersection Mode	Grid Data Planes
Intersections Count	1
Hemisphere	Lower
Projection	Equal Angle

Figure 38 Intersections of plane A and B defining the possibly unstable area. Critical zone in read area and secondary critical zone in yellow area. The intersection of these two planes alone does not fall within the critical or secondary critical zone.

The Possibly unstable area was nonetheless and interesting area because the fractures in this area were far more open and occurrent then the surrounding areas. The volume calculations done by LiDAR and Photogrammetry has a 14% difference. The Differences in this volume can be explained by uncertainties in each method and that the models do not perfectly align. In The Figure below we can see that distances in the unstable area go up to nearly 28 cm in some areas. However, most of the points fall within 15-0 cm distance from another resulting of half a cubic meter difference between the two models.

I believe that we will see rockfall events at this location in the future. However further investigations are needed in order to investigate possible volumes, timings and modelling to see where rock blocks would end up and If they could potentially reach the road. It must also be considered that the kinematic analysis is only based on surface measurements of the wall and how far the joint sets travel throughout the rock body is uncertain.

9 Conclusion

The work presented in this thesis is presented in two central parts where interpretations and results are presented

    (i)   LiDAR and Photogrammetry 3D modelling of natural rock walls

- By using Photogrammetry and LiDAR eight 3D models were made to extract 3D information from natural rock walls in two locations along E16

- The process of making 3D models by using photogrammetry and LiDAR from Data gathering to finished 3D models ready for interpretation has made grounds for discussing the pros and cos of each approach

- Data gathering for photogrammetry is relatively fast and convenient compared to laser scanning. Where photos can be taken in a matter of minutes with a handheld camera while LiDAR scanning requires at least an hour or two depending on how many scan positions that will be used. LiDAR requires equipment that is quite heavy to carry, and a tripod is needed for the scanner to be stable during scanning. Because both sites were very easily accessible by car there was not much trouble with equipment setup.

- For reliable results GCPs is considered essential for both approaches and entails the installation of GCPs in the rock wall. These were bolted to the wall and was the most time-consuming task during fieldwork as rope were needed in several locations to get access. Results were far superior at Site 1 where GCPs were installed well distributed over the rock wall compared to Site 2 were GCPs ere only installed in a tunnel area underneath the rock wall.

- Comparison of 3D models made from LiDAR in November 2020 and April 2021 at Site 1 show small deviations of zero to two centimeters, supporting LiDAR's reliability in representing the same rock surface in two individual 3D models made with over four moths' gap.

- Photogrammetry 3D models from Site 1 show deviations of up to 20cm.

    (ii)   The secondary focus was the structural geological analysis:

- Four main joint sets were identified from dip and dip direction measurements analyzed in stereo nets in DIPS.

- The major failure mechanism was identified as wedge sliding.

- Toppling and planar sliding was identified as minor but possible failure mechanisms.

- A short coming of the kinematic analysis was that the reported critical values only included planes belonging to main joint sets. Grossly underestimating the critical planes that can fail

- A potential unstable area was identified, and an approximate volume analysis was carried out by using photogrammetry and LiDAR 3D models. The difference of over 3 cubic meters in volume calculation underlines the importance of reliable models. Even though models only have differences ranging from zero to 20 centimeters, it makes considerable errors when calculating volume over a larger volume.

- Block sizes measurements in combination with scan line survey suggested that block sizes are controlled by the joint sets in the wall where distances of same joint sets had distance ranging from 20-60cm.

Bibliography

Abellan, A. D., Derron, M.-H. D., & Jaboyedoff, M. (2016). *"Use of 3D Point Clouds in Geohazards" Special Issue: Current Challenges and Future Trends.* Lausanne: Risk Analysis Group, Institute of Earth Sciences, University of Lausanne.

Abellan, A., Oppikofer, T., Jaboyedof, M., Rosser, N. J., Lim, M., & Lato, M. J. (2013). Terrestrial laser scanning of rock slope instabilities. *Earth Surf. Process. Landforms*, 39, 80–97 (2014). https://onlinelibrary-wiley-com.galanga.hvl.no/doi/pdfdirect/10.1002/esp.3493

Alejano, L. R., Gonza´lez, J., & Muralha, J. (2012). Comparison of Different Techniques of Tilt Testingand Basic Friction Angle Variability Assessment. *Rock Mech Rock Eng*, 45, 1023–1035. DOI 10.1007/s00603-012-0265-7. https://link-springer-com.galanga.hvl.no/content/pdf/10.1007/s00603-012-0265-7.pdf

Angell, E. (2018). Har henta ut minst 20 døde og fleire hundre skadde på «dødsvegen». *NRK*. Hentet fra https://www.nrk.no/vestland/brannsjefen-har-henta-ut-minst-20-dode-og-fleire-hundre-skadde-pa-_dodsvegen_-e16-1.14003356

Behnia, M., & Nateghpour, B. (2020). *Considerations on the Laboratory Estimate of the Basic Friction Angle of Rock Joints.* Geotechnical and geological engineering ed., 38 (3).

Bjordal, H. (2011). *Sikring av vegar mot steinskred.* Statens vegvesen. Hentet fra https://vegvesen.brage.unit.no/vegvesen-xmlui/bitstream/handle/11250/2582754/VD%20rapport%2032.pdf?sequence=1&isAllowed=y

Bolognesi, M., Furin, A., Russo, V., Pellegrinelli, A., & Russo, P. (2014). ACCURACY OF CULTURAL HERITAGE 3D MODELS BY RPAS AND TERRESTRIAL PHOTOGRAMMETRY. *The International Archives of the Photogrammetry, Remote Sensing and Spatial Information Sciences*, Volume XL-5, 2014. https://www.int-arch-photogramm-remote-sens-spatial-inf-sci.net/XL-5/113/2014/isprsarchives-XL-5-113-2014.pdf

Contino, A., Bov, P., Esposito, G., Giuffré, I., & Monteleone, S. (2017). Historical analysis of rainfall-triggered rockfalls: the case study of the disaster of the ancient hydrothermal Sclafani Spa (Madonie Mts, northern-central Sicily, Italy) in 1851. *Nat. Hazards Earth Syst. Sci.,* 17, 2229–2243. https://doi.org/10.5194/nhess-17-2229-2017 https://nhess.copernicus.org/articles/17/2229/2017/nhess-17-2229-2017.pdf

Corominas, J., Copons, R., Moya, J., Vilaplana, J. M., Altimir, J., & Amigo, J. (2005). *Quantitative assessment of the residual risk in a rockfall protected area.* Landslides (2005) 2: 343–357. doi:10.1007/s10346-005-0022-z

D'Amato, J., Hantz, D., Guerin, A., Jaboyedof, M., Baillet, L., & Mariscal, A. (2016). Influence of meteorological factors on rockfall occurrence in a middle mountain limestone cliff. *Nat. Hazards Earth Syst. Sci.*, 16, 719–735. https://nhess.copernicus.org/articles/16/719/2016/nhess-16-719-2016.pdf

Dorren, L. K. (2003). *A review of rockfall mechanics and.* Progress in Physical Geography 27,1 (2003) pp. 69–87. Institute for Biodiversity and Ecosystem Dynamics, Universiteit van Amsterdam.

Eltner, A., & Baumgart, P. (2015). Accuracy constraints of terrestrial Lidar data for soil erosion measurement: Application to a Mediterranean field plot. *Institute of Photogrammetry and Remote Sensing*. https://pdf.sciencedirectassets.com/271791/1-s2.0-S0169555X15X0016X/1-s2.0-S0169555X15300258/main.pdf?X-Amz-Security-Token=IQoJb3JpZ2luX2VjENz%2F%2F%2F%2F%2F%2F%2F%2F%2F%2FwEaCXVzLWVhc3QtMS JGMEQCICIwnradzvSlYnYMy%2BETbwkjvP7YEgx4pU4uzpL2IRT2AiAqfbODPhgAtv

Geological Survey of Norway. (2021, 05 11). *ROCKFALLS AND ROCKSLIDES*. NGU. https://www.ngu.no/en/topic/rockfalls-and-rockslides

Goodman. (2019. july.). *Introduction-to-rock-mechanics* (2.utgave). John Wiley & Sons. https://doku.pub/documents/goodman-r-e-introduction-to-rock-mechanics-2nd-edition-3nl25gdjjml8

Hanssen-Baue, I., Førland, E. J., Haddeland, I., Hisdal, H., Lawrence, D., Mayer, S., . . . Ådlandsvik, B. (2017). Climate in Norway 2100. Miljødirektoratet. file:///C:/Users/Isakh/Downloads/klimarapport-2100-engelsk-web-0160517%20(1).pdf

Hoseth, K. A., Kristensen, L. L., Håland, G., Viklund, M., & Bjordal, H. (2015). *Sikringstiltak mot skred og flom, Befaring i Hordaland og Sogn og Fjordane mai 2014.* Norges vassdrags- og energidirektorat. Hentet fra http://publikasjoner.nve.no/rapport/2015/rapport2015_115.pdf

Ingensand, H. (2006). METROLOGICAL ASPECTS IN TERRESTRIAL LASER-SCANNING TECHNOLOGY. *3rd IAG / 12th FIG Symposium, Baden*. https://www.fig.net/resources/proceedings/2006/baden_2006_comm6/PDF/LS1/Ingensand.pdf

Jaboyedoff, M., Oppikofer, T., Abella´n, A., Derron, M.-H., Loye, A., Metzger, R., & Pedrazzini, A. (2012). Use of LIDAR in landslide investigations: a review. *Nat Hazards* 61, 5–28. DOI 10.1007/s11069-010-9634-2

Karantanellis, E., Arav, R., Dillie, A., Lippl, S., Marsy, G., Torresani, L., & Elberink, S. O. (2020). EVALUATING THE QUALITY OF PHOTOGRAMMETRIC POINT-CLOUDS IN CHALLENGING GEO-ENVIRONMENTS -A CASE STUDY IN AN ALPINE VALLEY. *The International Archives of the Photogrammetry, Remote Sensing and Spatial Information Sciences*, Volume XLIII-B2-2020.

Kemeny, J., & Turner, K. (2008). GROUND-BASED LiDAR Rock Slope Mapping and Assessment. *Publication No. FHWA-CFL/TD-08-006*. Central Federal Lands Highway Division. doi: file:///C:/Users/Isakh/Downloads/dot_49768_DS1.pdf

KERSTEN, T., MECHELKE, K., & MAZIULL, L. (2015). 3D MODEL OF AL ZUBARAH FORTRESS IN QATAR – TERRESTRIAL LASER SCANNING VS. DENSE IMAGE MATCHING. *The International Archives of the Photogrammetry, Remote Sensing and Spatial Information Sciences*, Volume XL-5/W4. DOI:10.5194/isprsarchives-XL-5-W4-1-2015 https://www.researchgate.net/publication/273130686_3D_model_of_al_zubarah_fortress_in_qatar-Terrestrial_laser_scanning_vs_dense_image_matching

Koutsoudis, A., Vidmar, B., Loannakis, G., Arnaoutoglou, F., Pavlidis, G., & Chamzas, C. (2014). Multi-image 3D reconstruction data evaluation. *Journal of Cultural Heritage*, 15 (1), 73-79. https://www-sciencedirect-com.galanga.hvl.no/science/article/pii/S1296207412001926

Krautblatter, M., & Moser, M. (2009). A nonlinear model coupling rockfall and rainfall intensity based on a four year measurement in a high Alpine rock wall (Reintal, German Alps). *Nat. Hazards Earth Syst. Sci.*, 9, 1425–1432. https://nhess.copernicus.org/articles/9/1425/2009/nhess-9-1425-2009.pdf

Kulatilake, P. H., Wang, L., Tang, H., & Liang, Y. (2011). Evaluation of rock slope stability for Yujian River dam site by kinematicand block theory analyses. *Computers and Geotechnics*, 38 (6), 846-860 https://www.researchgate.net/publication/269342270_Rock_Slope_Stability_Study_for_Yujian_River_Dam_Site_Based_on_Kinematic_Analyses

Lato, M. J., Hutchinson, D. J., Gauthier, D., Edwards, T., & Ondercin, M. (2015). Comparison of airborne laser scanning, terrestrial laser scanning, and terrestrial photogrammetry for mapping differential slope change in mountainous terrain. *Canadian Geotechnical Journal*. http://web.b.ebscohost.com.galanga.hvl.no/ehost/pdfviewer/pdfviewer?vid=1&sid=4af210e6-2aa8-46f1-9c43-489dbee7f0db%40pdc-v-sessmgr03

Lichti, D. D., & Jamtsho, S. (2006.06.). Angular resolution of terrestrial laser skanner. *Photogrammetric record*, 2006-06, 21 (114), 141-160. https://bibsys-almaprimo.hosted.exlibrisgroup.com/primo-explore/fulldisplay?docid=TN_cdi_gale_infotracacademiconefile_A158814370&context=PC&vid=HIB&lang=en_US&search_scope=default_scope&adaptor=primo_central_multiple_fe&tab=default_tab&query=any,contains

Lim, M., Petley, D. N., Rosser, N. J., Allison, R. J., Long, A. J., & Pybus, D. (2005). COMBINED DIGITAL PHOTOGRAMMETRY AND TIME-OF-FLIGHT LASER SCANNING FOR MONITORING CLIFF EVOLUTION. *The Photogrammetric Record*, 20 (110), 109–129. https://onlinelibrary-wiley-com.galanga.hvl.no/doi/pdfdirect/10.1111/j.1477-9730.2005.00315.x

Matasci, B., Stock, G. M., Jaboyedoff, M., Carrea, M., Collins, B. D., Guérin, A., . . . Ravanel, L. (2017). Assessing rockfall susceptibility in steep and overhanging slopes using three dimensional analysis of failure mechanisms. *Landslides,* 15 (*5*). doi:http://dx.doi.org/10.1007/s10346-017-0911-y

Matsuoka, N., & Sakaib, H. (1999). Rockfall activity from an alpine cliff during thawing periods. *Geomorphology*, 28, (3–4), 309-328. https://www-sciencedirect-com.galanga.hvl.no/science/article/pii/S0169555X98001160

Meteorologisk institutt. (2021, March 10). *Observations and weather statistics*. Norsk Klimaservicesenter. https://seklima.met.no/observations/

Moon, D., Chung, S., Kwon, S., Seo, J., & Shin, J. (2019). Comparison and utilization of point cloud generated from photogrammetry and laser scanning: 3D world model for smart heavy equipment planning. *Automation in Contruction*, 98 (2019), 322-331.

Nocerino, E., Menna, F., Remondino, F., & Saler, R. (2013). ACCURACY AND BLOCK DEFORMATION ANALYSIS IN AUTOMATIC UAV AND TERRESTRIAL PHOTOGRAMMETRY - LESSON LEARNT -. *ISPRS Annals of the Photogrammetry, Remote Sensing and Spatial Information Sciences*,

Volume II-5/W1, 2013. https://www.isprs-ann-photogramm-remote-sens-spatial-inf-sci.net/II-5-W1/203/2013/isprsannals-II-5-W1-203-2013.pdf

Norsk Klimaservicesenter. (2021, January). *Klimaprofil Hordaland*. Norsk klimaservicesenter. https://klimaservicesenter.no/kss/klimaprofiler/hordaland

O'Connor, J. (2018). *Impact of image quality on SfM Photogrammetry: colour, compression and noise*. [Thesis, Kingston University & Lancaster University]. CORE. https://core.ac.uk/download/pdf/237397224.pdf

Olsen, M. J., & Stuedlein, A. W. (2010). Discussion of "Use of terrestrial laser scanning for the characterization of retrogressive landslides in sensitive clay and rotational landslides in river banks". *Canadian Geotechnical Journal*. Doi:https://doi.org/10.1139/T10-067

Oppikofer, T., Jaboyedoff, M., Blikra, L., Derron, M. H., & Matzger, R. (2009). Characterization and monitoring of the Aknes rockslide using terrrestrial laser scanning. *Nat. Hazards Earth Syst. Sci.*, 9, 1003–1019. https://nhess.copernicus.org/articles/9/1003/2009/nhess-9-1003-2009.pdf

Otterlei, S. S. (2017, 03 18). Hareide: Det er økte kostnader som har gjort E16 Bergen-Voss krevende. *NRK*. https://www.nrk.no/vestland/hareide_-det-er-okte-kostnader-som-har-gjort-e16-bergen-voss-krevende-1.13434074.

Pesci, A., Teza, G., & Bonali, E. (2011). Terrestrial Laser Scanner Resolution: Numerical Simulations and Experiments on Spatial Sampling Optimization. *Remote Sensing*, 3, 167-184. doi:10.3390/rs3010167 https://res.mdpi.com/remotesensing/remotesensing-03-00167/article_deploy/remotesensing-03-00167.pdf

Poisel, R., & Preh, A. (2011). *ROCK FALL DETACHMENT MECHANISMS.* Interdisciplinary Rockfall Workshop 2011 – Innsbruck-Igls. Hentet fra https://publik.tuwien.ac.at/files/PubDat_203976.pdf

Pratt, C., Macciotta, R., & Hendry, M. (2018). Quantitative relationship between weather seasonality and rock fall occurrences north of Hope, BC, Canada. *Bulletin of Engineering Geology and the Environment*, 78, 3239–3251. doi:https://doi.org/10.1007/s10064-018-1358-7

Remondino, F., El-Hakim, S., Gruen, A., & Zhang, L. (2008). Turning images into 3-D models. *IEEE Signal Processing Magazine*, 25 (4), 55 - 65. Doi:10.1109/MSP.2008.923093

RIEGL laser measurements systems. (u.å.) *RIEGL VZ-1000*. Hentet 14. February 2021 from http://www.riegl.com/uploads/tx_pxprieglenloads/DataSheet_VZ-1000_2017-06-14.pdf

Shan, J., & Toth, C. K. (2018). Topographic Laser Ranging and Scanning, Principles and Processing, second edition. *CRC Press*. https://books.google.no/books?hl=no&lr=&id=dGpQDwAAQBAJ&oi=fnd&pg=PP1&dq=Topographic+laser+ranging+and+scanning:+principles+and+processing&ots=lMQYYD5yXW&sig=LUnFZNTTznONIdkgBRKGJ4YT0fY&redir_esc=y#v=onepage&q&f=false

Siem, B. D., & Løvseth, I. C. (2020, 02 7). Dominerer skrekkliste: Seks av dei ti mest rasfarlege vegane ligg i Vestland. *NRK*. https://www.nrk.no/vestland/vegvesenet-med-rangering-av-rasfare_-seks-av-dei-ti-mest-rasfarlege-vegane-ligg-i-vestland-1.14872698.

Skarlatos, D., & Kiparissi, S. (2012). COMPARISON OF LASER SCANNING, PHOTOGRAMMETRY AND SFM-MVS PIPELINE APPLIED IN STRUCTURES AND ARTIFICIAL SURFACES. *ISPRS Annals of the*

Photogrammetry, Remote Sensing and Spatial Information Sciences, I-3, 2012.
https://www.isprs-ann-photogramm-remote-sens-spatial-inf-sci.net/I-3/299/2012/isprsannals-I-3-299-2012.pdf

Slob, S., & Hack, R. (2004). 3D Terrestrial Laser Scanning as a New Field Measurement and Monitoring Technique. https://www.researchgate.net/profile/Henri-Hack/publication/225707974_3D_Terrestrial_Laser_Scanning_as_a_New_Field_Measurement_and_Monitoring_Technique/links/0c96051fd04f48aa39000000/3D-Terrestrial-Laser-Scanning-as-a-New-Field-Measurement-and-Monitoring-

Smith, J. V., & Arnhardt, C. (2016). Distinguishing between single and double plane sliding of tetrahedral. *Engineering Geology*, 211 (7). Doi:DOI:10.1016/j.enggeo.2016.07.003

Volkwein, A., Schellenberg, K., Labiouse, V., Agliardi, F., Berger, F., Bourrier, F. & Jaboyedoff, M. (2011). Rockfall characterisation and structural protection – a review. WSL Swiss Federal Institute for Forest, Snow and Landscape Research, Zurcherstrasse 111, 8903 Birmensdorf, Switzerland.

Yogender, Raghavendra, S., & Kushwaha, S. K. (2020). Role of Ground Control Points (GCPs) in Integration of Terrestrial Laser Scanner (TLS) and Close-range Photogrammetry (CRP). Applications of Geomatics in Civil Engineering. Page: 531-537. doi:https://doi-org.galanga.hvl.no/10.1007/978-981-13-7067-0_42

Zhang, J., & Lin, X. (2017). *Advances in fusion of optical imagery and LiDAR point cloud applied to photogrammetry and remote sensing.* International Journal of Image and Data Fusion, 8:1, 1-31. doi:https://doi.org/10.1080/19479832.2016.1160960

Appendix

Statistics from stereonet 1 (Field data)

Joint set	Number of individual planes	Entries included	1 S.D. (68.26%)	2 S.D. (95.44%)	3 S.D (99.74%)	50%
1F	24	Variability Limit	8.87986°	14.5908°	20.3093°	6.89847°
		Confidence Limit	1.81999°	2.98561°	4.14564°	1.41443°
1J1	19	Variability Limit	7.07838°	11.6235°	16.1639°	5.49975°
		Confidence Limit	1.62804°	2.6707°	3.70829°	1.26526°
1J2	23	Variability Limit	9.66693°	15.8891°	22.127°	7.50936°
		Confidence Limit	2.02543°	3.32269°	4.6138°	1.57408°
1J3	32	Variability Limit	16.5787°	27.3592°	38.3366°	12.8667°
		Confidence Limit	2.97349°	4.87846°	6.77512°	2.31082°
1J4	**7**	Variability Limit	16.5787°	27.3592°	38.3366°	12.8667°

		Confidence Limit	2.97349°	4.87846°	6.77512°	2.31082°

Statistics from stereonet 2 (Digital data)

Joint set	Number of individual planes	Confidence level	1 S.D. (68.26%)	2 S.D. (95.44%)	3 S.D (99.74%)	50%
2F	**51**	Variability Limit	13.6659°	22.508°	31.4425°	10.6108°
		Confidence Limit	1.93268°	3.1705°	4.40242°	1.502°
2J1	**59**	Variability Limit	10.948°	18.0051°	25.0955°	8.50335°
		Confidence Limit	1.4344°	2.35301°	3.26711°	1.11477°
2J2	6	Variability Limit	9.29512°	15.2757°	21.2677°	7.2208°
		Confidence Limit	3.80946°	6.25076°	8.68252°	2.9604°
2J3	5	Variability Limit	5.55999°	9.12635°	12.6835°	4.32042°
		Confidence Limit	2.48981°	4.08468°	5.67226°	1.93496°
2J4	4	Variability Limit	4.81553°	7.90306°	10.9806°	3.74208°
		Confidence Limit	2.41002°	3.95374°	5.49036°	1.87295°

Statistics from stereonet 3 (Combined data)

Joint set	Number of individual planes	Confidence level	1 S.D. (68.26%)	2 S.D. (95.44%)	3 S.D (99.74%)	50%
3F	69	Variability Limit	10.2451°	16.8436°	23.4651°	7.958°
		Confidence Limit	1.24026°	2.03452°	2.82485°	0.963893°
3J1	37	Variability Limit	8.07316°	13.2614°	18.4505°	6.2722°
		Confidence Limit	1.33176°	2.18462°	3.03328°	1.035°
3J2	79	Variability Limit	10.0974°	16.5997°	23.123°	7.84339°
		Confidence Limit	1.14223°	1.87369°	2.60153°	0.887705°
3J3	49	Variability Limit	8.97322°	14.7448°	20.5246°	6.97094°
		Confidence Limit	1.28735°	2.11176°	2.93211°	1.00049°